

Nanoscale investigation of high temperature oxidation mechanisms of high-Cr ferritic steels

Ashok Vayyala

Energie & Umwelt / Energy & Environment

Band / Volume 491

ISBN 978-3-95806-467-6

Forschungszentrum Jülich GmbH
Zentralinstitut für Engineering, Elektronik und Analytik (ZEA)
Analytik (ZEA-3)

Nanoscale investigation of high temperature oxidation mechanisms of high-Cr ferritic steels

Ashok Vayyala

Schriften des Forschungszentrums Jülich
Reihe Energie & Umwelt / Energy & Environment

Band / Volume 491

ISSN 1866-1793

ISBN 978-3-95806-467-6

Bibliografische Information der Deutschen Nationalbibliothek.
Die Deutsche Nationalbibliothek verzeichnet diese Publikation in der
Deutschen Nationalbibliografie; detaillierte Bibliografische Daten
sind im Internet über <http://dnb.d-nb.de> abrufbar.

Herausgeber und Vertrieb: Forschungszentrum Jülich GmbH
Zentralbibliothek, Verlag
52425 Jülich
Tel.: +49 2461 61-5368
Fax: +49 2461 61-6103
zb-publikation@fz-juelich.de
www.fz-juelich.de/zb

Umschlaggestaltung: Grafische Medien, Forschungszentrum Jülich GmbH

Druck: Grafische Medien, Forschungszentrum Jülich GmbH

Copyright: Forschungszentrum Jülich 2020

Schriften des Forschungszentrums Jülich
Reihe Energie & Umwelt / Energy & Environment, Band / Volume 491

D 82 (Diss. RWTH Aachen University, 2020)

ISSN 1866-1793
ISBN 978-3-95806-467-6

Vollständig frei verfügbar über das Publikationsportal des Forschungszentrums Jülich (JuSER)
unter www.fz-juelich.de/zb/openaccess.



This is an Open Access publication distributed under the terms of the [Creative Commons Attribution License 4.0](https://creativecommons.org/licenses/by/4.0/), which permits unrestricted use, distribution, and reproduction in any medium, provided the original work is properly cited.

Abstract

Fe–22Cr–0.5Mn based ferritic steels are being used as construction materials for interconnects in solid oxide cells (SOCs). Oxidation resistance of these steels is critical for their performance and was investigated in the present work under conditions relevant for the interconnect operation. A set of ferritic steels of a Crofer family, including the commercial steel Crofer 22 H, were oxidized at 800 °C in Ar–O₂, Ar–H₂–H₂O and Ar–CO–CO₂ model gases simulating air and fuel sides of the fuel cells. The key factors controlling the high temperature oxidation behavior are addressed in the work, namely i) the effect of gas composition and ii) the role of alloying elements in the steels, especially minor additives.

A set of analytical techniques was employed to characterize the oxidation process as well as the related structural changes in the steels. TG data were correlated with the results of the elemental analysis from GD–OES, phase analysis by XRD or Raman spectroscopy and microstructural analysis using SEM. A special focus in the work was put on high–resolution characterization methods such as TEM and APT, which enable to reveal the microstructure of the oxide scale and the elemental distribution at the nanoscale level and thereby investigate the mass transport processes through the oxide. APT was extensively used for obtaining atomic scale insight into the microstructure, particularly at grain boundaries, and the obtained information was employed to shed light on the oxidation mechanisms.

The oxidation rate of these ferritic steels strongly depends on the oxygen partial pressure as well as on the alloy chemistry, even on small compositional changes. All studied alloys form a duplex oxide scale consisting of MnCr₂O₄ spinel on top of Cr₂O₃ in all atmospheres. Addition of Nb resulted in Nb–rich rutile–type oxide layer formation at the chromia–alloy interface. Subsequent addition of Si to Nb–containing alloy leads to disappearance of Nb–rich oxide layer and formation of a mesh–like SiO₂ layer at this interface. Ti addition promotes formation of the internal oxidation zone.

APT revealed and quantified segregation of minor alloying constituents (Nb, Ti, Mn and Si) at the oxide GBs, which control the mass transport through the oxide scale, and at the alloy–oxide interfaces. Relationships between segregation activity of individual elements (in terms of Gibbsian interfacial excess), oxide scale microstructure and alloy oxidation rate have been established based on APT results. In particular, it was shown that the elemental segregation activity and the oxide grain structure do not correlate with the oxidation rate differences in different atmospheres, whereas the porosity of the oxide scale was assumed to be the key parameter controlling the oxidation rate. Comparison of GB segregation activities in different studied alloys revealed that vacancies formation due to Wagner–Hauffe doping with aliovalent impurities (Ti and Nb), which is commonly assumed as a mechanism for the impurity

effect, cannot be solely responsible for faster oxidation, and the structural alteration of grain boundaries in presence of segregating species was proposed as an alternative mechanism. The role of Si and the reactive element (La) was also investigated and explained based on the direct nanoscale information. The obtained results can be used for future development of high-Cr steels with an improved oxidation resistance.

Kurzzusammenfassung

Fe – 22 Cr – 0.5 Mn basierete Stähle werden beim Aufbau von Solid Oxide Fuel Cells (SOFCs) als Interconnect–Materialien eingesetzt. Als kritischer Parameter für seine Funktion als Interconnect–Material wurde in der vorliegenden Arbeit die Oxidationsbeständigkeit dieser Stähle untersucht. Dazu wurden verschiedene Crofer–Stähle, einschließlich des kommerziell verfügbaren Crofer 22 H, bei 800 °C in Ar – 20 %O₂, Ar – 4 %H₂ – 4 %H₂O und Ar – 1 %CO – 1 %CO₂ als Modell–Gasgemischen für die Luft– und Brenngas–Gemische einer Brennstoffzelle oxidiert. Als Schlüsselfaktoren für das Oxidationsverhalten wurden in dieser Arbeit die Zusammensetzung der Gasgemische und die Rolle der Legierungsbestandteile insbesondere der Nebenbestandteile untersucht.

Der Oxidationsprozess und die damit einhergehenden Strukturänderungen wurden mit verschiedenen analytischen Verfahren charakterisiert. TG Daten wurden mit den Ergebnissen der GD–OES, der Phasenanalyse mittels XRD oder Raman Spektroskopie sowie der Mikrostruktur–analyse mittels SEM korreliert. Der Kernfokus der Arbeit lag jedoch auf Einsatz der hochauflösenden Analysetechniken TEM und APT, die Veränderungen in der Mikrostruktur in Bezug auf Oxidation und Elementverteilung/–umverteilung im nm–Bereich ermöglichen und damit ermöglichen Transportprozesse durch Oxide zu untersuchen. APT wurde extensiv für die Untersuchung der Mikrostruktur in atomarer Auflösung, insbesondere an Korngrenzen eingesetzt, wodurch Informationen über den Oxidationsmechanismus erhalten wurden.

Die Oxidationsraten der Stähle hängen stark vom Partialdruck des Sauerstoffs und der Legierungschemie ab, auch wenn die Zusammensetzung sich nur geringfügig ändert. Alle Legierungen bilden Doppeloxide aus MnCr₂O₄ Spinell auf der Cr₂O₃ Schicht, unabhängig von der Atmosphäre. Die Zugabe von Nb führte zu einer Nb–angereicherten Oxid–Schicht vom Rutil–Typ auf dem Cr–Oxid Interface. Die Schrittweise Zugabe von Si zu den Nb–haltigen Legierungen zeigte die Abnahme der Nb–angereicherten Oxidschichten und das Entstehen einer netzartigen SiO₂ Schicht am Interface. Ti–Zugabe förderte die Bildung einer internen Oxidationszone.

Mittels APT konnte die Segregation von Legierungs–Nebenbestandteilen (Nb, Ti, Mn and Si) an den Korngrenzen und den Metal–Oxid–Interfaces, die den Massentransport durch die Oxidschicht bestimmen, quantitativ bestimmt werden. Die Beziehung zwischen der Segregationsaktivität einzelner Elemente (Gibbsian interfacial excess), Oxidschicht–Mikrostruktur und Oxidationsraten ist auf Basis der APT Ergebnisse etabliert worden. Spezifisch wurde gezeigt, dass die Segregationsaktivität und die Oxid–Korn–Struktur nicht mit den unterschiedlichen Oxidationsraten in verschiedenen Atmosphären korrelieren, wohin gehen die Porosität der Oxidschicht als Schlüsselparameter für die Oxid–Wachstumsrate angenommen wird. Der Vergleich der Segregationsaktivitäten an Korngrenzen in verschiedenen Legierungen zeigt, dass die Leerstellenbildung gemäß Wagner–Hauffe Doping mit aliovalenten Verunreinigungen (Ti

und Nb), die typischer Weise als der Mechanismus für die Verunreinigungeneffekt angesehen wird, nicht als alleiniger Grund für die schnellere Oxidation auftreten kann. Daher werden die Strukturänderungen der Korngrenzen bei gleichzeitiger Segregation als alternativer Mechanismus vorgeschlagen. Die Rolle des Si und des reaktiven Elementes La ist ebenfalls untersucht worden und kann auf Basis der Nanoinformationen erklärt werden. Die erhaltenen Ergebnisse dienen der Weiterentwicklung von hochlegierten Cr-Stählen mit verbesserter Oxidationsstabilität.

Contents

Abstract	v
Kurzzusammenfassung	vii
List of Abbreviations	xix
1 Introduction	1
1.1 Solid Oxide Cell (SOC) and its components	2
1.2 Materials for SOC	3
1.2.1 Anode	3
1.2.2 Cathode	3
1.2.3 Electrolyte	4
1.2.4 Interconnects	4
2 Scientific Background	7
2.1 An overview of metal oxidation theory	7
2.2 Thermodynamics of high temperature oxidation	9
2.3 Kinetics of high-temperature oxidation	12
2.4 Development of high-Cr ferritic steels for SOC interconnects	14
2.5 Reactive element (RE) effect in high-Cr ferritic steels	16
2.6 Effect of gas composition on interconnect oxidation	18
2.7 Internal oxidation	20
2.8 Diffusion and mass transport in thermally grown oxide	20
2.9 Nanoscale characterization of thermal oxide scales	21
2.9.1 Transmission electron microscopy	21
A Energy dispersive X-ray spectroscopy (EDX/EDS)	23
B Application to thermally grown oxide scales	24

2.9.2	Atom Probe Tomography (APT)	25
	A Historical perspective	25
	B Fundamentals	26
	C Sample preparation	27
	D Application of APT to thermally grown oxide scales	28
2.10	Motivation	29
3	Experimental Methods	31
3.1	Alloys investigated	31
3.2	Oxidation Testing	32
3.3	Materials Characterization	32
3.3.1	Phase Analysis	32
	A X-ray Diffraction (XRD)	32
	B Raman Spectroscopy	33
3.3.2	Compositional Depth Profiling	33
3.3.3	Electron Microscopy	33
	A Scanning Electron Microscopy (SEM)	33
	B Transmission Electron Microscopy (TEM)	33
3.3.4	Atom Probe Tomography (APT)	34
4	Effect of gas composition on high temperature oxidation	36
4.1	Introduction	36
4.2	Thermogravimetric analysis	37
4.3	Phase analysis	38
4.4	Elemental Depth profiling	40
4.5	Electron microscopy	43
	4.5.1 Scanning Electron Microscopy (SEM)	43
	4.5.2 Transmission Electron Microscopy (TEM)	45
4.6	Atom probe tomography	48
	4.6.1 Chromia scale in Ar–O ₂	48
	4.6.2 Chromia scale in Ar–4% H ₂ –4% H ₂ O	51
	4.6.3 Chromia scale in Ar–1% CO–1% CO ₂	53
4.7	Oxidation Mechanisms	54
	4.7.1 Nanoscale considerations for the oxide scale growth	54
	4.7.2 Carbon transport through Cr ₂ O ₃	56

4.7.3 Chromia plate/whisker formation	57
4.8 Summary	57
5 Role of minor alloying elements on high temperature oxidation	59
5.1 Oxidation Kinetics	59
5.2 Glow discharge optical emission spectroscopy	61
5.3 Electron Microscopy analysis	62
5.3.1 Scanning electron microscopy (SEM)	62
5.3.2 Scanning transmission electron microscopy (STEM)	64
5.4 Atom probe tomography (APT)	65
5.4.1 Alloy-NTS	65
A Chromia scale	65
B Metal-oxide interface	67
5.4.2 Alloy-NT	68
A Chromia scale	68
B Metal-oxide interface	70
5.4.3 Alloy-T	71
A Chromia scale	71
B Metal-oxide interface	72
5.4.4 Alloy-N	73
A Chromia scale	73
B Metal-oxide interface	75
5.5 Discussion	75
5.5.1 General considerations of GB influence on the oxidation behavior	75
5.5.2 Quantification of GB segregation from APT data	76
5.5.3 Elemental diffusion through the chromia scale	77
5.5.4 Intermittent oxide phases between chromia and alloy	78
5.5.5 Reactive element effect	79
5.6 Summary	80
6 Internal oxidation	82
6.1 Scanning electron Microscopy (SEM)	82
6.2 Transmission electron Microscopy (TEM)	83
6.3 Atom probe tomography (APT)	84
6.4 Thermodynamic considerations	88

Contents

6.5	Influence of gas composition	89
6.6	Summary	89
7	Conclusion	91
7.1	Possible pathways for further steel development	93
	Bibliography	94
	Acknowledgements	103
	Curriculum Vitae	104

List of Figures

1.1	Schematic representation of energy storage by various devices as a function of time [5]	2
1.2	Schematic of an SOFC stack showing different components and relevant gas atmospheres (air and fuel).	5
2.1	Schematic showing various stages of metal–oxygen reactions during high temperature exposure [20].	8
2.2	Ellingham diagram for several metal oxides based on their Gibbs free energy as a function of temperature [21]	11
2.3	Wagner’s model of high–temperature oxidation [21].	12
2.4	Schematic of detrimental effect of RE during high–temperature oxidation. RE ions diffuse outwards from the underlying alloy via oxide scale grain boundaries and become enriched at the gas–scale interface (surface) [49].	17
2.5	Weight gain plot of Fe–24Cr alloys containing reactive element additions such as Ce, Y, Zr and La during oxidation at 800 °C in air (Ar–O ₂) [29]	18
2.6	Schematic representation of various signals generated during the interaction of specimen with the incident electron beam.	22
2.7	Schematic representation of various imaging modes in TEM. a) Bright–Field TEM, b) Dark–Field TEM, c) Bright–Field STEM and d) Dark–Field STEM. [74].	22
2.8	An example of EDS area analysis of the thermally grown chromia scale on ferritic steel.	24
2.9	TEM micrographs of thermally grown Cr ₂ O ₃ scales on Ni–25Cr at 1050 °C for 4 hours in (a) Ar–20%O ₂ and (b) Ar–4%H ₂ –2%H ₂ O atmospheres [54]. . . .	25
2.10	Schematics of specimen, local electrode and position sensitive detector in the analysis chamber of an APT instrument.	27
2.11	Site specific sample preparation for APT measurement using FIB [89].	28

2.12	Correlative APT-TEM approach for a thermally grown alumina scale (a) bright-field STEM image of an APT specimen and corresponding EDS mapping for Ti, Y and Ga including APT atom maps and (b) elemental concentration profiles from the grain boundary [94].	29
4.1	Thermogravimetric test results acquired during isothermal oxidation of Alloy-NT at 800 °C in different gas compositions for 72 hours of exposure: (a) mass change as a function of the exposure time and (b) instantaneous <i>apparent</i> parabolic rate constant (k_w) as a function of the exposure time.	37
4.2	Room temperature XRD patterns acquired after isothermal oxidation of Alloy-NT exposed to different gas compositions at 800 °C for 72 hours.	39
4.3	Raman spectra acquired after isothermal oxidation of Alloy-NT in different gas compositions at 800 °C for 72 hours.	40
4.4	GD-OES depth profiling of various elements for the Alloy-NT exposed in Ar-20%O ₂ at 800 °C for 72 hours of exposure.	41
4.5	GD-OES depth profiling of various elements for the Alloy-NT exposed in Ar-4%H ₂ -4%H ₂ O at 800 °C for 72 hours.	42
4.6	GD-OES depth profiling of various elements for the Alloy-NT exposed in Ar-1%CO-1%CO ₂ at 800 °C for 72 hours.	42
4.7	Surface morphologies of the Alloy-NT exposed at 800 °C for 72 hours in (a, d) Ar-20%O ₂ , (b, e) Ar-4%H ₂ -4%H ₂ O and (c, f) Ar-1%CO-1%CO ₂ . The figure also shows globular type oxide in case of Ar-20%O ₂ (high p_{O_2}) and plate-like morphology in case of Ar-4%H ₂ -4%H ₂ O and Ar-1%CO-1%CO ₂ (low p_{O_2} gases).	44
4.8	Cross sectional SEM images of the Alloy-NT exposed at 800 °C for 72 hours. (a, d) Ar-20%O ₂ , (b, e) Ar-4%H ₂ -4%H ₂ O and (c, f) Ar-1%CO-1%CO ₂	45
4.9	Bright-field STEM images of oxide layers formed on the surface of Alloy-NT at 800 °C after 72 hours of exposure in (a) Ar-20%O ₂ , (b) Ar-4%H ₂ -4%H ₂ O and (c) Ar-1%CO-1%CO ₂	46
4.10	Bright-field STEM micrographs shown for chromia grain size comparison formed on Alloy-NT at 800 °C oxidized in three different gas compositions for 72 hours.	48

4.11	APT analysis of chromia scale formed on the Alloy–NT exposed to Ar – 20%O ₂ at 800 °C for 72 hours. (a) Atom maps of chromia showing the elemental segregation to grain boundaries (Ti, Nb and Mn) and solubility in grains (Ti, Mn and Fe are not uniformly distributed), (b) and (c) are the elemental concentration profiles for major and minor elements, respectively, across a random grain boundary marked with an arrow in (a).	49
4.12	(a) Atom maps from APT for a grain interior decorated with Nb and Mn iso-surfaces. (b) Typical concentration profiles across a grain interior. (c) Proxigrams for the Mn-rich nano precipitates showing the substoichiometry of the inner spinel nuclei.	51
4.13	Atom maps from APT for the chromia formed on Alloy–NT after isothermal oxidation at 800 °C in Ar – H ₂ – H ₂ O for 72 h.	52
4.14	(a) Concentration profiles across a random grain boundary from Figure 4.13, and (b) Proxigrams across the interfaces encompassing Si-rich regions in the chromia scale.	53
4.15	Atom maps from APT of chromia scale formed on Alloy–NT after isothermal oxidation at 800 °C in Ar – CO – CO ₂ for 72 hours.	54
4.16	Schematic illustrating that the oxide scale composition and microstructure of Alloy–NT. Nb ⁴⁺ segregation to the chromia scale GBs increases local concentration of Cr vacancies (V'''_{Cr}) leading to enhanced transport of Cr and Mn, and consequently higher weight gain in low pO_2 gases.	55
5.1	Thermogravimetric test results acquired during isothermal oxidation of four different alloys at 800 °C in Ar – 4%H ₂ – 4%H ₂ O: (a) mass change as a function of the exposure time and (b) instantaneous <i>apparent</i> parabolic rate constant $k_p(t)$ as a function of the exposure time.	60
5.2	Glow Discharge–Optical Emission Spectroscopy (GD–OES) depth profiling of different alloys oxidized at 800 °C for 72 hours in Ar – 4%H ₂ – 4%H ₂ O. (a) Alloy–NTS (Crofer 22 H), (b) Alloy–NT (KCL), (c) Alloy–T (Crofer 22 APU) and (d) Alloy–N (KCD).	61
5.3	Surface morphologies (left column) and cross sectional (right column) SEM micrographs of the alloys exposed for 72 h at 800 °C in Ar – 4%H ₂ – 4%H ₂ O: (a) and (e) Alloy–NTS, (b) and (f) Alloy–NT, (c) and (g) Alloy–T, (d) and (h) Alloy–N.	63
5.4	Bright–field TEM images of (a) Alloy–N and (b) base Alloy–NTS oxidized for 72 h at 800 °C in Ar – 4%H ₂ – 4%H ₂ O and (c) corresponding EDS elemental maps for Alloy–NTS.	64

5.5 APT analysis of the Cr₂O₃ scale thermally grown on Alloy-NTS (base alloy) during oxidation at 800 °C in Ar-4%H₂-4%H₂O: (a) atom maps of Ti, Mn, Si and Nb; (b) elemental concentration profiles across GBs in the chromia scale; (c) proximity histograms across an interface between chromia and inner spinel grains. The inset shows a magnified view at the same interface to highlight minor impurities. 66

5.6 APT analysis of the oxide-alloy interface region in Alloy-NTS (base alloy) after oxidation at 800 °C in Ar-4%H₂-4%H₂O: (a) combined atom maps for the chromia-alloy interfacial region; (b) 15 at. % Si iso-concentration surface delineating the net-like SiO₂ layer forming at the metal-oxide scale interface; (c) proximity histograms across the interface for major and minor alloying elements. 68

5.7 APT atom maps for the inner chromia scale formed on Alloy-NT after isothermal oxidation at 800 °C in Ar-4%H₂-4%H₂O for 72 hours. 69

5.8 APT analysis of a GB region in chromia scale formed on Alloy-NT oxidized isothermally at 800 °C in Ar-4%H₂-4%H₂O for 72 h. (a) Atom maps of impurities present in the GB region showing dissimilar segregation behavior. (b) Elemental concentration profiles across the GBs. 70

5.9 APT analysis of the oxide/alloy interface region in Alloy-NT after isothermal oxidation at 800 °C in Ar-4%H₂-4%H₂O for 72 hours. (a) A combined atom map for major elements from the regions near the interface between oxide and alloy. (b) Magnified interfacial region from (a) with atom maps for Nb, Ti and Si. (c) Concentration profile of Mn across the GB in the oxide scale. (d), (e) Proximity histograms across the oxide/alloy interface for major alloying elements and Si, respectively. 71

5.10 APT analysis of the chromia scale on Alloy-T (without Nb and Si) oxidized isothermally at 800 °C in Ar-4%H₂-4%H₂O for 72 hours. (a) Atom maps of alloying elements present in Cr₂O₃ and (b) concentration profiles across a grain boundary for primary segregants (Ti and Mn). 72

5.11 APT analysis of the chromia-alloy interface region in Alloy-T (without Nb and Si) after 72 h oxidation at 800 °C in Ar-4%H₂-4%H₂O: (a) a combined atom map and (b) proximity histograms across the chromia-alloy interface. A magnified inset highlights Ti segregation at the interface. 73

5.12	APT analysis of chromia scale on Alloy-N (without Ti and Si) oxidized isothermally at 800 °C in Ar-4% H_2 -4% H_2O for 72 h. (a) Atom maps of alloying elements present in Cr_2O_3 (Nb and Mn) and (b) concentration profile of grain boundary segregants (Nb and Mn) for the Cr_2O_3 phase.	74
5.13	APT analysis of the oxide-alloy interfacial region in Alloy-N (without Ti and Si) after 72 h oxidation at 800 °C in Ar-4% H_2 -4% H_2O : (a) atom maps demonstrating formation of a (Nb,Cr) O_2 layer next to the alloy; (b) proximity histograms across the metal-oxide interface showing weak Si segregation.	74
6.1	SEM micrographs of the cross sectional samples from different alloys oxidized at 800 °C for 72 hours in Ar-4% H_2 -4% H_2O . (a) Alloy-NTS (Crofer 22 H), (b) Alloy-NT (KCL), (c) Alloy-T (Crofer 22 APU) and (d) Alloy-N (KCD). All images are shown at same magnification. The alloys' names given in the parenthesis refer to their designations in commercial use or in the lab as well as in our earlier publications.	83
6.2	Bright-field TEM images of Alloy-NT oxidized at 800 °C for 72 hours in Ar-4% H_2 -4% H_2O . (a) Low magnification and (b) corresponding high magnification image showing metal-oxide interface and the internal oxidation zone.	84
6.3	APT analysis of an inner Ti-rich oxide particle (Region 1 in Figure 6.2b) in Alloy-NT after isothermal oxidation at 800 °C in Ar-4% H_2 -4% H_2O for 72 hours. (a) Alloy/oxide particle interface with atom maps of major (Fe, Cr, Nb, Ti) and minor (Si, Mn, Al, B and C) alloying elements. (b) Mass spectrum showing the presence of impurities, such as B and C at the alloy/oxide particle interface. (c) Proximity histogram built across the alloy/oxide particle interface for major alloying elements and (d) for minor alloying elements.	85
6.4	Concentration profiles from APT measurement for (a) alloy grain boundary and (b) oxide particle grain boundary.	86
6.5	APT atom maps of subsurface layer containing small oxide precipitates (Region 2 in Figure 6.2b). Proxigram for the matrix and inner oxide precipitates interface for (a) primary elements and (b) minor elements.	87
6.6	A small sub-volume of the Nb-rich nanoclusters as shown in Figure 6.5(a) and (b) Atom maps of oxygen and niobium respectively and (c) proximity histogram profiles for Fe, Cr, Nb and O. The inset figure highlights the Nb-rich oxide most likely of NbO_2 stoichiometry (as oxygen deficiency is an inherent artifact of APT).	88

*

List of Tables

3.1 Chemical composition of the investigated alloys as determined by ICP–OES (in at. %). Alloys designations contain N for Niobium, T for Titanium and S for Silicon additions.	31
4.1 The partial pressures of oxygen calculated using FACTSAGE for different gas compositions used in the current research work.	36
4.2 Thickness (in μm) of different oxide scales formed after 72 hours of oxidation at 800 °C in different gas compositions for the Alloy–NT.	47
4.3 APT bulk composition of chromia scales formed in different gas atmospheres relevant to SOFC/SOEC.	50
5.1 Thickness (in μm) of the various subscales in the surface oxide formed on the studied alloys.	62
5.2 APT bulk composition of chromia scales formed in different gas atmospheres relevant to SOFC/SOEC.	66
5.3 Gibbsian interfacial excess values G_i for grain boundary segregation in the chromia scale.	76

*

List of Abbreviations

2D	Two-dimensions
3D	Three-dimensions
APT	Atom Probe Tomography
EDS	Energy Dispersive Spectroscopy
EELS	Electron Energy Loss Spectroscopy
FIB	Focused Ion Beam
FIM	Field Ion Microscopy
FZJ	Forschungszentrum Jülich
GB	Grain Boundary
GD-OES	Glow Discharge-Optical Emission Spectroscopy
HAADF	High Angle Annular Dark Field
ICP-OES	Inductively Coupled Plasma Optical Emission Spectroscopy
ICP-MS	Inductively Coupled Plasma Mass spectroscopy
MS	Mass Spectrum/Mass spectroscopy
SEM	Scanning Electron Microscopy
SOEC	Solid Oxide Electrolyzer Cell
SOFC	Solid Oxide Fuel Cell
STEM	Scanning Transmission Electron Microscopy
TEM	Transmission Electron Microscopy
TJ	Triple Junction
TG	Thermogravimetric
XRD	X-ray Diffraction
ZEA-3	Zentralinstitut für Engineering, Electrical und Analytik

1 Introduction

The sources of renewable energy and their share in electricity generation have increased continuously, largely driven by politics, industries and environmental issues [1]. In the renewable energy market, wind and solar power have a majority share as they are abundant and do not emit greenhouse gases. For example, just in the European Union, these renewable energies would account for about 20% of the gross final energy consumption by 2020 and 60% by 2050 [2]. However, local meteorological conditions make these renewable sources highly sporadic, i.e. they are highly fluctuating on many different time scales [3, 4]. Controlling and suppressing these energy fluctuations is the key for the adaptability of technologies such as wind turbines, photovoltaic and solar thermal power systems in the electric grid system. Therefore, one of the most significant challenges for continuous energy production in the future relies on stable renewable energies. Power-to-X (P2X) is one such renewable energy conversion and storage concepts by which the fluctuations in renewable energy can be suppressed. In the P2X concept (X can be chemicals, fuel, hydrogen, food, methane, mobility etc.) surplus electricity from renewable sources such as wind and/or solar is utilized by converting it into more usable form. Among others, this can be done in conjunction with industrial wastes such as CO₂ by a process called co-electrolysis, using an electrochemical device – solid oxide electrolyzer cell (SOEC). Compared to the currently existing conventional energy storage devices like capacitors and batteries, power-to-gas (P2G) has the highest energy storage capacity with respect to the storage duration as can be seen in [Figure 1.1](#).

Our interest in SOEC is not only due to their significantly higher power density, but also because they do not require expensive noble metals, have low exhaust emissions as they can convert greenhouse gases like CO₂ into CO at high operating temperature of 700–900 °C. The high operating temperatures of SOECs are also very advantageous from water management point of view, in comparison with the proton-exchange membrane fuel cell (PEM/PEMFC), as in SOECs the water produced is in vapor phase and thus the conductivity and resistance in the

cell remain unaffected by the presence of water. Alternatively, the water vapor can be used for co-generation or combined cycle operations. All these factors combined with the fact that there are no mechanical rotating or moving parts, makes SOECs very attractive in comparison to the other fuel cells. However, the high operating temperatures of SOECs are accompanied by their own set of problems, mainly, accelerated degradation of the cell components. Hence there is a significant room for improvement in the performance of these devices to make them more competitive.

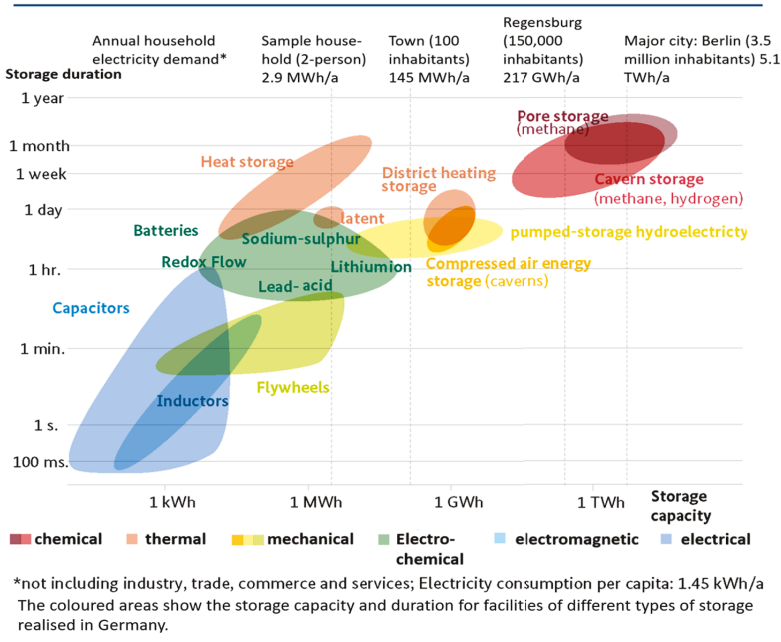


Figure 1.1: Schematic representation of energy storage by various devices as a function of time [5]

1.1 Solid Oxide Cell (SOC) and its components

Solid Oxide Cell (SOC) is an electrochemical device which can operate in both fuel producing and power producing modes, ideally at 800 °C [6]. The fuel producing mode is called solid oxide electrolyzer cell (SOEC), which converts electrical energy into chemical fuel whereas the power producing mode is called solid oxide fuel cell (SOFC) (Figure 1.2) which converts chemical energy into electrical energy, i.e. reverse operation of SOEC. These SOCs consist of an anode and a cathode, which are separated by a ceramic electrolyte. The anode–electrolyte–cathode assembly is commonly called as a cell. The voltage produced by a single cell during operation is approximately in the range of 0.6–0.8 V [7], which is quite low (for example, the

voltage required for a mobile phone is typically 5 V). So, the voltage produced by a single cell is of no practical use. Therefore, SOC must consist of multiple cells connected either in series to provide the required voltage or in parallel to produce the required current for a reasonable purpose. For this, a component called interconnect is used which integrates the individual cells to form a stack [8]. As a result, the overall voltage is increased and becomes technically useful for practical applications. In these cells, fuel is supplied in the fuel chamber and air is supplied in the air chamber. The component exposed to fuel side undergoes reduction whereas on air side it undergoes oxidation reactions [6]. Here a brief overview of the various components of a SOFC and the material requirements is provided to set the scientific background and introduce the main concepts pertinent to this work.

1.2 Materials for SOC

All the components of SOC devices are in solid state and are primarily made of either alloy, ceramics and/or cermets (ceramic + metal composites). The materials of all the SOC components must also be physically, chemically and thermally compatible with the other components in the device, especially when exposed to the high temperatures.

1.2.1 Anode

The material used as anode requires not only high electronic and ionic conductivities, but must also be stable in the oxidizing environment. Metals are mostly preferred as anode materials as they catalyze the anode reaction, especially Ni, owing to its abundance and affordability [6]. However, due to its high coefficient of thermal expansion (CTE), it is not directly used; instead it is used to make composites of Ni–YSZ (yttria stabilized zirconia). Addition of YSZ serves dual purpose; providing superior ionic conductivity and enhancing anode–electrolyte attachment. Currently, porous Ni–YSZ cermet is commonly used as anode material for SOC devices because it is a good current collector and acts as catalyst for oxidation reactions [9, 10].

1.2.2 Cathode

The most important reaction in case of SOFC operation is the reduction of oxygen at the cathode and subsequent transport of oxygen ions to the anode through the electrolyte. The materials used as cathode must be porous so that oxygen molecules are permeated easily to reach the solid electrolyte [6, 7], have high ionic and electronic conductivities and have high catalytic activity for oxygen reduction reaction. Nowadays, the most commonly used material

for cathode is lanthanum manganite (LaMnO_3), a perovskite structure (ABO_3) based p-type ionic compound [11, 12]. This material is typically doped with rare earth elements like Sr, Ce and Pr in order to enhance the electrochemical properties like the ionic conductivity. Most frequently it is doped with Sr as $\text{La}_{1-x}\text{Sr}_x\text{MnO}_3$ (LSM) and this increases the ionic conductivity by 10–100 times as compared to the undoped perovskite LaMnO_3 whose conductivity is 10 S/cm (at 700 °C). The CTE values of the cathode should be close to that of electrolyte material in order to avoid thermal stresses [13] and LSM is a good candidate from that point of view as well.

Perovskite materials with high oxygen permeability and high electro-catalytic activity are a group of materials based on Fe and Co, for example $(\text{La, Sr})(\text{Co, Fe})\text{O}_3$ (LSCF) [14]. However, these materials have to be selected carefully for use as an electrolyte material since they have notably higher CTE as compared to the commonly used 8 mol % yttria-stabilized zirconia (8YSZ).

1.2.3 Electrolyte

Once the molecular oxygen (O_2) is converted to oxygen ions (O^{2-}), it must migrate through the electrolyte to the fuel side (anode side in SOFC or cathode side in SOEC) of the SOC [14] to combine with the H^+ ions to produce water vapor. In order for the migration of O^{2-} ions to happen, the electrolyte must have high ionic conductivity and no electronic conductivity. Also, it should be fully dense to avoid escape of reacting gases and be as thin as possible to minimize resistive losses in the cell [13]. The ideal electrolyte for SOCs can be stable, O^{2-} or H^+ conducting ceramics. There are numerous potential ceramic materials which can be used: for example, YSZ, doped bismuth oxide and doped cerium oxide [7] etc. Among all these materials, YSZ has emerged as a highly suitable electrolyte, due to its thermally stable structure, high ionic conductivity resulting from the high levels of metal oxide doping (which facilitates O^{2-} vacancy formation).

1.2.4 Interconnects

Interconnect is one of the main components of SOC devices which provides electrical connection between two cells and grouping of single cells together to form a stack [15]. It acts as a physical barrier to protect the anode and cathode materials from being deteriorated in oxidizing and reducing atmospheres, respectively (Figure 1.2). It also provides mechanical support and stability to the stack. Additionally, it gives major thermal conduction path for heat distribution in the fuel cell stack. Thus interconnect performance is of vital importance

to the overall SOC performance and the key requirements for an interconnect material are summarized below [15]:

1. high electrical conductivity,
2. high thermal conductivity to reach a uniform heat distribution in the stack,
3. low mismatch of thermal expansion coefficient (CTE) with regard to the other components,
4. high density to avoid the mixing of fuel and air gases,
5. good mechanical strength and
6. very good corrosion resistance.

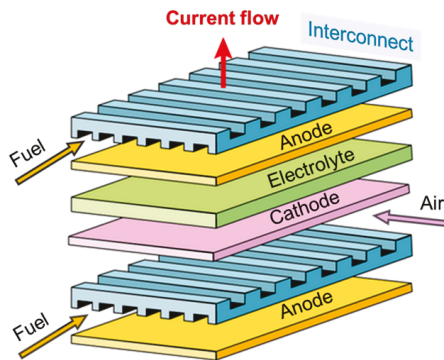


Figure 1.2: Schematic of an SOFC stack showing different components and relevant gas atmospheres (air and fuel).

High operating temperatures make ferritic stainless steels the most potential candidates for the interconnect material as their CTE is quite compatible with the other ceramic materials of different components of the cell. The Institute for Energy and Climate Research, Microstructure and Properties of Materials (IEK-2) at Forschungszentrum Jülich jointly with the industry partner, ThyssenKrupp VDM (now VDM Metals) had developed high-Cr (22 wt. %) ferritic stainless steels as an interconnect material for high temperature SOFC applications [16, 17]. This collaboration produced a new interconnect steel, now commercially available as Crofer® 22 H [18]. As SOFCs operate in the range of 700–800 °C, the oxides formed during high temperature exposure must be electrically conducting. In Crofer 22 H typical deoxidizers (added to molten steel) like Al and/or Si were brought to minimum levels so that the formation of electrically insulating oxide layers (alumina or silica) can be avoided on the alloy surface [19]. Relatively small amounts of W and Nb were added to improve the creep strength as they

tend to form intermetallic precipitates, called Laves phase [17] of composition $(\text{Fe, Cr})_2(\text{Nb, W})$ well distributed in the ferrite matrix of Crofer 22 H.

However, it must be highlighted that understanding the oxidation behavior of interconnect materials under actual operating conditions remains insufficient. This prevents efficient compositional tailoring for further improvement of the alloy properties, particularly its high temperature oxidation resistance. The key aspect here is understanding the role of different SOC-relevant atmospheres on one hand and of the alloy constituents on the high temperature oxidation mechanisms on the other hand.

2 Scientific Background

The objective of this chapter is to give a summary on the theory of oxidation of metals and alloys in general as well as fundamentals of high temperature oxidation process from the viewpoint of thermodynamics and kinetics.

The review continues with an in-depth inspection of different high-Cr ferritic steels and their oxidation behavior relevant to SOEC/SOFC interconnects applications and the gaps in the literature on these materials are highlighted.

In the third part, special importance has been given to characterization techniques suitable for studying thermally grown oxides such as XRD, SEM, GD-OES and TEM. The usefulness of these techniques as well as their drawbacks are discussed. Further, the importance of high resolution and high sensitivity techniques like an atom probe is reviewed, including the earlier attempts to characterize thermally grown oxides.

2.1 An overview of metal oxidation theory

A reaction between a metal (M) and an oxygen gas molecule (O_2) to form an oxide (M_xO_y) can be written as:



The above metal oxidation reaction may seem to be the simplest, yet it depends on a variety of factors and the associated mechanisms are often complex. Several simplifications were made to understand the high temperature oxidation process [20] as shown in [Figure 2.1](#). The key stages of metal-oxygen reaction at high temperatures are:

1. The prime and initial step in metal–oxygen reaction requires adsorption of molecular oxygen on the clean metal surface.
2. As the reaction continues, molecular oxygen dissociates into oxygen atoms which may dissolve in the metal, leading to formation of oxide nuclei on the metal surface.

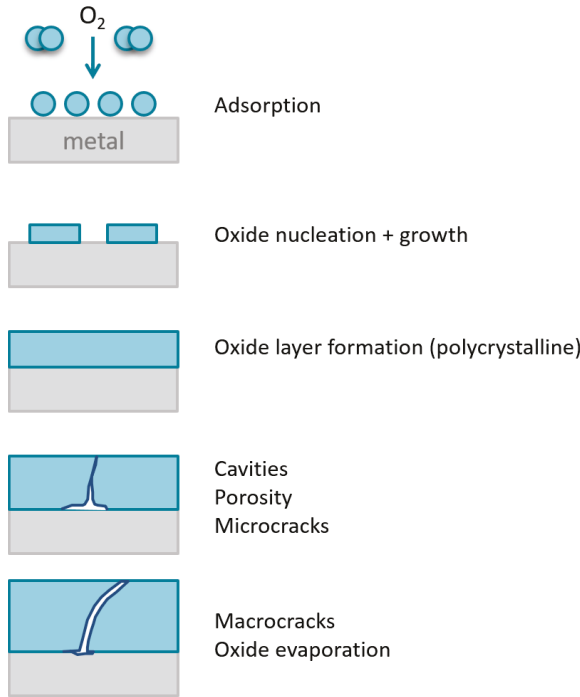


Figure 2.1: Schematic showing various stages of metal–oxygen reactions during high temperature exposure [20].

3. The metal is separated from the gas atmosphere when the oxide is continuous and thick enough on its surface. Further reaction (oxide growth) can occur mainly via solid state diffusion of the reacting species (metal and/or oxygen) across the thick oxide layer. For thick oxides grown at high temperatures, the driving force for oxide growth is the chemical potential gradient created across the oxide layer.
4. Certain metals which may form porous oxides are not grown via solid state diffusion, instead, the surface reaction mechanism is the prevailing one. At elevated temperatures such oxides can become either liquids or volatile, making the oxide layer less protective (e.g. Mo and W based oxides).

5. The reaction mechanism for a particular metal–oxygen system is a function of the temperature, gas composition, oxygen partial pressure, exposure time, surface state and microstructure of the metal.

One of the fundamental yet important questions in corrosion science is whether or not a chemical reaction between a metal and its surrounding atmosphere can occur. This can be addressed by considering the thermodynamics of high temperature oxidation.

2.2 Thermodynamics of high temperature oxidation

From the laws of thermodynamics, the tendency for the reaction shown in Equation (2.1) to proceed either in forward (oxidation) or backward (reduction) reaction can be retrieved. If temperature and pressure are constant, the stability of a reaction is determined based on its Gibbs free energy (ΔG) [21], which is a measure of thermodynamic driving force and is shown here:

$$\Delta G = \Delta H - T\Delta S \quad (2.2)$$

where ΔH is the change in enthalpy, ΔS is the change in entropy and T is the temperature.

Gibbs free energy tells whether a reaction is spontaneous, non-spontaneous or if equilibrium is established, as shown below.

- (i) $\Delta G < 0 \implies$ forward reaction is spontaneous. Oxidation of metal is more probable.
- (ii) $\Delta G > 0 \implies$ backward reaction is spontaneous. Reduction of metal oxide is expected.
- (iii) $\Delta G = 0 \implies$ equilibrium between forward and backward reaction is anticipated.

In case of metal oxidation (case (i) above), following the law of mass action, the change in Gibbs free energy for the reaction in Equation (2.1) becomes:

$$\Delta G = \Delta G^\circ + RT \ln \left(\frac{a_{M_xO_y}}{a_M^x a_{O_2}^{\frac{y}{2}}} \right) \quad (2.3)$$

where, ΔG° is the Gibbs free energy at its standard state, R is the universal gas constant, T is the temperature and a is the activity of each component. For pure solids, i.e., both metals and oxides, the activity (a) can be set equal to unity. At high temperatures and moderate pressures, gases can be approximated by the ideal gas law and their activities can be expressed in terms of their partial pressures (p). Therefore, the terms $a_{M_xO_y}$ and a_M^x become equal to 1, whereas

a_{O_2} becomes p_{O_2} . Then the above reaction (Equation (2.3)) can then be simply written as:

$$\Delta G = \Delta G^\circ - \frac{y}{2}RT \ln(p_{O_2}) \quad (2.4)$$

When the system is in equilibrium (i.e. when $\Delta G = 0$), the above equation can be rearranged as:

$$p_{O_2}^{diss} = \exp\left(\frac{\Delta G^\circ}{yRT}\right) \quad (2.5)$$

where, $p_{O_2}^{diss}$ is known as dissociation pressure of the oxide which is in equilibrium with the metal. This is also the minimum oxygen partial pressure necessary for a metal to form its thermodynamically stable oxide.

The value of dissociation pressure for a particular oxide can be retrieved from the Ellingham diagram (Figure 2.2), which is a plot of the standard Gibbs free energy (ΔG°) for an oxide as a function of temperature (T) at standard state ($p_{O_2} = 1$ atm). This plot aids in understanding the stability of oxides at any given condition. The ΔG° is more negative towards the bottom of the diagram and the lower the oxide line is located, the more stable the oxide is. The point where a straight line drawn from index point O in Figure 2.2, i.e. from $(\Delta G^\circ, T) = (0,0)$, intersects any particular oxide line at a particular temperature gives the dissociation oxygen partial pressure ($p_{O_2}^{diss}$) for that oxide at that temperature. It can be seen from Figure 2.2 that the lower the free energy of an oxide, the lower is its dissociation pressure and hence, the oxide is thermodynamically more stable. Conversely, with the increase in temperature, the Gibbs free energy also increases (towards the top of the Ellingham diagram), indicating that the oxides become thermodynamically less stable. For instance, Ni oxidation to NiO at 800 °C requires minimum oxygen partial pressure of $\sim 10^{-14}$ atm, whereas at the same temperature the oxides of Cr and Al (Cr_2O_3 and Al_2O_3 , respectively) require dissociation pressures of $\sim 10^{-26}$ atm and $\sim 10^{-42}$ atm respectively, indicating that it is thermodynamically relatively difficult to resist the formation of Cr- and Al- oxides. One should, however, remember that the $p_{O_2}^{diss}$ values attained from this figure are for unit metal activity i.e. for pure solids. In the case of alloys, the solute species which undergo oxidation would always have the activity lower than unity, i.e. higher oxide dissociation partial pressure.

It is also evident from the Figure 2.2 that oxides of Fe, Ni, and Co, which are the base metals for majority of the engineering alloys, are considerably less stable than the oxides of solutes such as Cr, Al and Si. When one or more of these solute elements are added to Fe, Ni, or Co,

internal oxidation of the solutes is more likely to occur, provided the concentrations are relatively low. If the solute concentrations in such alloys increase to a significantly high level, the oxidation mechanism shifts from internal to external scale formation. This process is known as *selective oxidation*. Most of the Fe, Ni and Co based alloys depend on selective oxidation of chromium to form Cr_2O_3 layer for good oxidation resistance. This is the primary reason why stainless steels are called *stainless* due to the high content of Cr that leads to protective Cr_2O_3 layer formation on the alloy surface. Al is intentionally added to certain alloys to grow Al_2O_3 scale for better oxidation resistance at slightly higher temperatures as compared to Cr addition.

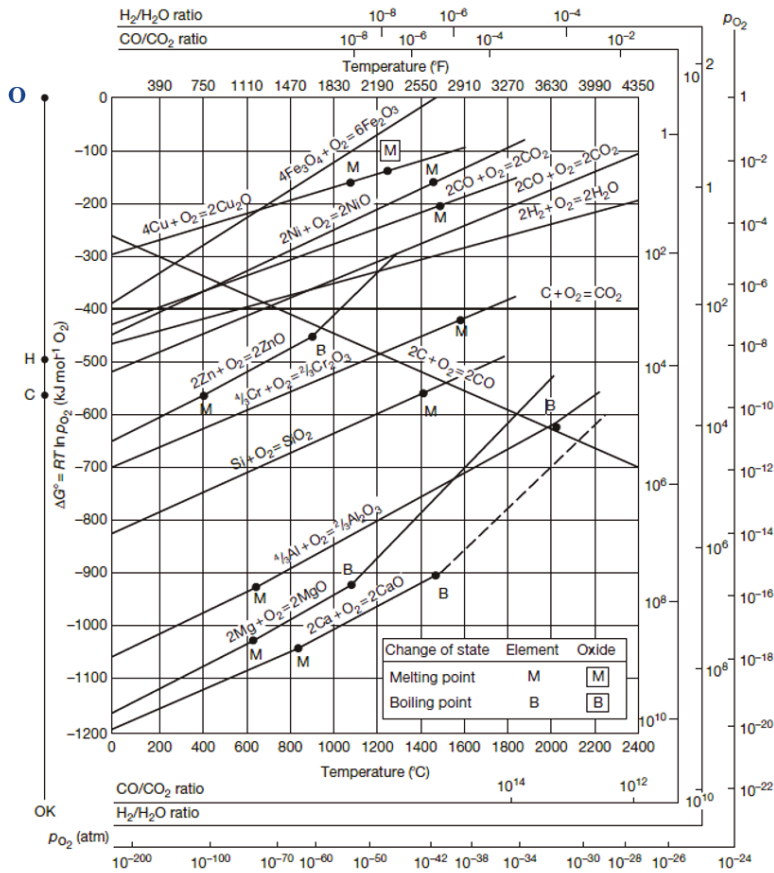


Figure 2.2: Ellingham diagram for several metal oxides based on their Gibbs free energy as a function of temperature [21]

2.3 Kinetics of high-temperature oxidation

Thermodynamics provides information on the feasibility of a reaction but kinetics of a reaction is also important to consider as it provides valuable information about the rate of oxidation (speed at which corrosion takes place) of a metal or an alloy. Two primary stages associated in the oxidation process are nucleation and growth. Nucleation of oxide is the very early stage of oxidation, which is also referred to as *transient oxidation*. In the latter stages, the growth of oxide results in a continuous and thick scale development on the metal surface as shown in Figure 2.1 and the mechanism by which the reactants move through the oxide layer is very important to understand.

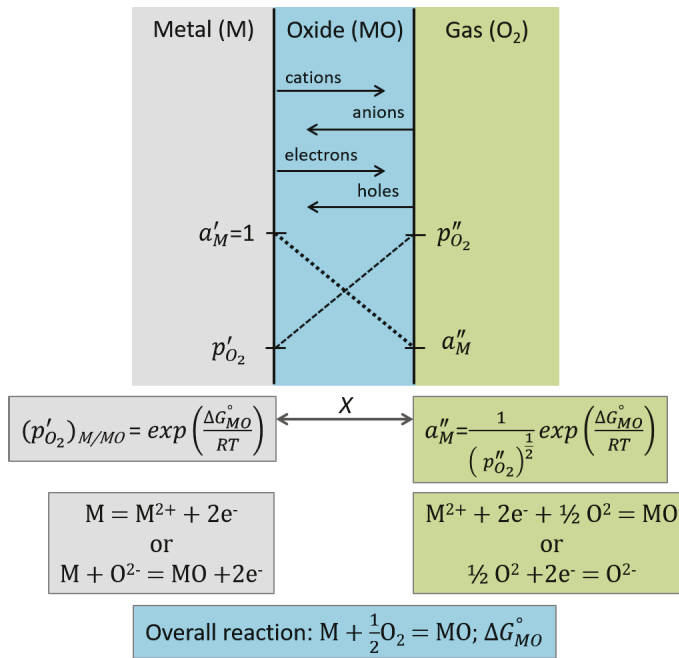


Figure 2.3: Wagner’s model of high-temperature oxidation [21].

A simplified model of mass transport process across an oxide scale formed during high temperature exposure is schematically shown in the Figure 2.3. The metal at the metal-oxide interface undergoes oxidation by producing metal cations and electrons, which diffuse through the oxide scale and reaches the gas-oxide interface, resulting in oxide scale formation. This mechanism is known as *outward growth of oxide scale*. Alternatively, the oxygen molecules at the gas-oxide interface undergo reduction by forming oxygen anions and electron-holes

which diffuse through the oxide scale and react with the metal at metal-oxide interface. This mechanism is known as *inward growth of oxide scale*.

Wagner's theory of oxidation [22, 23] postulated that growth of oxide scale takes place via mass (cations and anions) transport and is governed by the parabolic rate law. The theory proposed by Wagner was based on several assumptions: the oxide is compact and maintains good adherence to the metal substrate and the local thermodynamic equilibrium is attained both at the scale-gas interface and metal-oxide interface when a certain thickness of the oxide scale was developed. As the scale thickness x increases with the time t , the diffusion distance also increases and the rate of oxidation decreases, thus resulting in parabolic kinetics.

The parabolic rate law relevant to oxide growth can be written as [20]:

$$\frac{dx}{dt} = \frac{k_p}{x} \quad (2.6)$$

where x indicates the oxide scale thickness (μm), k_p is the parabolic rate constant $\text{cm}^2 \text{s}^{-1}$ and t is the oxidation time.

By integrating the above equation Equation (2.6) and assuming $x = 0$ at $t = 0$ the standard form of parabolic rate law is obtained;

$$x^2 = 2k_p t \quad (2.7)$$

Most of the times, either the oxide scale is not uniform or, especially at early stages, the thickness is not measurable without using high resolution techniques. Therefore, the oxide scale growth is commonly and widely represented by measuring the specific weight change (weight change per unit surface area). The corresponding parabolic rate law can be expressed as following [24]:

$$\left(\frac{\Delta m}{A}\right)^2 = 2k_w t \quad (2.8)$$

where Δm is the mass gain, A is the surface area of the sample and k_w the instantaneous parabolic rate constant.

For a simple oxide of M_xO_y type, the relationship between k_p and k_w is as shown below [20]:

$$k_w = \left(\frac{y \cdot W_O \cdot \rho_{M_xO_y}}{V_{M_xO_y}} \right)^2 \cdot k_p \quad (2.9)$$

where W_O is molar weight of oxygen, $\rho_{M_xO_y}$ is density of M_xO_y and $V_{M_xO_y}$ is molar volume of the oxide.

As explained above, the oxidation kinetics, including the parabolic rate constant, can be experimentally determined based on the weight gain attained by a sample during high temperature oxidation. However, for deeper understanding regarding the mass transport across the oxide scales, just the determination of rate constant is insufficient. Understanding the oxide structure, including pathways responsible for mass transport, is one of the key aspects to identify the responsible mechanisms of high temperature oxidation, as discussed next.

2.4 Development of high-Cr ferritic steels for SOC interconnects

As introduced earlier, ferritic steels are the ideal candidates for interconnect materials to be used at high temperature conditions by virtue of their stability, affordability as well as compatible values of coefficient of thermal expansion (CTE). The formation of an oxide layer as the reaction product, which acts as a protective coating between the steel and the atmosphere, is critical in making these ferritic steels employable and durable for the harsh service environments. From the stand point of protectiveness of the oxide scales, high temperature steels are generally categorized as Cr_2O_3 or Al_2O_3 forming [24]. Since Cr_2O_3 is a semiconductor compared to insulating Al_2O_3 , Cr_2O_3 forming steels with marginal amount of Al are chosen as ideal candidate materials for SOFC interconnect applications [25].

In gas compositions with pO_2 value close to atmospheric pressure and under temperatures < 1000 °C, evaporation of Cr_2O_3 in the form of CrO_3 or $CrO_2(OH)_2$, is a severe problem and is commonly referred to as *Cr₂O₃ poisoning* [6]. This effect limits the suitability of these steels as interconnects [26], as there is a continuous degradation of the oxide layer on the surface. Therefore, Mn is added to these steels as it can form an additional layer, $MnCr_2O_4$ spinel on top of the Cr_2O_3 , which protects the steels from being poisoned. However, Cr content is still maintained at high levels (usually > 20 wt. %) in order to provide the Cr reservoir for the formation of Cr_2O_3 [27] as well as $MnCr_2O_4$ ($MnO + Cr_2O_3$). Therefore, high-Cr ferritic steels

of the Fe–Cr–Mn base are currently used as construction materials for SOFC interconnects [26].

One major drawback of these steels is their poor mechanical strength at the high operating temperatures of SOFC (ideally at 800 °C [27, 28]). To overcome this, refractory elements such as Nb and W are added to high-Cr ferritic steels for two purposes: firstly, they improve the mechanical strength at elevated temperatures and secondly, CTE of the interconnect becomes compatible with that of the other ceramic components in the SOFC [27]. The electrical conductivity of the surface oxide scales remains almost the same as that for the Nb/W-free alloys [29]. It was also found that W addition had no effect on the oxidation behavior in the temperature range 800–900 °C, whereas Nb addition has a detrimental effect by lowering the oxidation resistance [27]. However, the oxidation mechanisms pertinent to effect of Nb addition are poorly understood so far [30].

The adverse effect of Nb-addition on the oxidation resistance is alleviated by intentionally adding Si (though it is also a technological impurity) [31]. Si binds Nb in the steel and promotes Laves phase formation, resulting in better mechanical strength at high temperatures. Though this is the desired objective, Si tends to form an oxide layer at the metal–oxide interface which make the ferritic steel nonviable for interconnect applications due to the electrically insulating nature of the silicon oxide [32]. Therefore, the amount of Si addition in the steel is very critical and must be carefully chosen.

The combined additions of Nb, W and Si result in an alloy with better oxidation resistance, CTE comparable to the other ceramic components in the SOFC device and good mechanical strength at high temperatures [27]. Additionally, Ti is also added for obtaining fine internal oxide precipitates of titania in the metal matrix at the vicinity of metal–oxide interface, which results in sub-surface strengthening [33]. This diminishes the tendency for surface wrinkling, which is caused due to thermal cycling [19]. However, the effect of Ti on external oxide scale formation is yet poorly understood.

In addition to the role of individual elements, like Nb, W, Si, Ti discussed above, the *interplay effect* (i.e. the effect of one element on the other) on high temperature oxidation is so far poorly understood. Yet this is very crucial for understanding the oxidation behavior as well as for the optimization of alloy composition. In this work systematic studies are performed to investigate the individual effect as well as the complex interplay between the individual alloying elements

on the high temperature oxidation behavior in different model gas compositions pertinent to SOC interconnect applications.

2.5 Reactive element (RE) effect in high-Cr ferritic steels

So far the importance of addition of various alloying elements and their contributions towards the interconnect stability and performance at the high temperatures through a protective oxide layer formation have been discussed. However, in spite of all these measures, any cracks or pores in this protective oxide layer can lead to its failure (oxide scale spallation) and permit oxygen penetration to the metal surface, leading to rapid oxide growth, which is highly undesirable from mechanical stability standpoint. One of the routes by which this can be surmounted is by adding reactive elements such as Y, La, Ce, and Hf to the steels which results in microstructure refinement and defect formation that modify the inclusions, which in turn aid in promoting strength and toughness of the steels [29]. John Stringer was credited for coining the term *reactive element* (RE) effect to replace *rare earth* effect to better describe the positive effect of oxygen-active elements on high-temperature oxidation [34].

Addition of the REs can also tackle the detrimental effects of the presence of sulfur, a naturally occurring steel impurity, on the steel properties [35–37]. Most of the steels are susceptible to stress corrosion cracking caused by sulfur by forming sulfide inclusions either at the grain boundaries in steel or at the metal–oxide interface during high temperature exposures. RE addition hinders sulfur segregation at the metal–oxide interface through binding with sulfur to form RE–sulfide [38], leading to the remarkable effect of enhancing the adherence of oxide scale to the underlying alloy [39–42].

In the presence of REs, the oxidation rate can dramatically diminish by a factor of 100 [43] and the amount of RE added to the alloys tremendously influences the oxidation rate. The inward diffusion of oxygen becomes predominant by the presence of reactive elements in the alloys [44–46] as REs have relatively higher affinity towards oxygen. The concentration of reactive elements in the alloy necessary to produce RE effect is typically in the range of 0.1–0.2 at. %. When added in quantities above a critical value (usually above 1 at. %), the REs tend to manifest undesirable effects, including a substantial increase in the oxidation rate [47, 48]. This *overdoping* is possibly due to the presence of oxygen vacancies in the RE oxides, resulting in increased oxygen diffusion. In case of overdoping, RE ions diffuse rapidly through the oxide scale via grain boundaries, resulting in lower obstruction for the Cr transport (see Figure 2.4), thus reducing the effect of RE on slowing oxide growth [49].

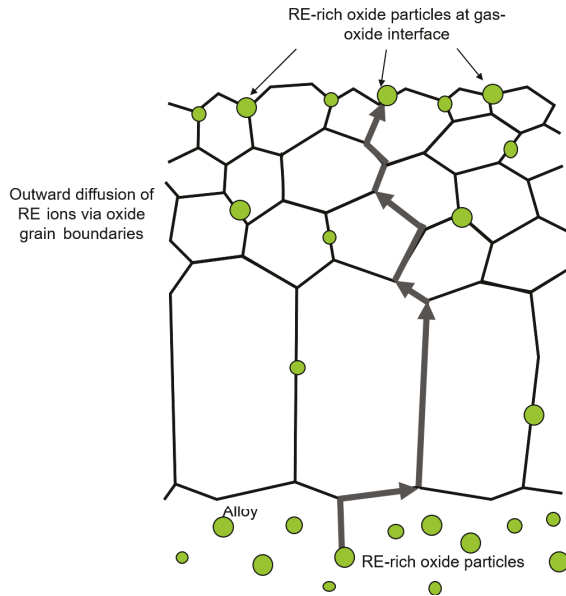


Figure 2.4: Schematic of detrimental effect of RE during high-temperature oxidation. RE ions diffuse outwards from the underlying alloy via oxide scale grain boundaries and become enriched at the gas-scale interface (surface) [49].

From Figure 2.5 it is evident that RE addition curtails the oxide scale growth as compared to a no-addition Fe–24Cr ferritic steel. Among the REs, La addition seems to be more effective in hindering the oxide growth as compared to the other elements like Ce, Y and Zr. The prime reason for Ce, Y and Zr exerting less influence in comparison to La is due to the nearly nil-solubility of earlier elements in the Fe-matrix, resulting in Fe-rich intermetallic precipitates like $\text{Fe}_{17}\text{Ce}_2$ and Fe_{17}Y_2 (precipitate strengthening). These precipitates form at the alloy GBs and undergo oxidation when exposed to high temperatures, thus restricting doping into the chromia scale. On the other hand, La doesn't form intermetallic precipitates with Fe and at 800 °C, it can dissolve in the BCC α -matrix up to a concentration approximately 0.5wt. % (solid solution strengthening).

Though RE addition leads to improvements in the oxide adherence and slow oxide growth, the mechanism for these is still unclear and near-atomic scale information is essential for any attempts to resolve this. In general, REs are present in trace quantities and hence, the detection of RE is very difficult within the oxide scale and to accurately identify location of the RE within the thermally grown (TG) oxide scale, one needs high resolution techniques [50–52].

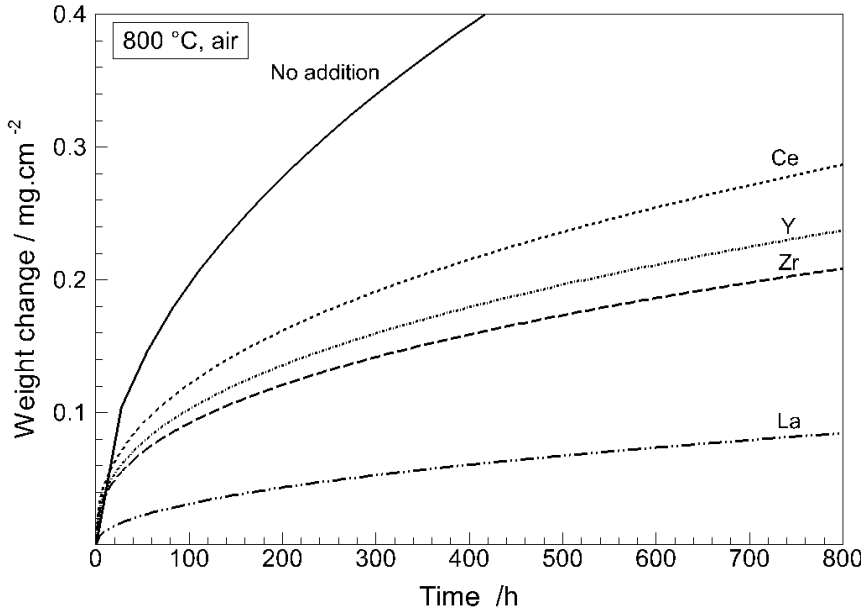


Figure 2.5: Weight gain plot of Fe-24Cr alloys containing reactive element additions such as Ce, Y, Zr and La during oxidation at 800 °C in air (Ar-O₂) [29]

So far the alloy chemistry and its modification affecting the oxidation behavior were discussed. However, different gas compositions on either side of the interconnect, in which it operates, is another key aspect affecting the overall SOC performance and is discussed in the following section.

2.6 Effect of gas composition on interconnect oxidation

In SOFC, the interconnect on the cathode side is exposed to air (Ar-O₂) and on the anode side to fuel at operating temperature 800 °C. Most studies regarding metallic interconnect corrosion have been performed in air (Ar-O₂) and in H₂ or H₂-H₂O, since H₂ is an established fuel gas [53]. Earlier studies on high temperature oxidation of chromia formers in Ar-O₂ atmosphere showed that the formation of oxide scales was dependent on the partial pressure of oxygen (p_{O_2}) [54, 55]. Decrease in the p_{O_2} of such gases (Ar-O₂) showed lower oxidation rate and improved oxide-metal adhesion. However, very different behavior was observed in low p_{O_2} gases like Ar-H₂-H₂O (decrease in p_{O_2} can be achieved by increasing the ratio of H₂/H₂O). Lowering the p_{O_2} in Ar-H₂-H₂O gases resulted in higher oxidation rates, and the Cr₂O₃ grains were much smaller in the low p_{O_2} gas (H₂-H₂O) compared to the high

pO_2 (Ar–O₂) gases. This is due to the water vapor in low pO_2 gas getting adsorbed and dissociated faster at the outer surface compared to O₂, which promotes the inward oxygen anion transport to the oxide-metal interface. Though the increased oxygen grain boundary diffusion is postulated to be the dominating mechanism, the transport of H₂ and H₂O in the form of molecules through the chromium oxide could also activate and contribute to the inner oxide growth.

Sometimes, cheaper alternatives to H₂ fuel are utilized. Hydrocarbon based fuel (syn-gas) is one of the choices based on its availability. It consists primarily of H₂ and CO with significant amount of H₂O and some levels of CO₂. When hydrocarbon-based fuels are used in SOFC, the reforming gases such as CO–CO₂ may come in contact with the interconnect alloys. Therefore, these gases can affect the oxidation mechanism and the stability of oxide scales. Several ferritic steels were studied individually in each gas composition. For instance, several authors have studied interconnect oxidation behavior in air atmospheres [56–59]. On the other hand, in the anode side atmosphere, some authors reported on the high temperature oxidation of Fe–Cr alloys in H₂–H₂O [60, 61]. There are a few high temperature oxidation studies in CH₄–H₂O [62, 63] but there are very limited studies pertinent to CO–CO₂ [43] gases, particularly on the commercially used high–Cr ferritic steels. There are studies describing the interconnect oxidation behavior in syn-gas [4–7] but very limited work was performed for CO–CO₂ gas atmosphere.

Earlier studies on chromia forming steels in H₂–H₂O showed that water molecules tend to adsorb on the Cr₂O₃ grain boundaries, altering the transport properties [54]. Similar mechanisms must be responsible for the oxidation behavior in CO–CO₂, as these gases (low pO_2) provided a faster oxidation rate [64]. The transport properties along the chromia grain boundaries can affect the oxide scale kinetics and its microstructure and grain size [53]. As these gaseous species alter the transport properties across the chromia grain boundaries, this may also be related to the diffusion and segregation of minor alloying elements along them. Therefore, this work focuses on the effect of gas compositions on high temperature oxidation of high–Cr ferritic steels. Specifically, four different commercially available high–Cr ferritic steels were studied in Ar–O₂, Ar–H₂–H₂O and Ar–CO–CO₂ atmospheres, with special emphasis on the effect of gas composition on chromia scale growth and the transport properties.

In addition to external oxide scale formation, these ferritic steels also undergo internal oxidation (in the metal matrix) due to the presence of active elements which, even if present in

minor amounts, are responsible for internal oxidation zone (IOZ) formation. The literature review of these aspects are discussed in the next section.

2.7 Internal oxidation

Internal oxidation is one of the material degradation processes in which the oxide particles are formed with the less noble alloying elements [24]. The internal oxidation can occur in any alloy system, if the amount of active elements in the alloy is below a critical concentration and at temperatures $> 400\text{ }^{\circ}\text{C}$ [65, 66]. Internal oxidation is mainly a diffusion-controlled process i.e. it obeys parabolic rate law. This process is always controlled by the oxygen diffusion from the surface through the external oxide [67]. The active elements present in this zone lead to oxide particles formation, and it is commonly referred to as internal oxidation zone (IOZ).

During internal oxidation, the oxides of alloy solutes can be formed as either fine particles precipitated within the alloy matrix (grain interior) [24], or as coarse particles preferentially precipitated at the crystal defects, like alloy grain boundaries [68, 69]. Occasionally, these oxide precipitates can offer strengthening mechanism in the subsurface regions of an alloy [70]. However, they can also lead to premature failure in this alloy zone due to crack formation at the matrix-oxide particles' interface [68]. Therefore, internal oxidation should be also considered together with the external scale formation for a complete understanding of the oxidation behavior. Considering the high-Cr ferritic steel family based on Fe-22Cr-0.5Mn steels, the active elements in the materials could be one or more of the following; Ti, Nb, Si and Al. When the concentration of these reactive elements is below a critical concentration, it can lead to internal oxidation by forming TiO_2 , NbO_2 , SiO_2 and Al_2O_3 particles in the alloy matrix at the vicinity of metal-oxide interface, which exists up to a certain depth in the alloy, and the chemical analysis of these internal oxidation products is very important.

So far different aspects affecting the oxidation behavior have been discussed. All these mechanisms/processes are related to the oxide microstructure during high temperature exposure and associated with the mass transport through the oxide scale. Therefore, it is of key importance to understand the diffusion pathways responsible for oxide growth mechanisms.

2.8 Diffusion and mass transport in thermally grown oxide

Metals and alloys exposed to high temperatures often show the formation and growth of a continuous external oxide scale and/or the internal oxidation of the less-noble solutes. Mass transport through the oxide scale is vital for understanding the growth kinetics for both exter-

nal scale growth and internal oxidation processes. The shortest transport pathways for ions to diffuse through the oxide scale are referred to as *short-circuit diffusion* paths which could be defects such as dislocations, grain boundaries and triple junctions [71]. Therefore, the overall oxidation kinetics may be substantially influenced by the presence of these defects, and it is very essential to study oxide microstructure to understand the oxidation processes [20].

The transport processes along *short-circuit diffusion* pathways are easier and faster due to the relatively more open structure compared to the lattice. Local stresses and strains associated with these defects can be reduced to some extent by the segregation of diffusing constituents. Segregation of diffusing constituents often affects the diffusion processes [43]. This is well recorded in the case of grain boundary diffusion [72]. Therefore, grain boundaries play an important role in the formation of thermally grown (TG) oxides on the alloy surface. The segregation of minor elements of an alloy to oxide grain boundaries prominently alters the oxide defect structure as well as the mass transport properties of the TG oxide. Additionally, interfacial reactions at the metal–oxide interface play a major role in the case of solid–state diffusion [73]. In the present context, the analysis of the metal–oxide interface is critical for understanding the oxide scale adherence as well as the electrical conductivity of the interconnect. All these require high resolution characterization techniques like transmission electron microscopy (TEM) and atom probe tomography (APT) for a holistic understanding on the process of high temperature oxidation. However, there is very limited work on these addressing the mass transport, segregation and linking this information to oxidation mechanisms.

2.9 Nanoscale characterization of thermal oxide scales

2.9.1 Transmission electron microscopy

Transmission electron microscopy (TEM) is one of the versatile materials characterization techniques used to reveal micro- and nano-scale features in a solid material. In short, it can be described as a study of the interactions between high-energy electrons, typically in the range of 100–300 keV, and an electron-transparent thin specimen. This interaction results in the generation of a number of different signals as shown in [Figure 2.6](#). These signals can be used for producing images, spectroscopic analysis for chemical information and diffraction patterns for structural information.

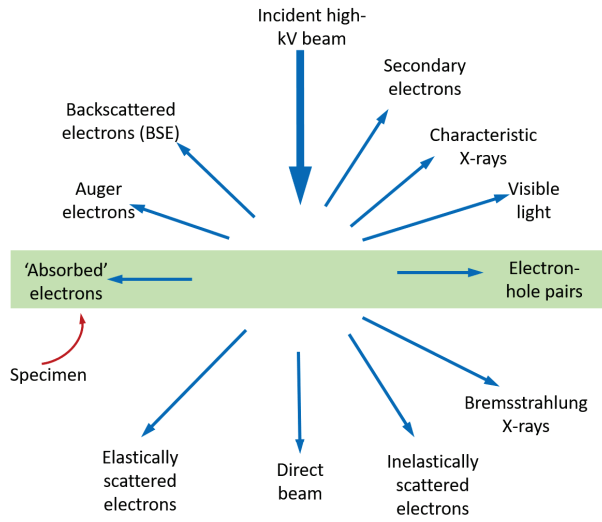


Figure 2.6: Schematic representation of various signals generated during the interaction of specimen with the incident electron beam.

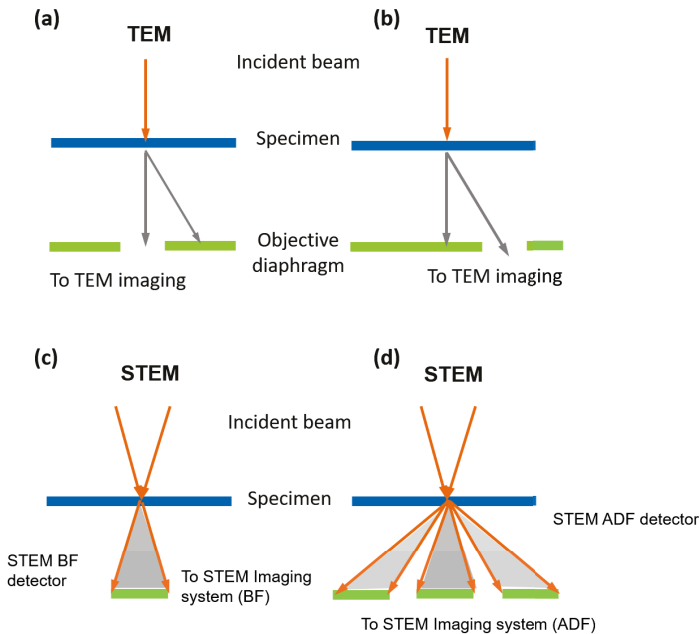


Figure 2.7: Schematic representation of various imaging modes in TEM. a) Bright-Field TEM, b) Dark-Field TEM, c) Bright-Field STEM and d) Dark-Field STEM. [74].

The two available types of TEM are: conventional TEM (CTEM) and scanning TEM (STEM) which differ principally in the way they address the specimen. The CTEM is a wide-beam technique, in which a close-to-parallel electron beam interacts with the region of interest and the image is produced by an objective (imaging) lens. With the help of diffraction pattern, either a direct beam (unscattered beam) called bright-field TEM (BF-TEM) or a scattered beam called dark-field TEM (DF-TEM) can be chosen for the formation of a real space image (see Figure 2.7).

In case of BF imaging mode, the contrast is improved by omitting diffracted electrons from the image. Regions of the specimen that absorb or scatter electrons (thick areas) appear darker. In case of DF imaging mode, only electrons scattered at a particular angle contribute to the real-space image. In this imaging mode, specimen regions with selected crystal orientation appear brighter and rest of the regions appear darker.

The STEM employs a fine focused electron beam, formed by a probe lens before the thin specimen, to address each pixel in series as the probe is scanned across the specimen. In STEM mode, apertures are not used. Instead a different detector which collects either the direct beam (BF detector) or the scattered electrons at a particular range of angles (annular dark-field (ADF) and high-angle annular dark-field (HAADF) detector) is used.

A Energy dispersive X-ray spectroscopy (EDX/EDS)

Chemical imaging in TEM can be made using X-rays, emitted by the target and the energy losses of inelastic transmitted electron [74]. The emission yield of X-rays increases with atomic number (Z), therefore, the chemical contrast of heavier elements is obtainable easily whereas for lighter elements, electron energy loss spectroscopy (EELS) is more accurate. Using the X-rays emitted from the specimen, chemical mapping is made by energy dispersive spectroscopy (EDS). The EDS detector is placed inside the objective lens at a target angle based on the TEM specimen holder.

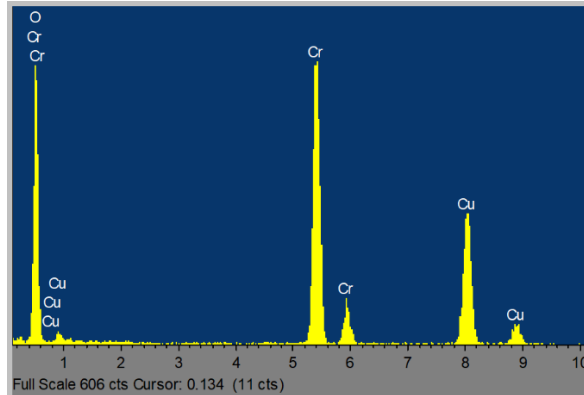


Figure 2.8: An example of EDS area analysis of the thermally grown chromia scale on ferritic steel.

Electrons of an inner core shell are pumped out via irradiation of the sample with the primary electron beam in electron microscopy (SEM or TEM). The escaped electron within the inner shell leads to an unstable arrangement and the hole is immediately occupied by an electron from the outer shells triggering X-ray emission in a specific energy range. The energy released is determined from the difference between the electron energies before and after the relaxation. The possible combinations are represented by the name of the final shell (K, L, M, etc.) mutually with a suffix (α , β , γ) which are characteristics of a particular element. Qualitative and quantitative information on elemental composition can be retrieved from this technique, as can be seen in Figure 2.8 (this spectrum corresponds to an area scan of a chromia scale formed on ferritic steels).

B Application to thermally grown oxide scales

Using several of these modes in TEM/STEM, thermally grown oxides can be characterized to retrieve microstructural information at the nanoscale [54, 75, 76]. The main purpose of using TEM, in case of thermally grown oxides, is to probe the oxide grain size, analyze elemental distribution and composition from EDS analysis and characterize the metal oxide interface. For example, Figure 2.9 shows a comparison of chromia microstructure in high and low pO_2 gases, where the grain size difference in both the atmospheres is clearly visible.

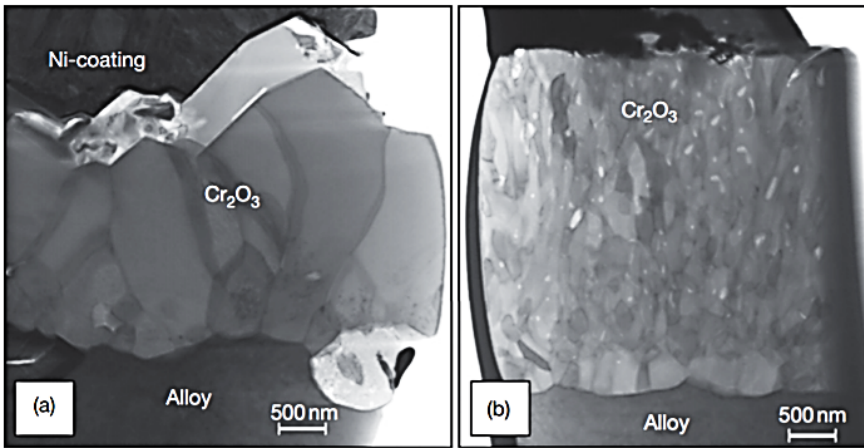


Figure 2.9: TEM micrographs of thermally grown Cr_2O_3 scales on Ni–25Cr at 1050 °C for 4 hours in (a) Ar–20% O_2 and (b) Ar–4% H_2 –2% H_2O atmospheres [54].

Though TEM provides valuable structural information, it is often not possible to obtain a reliable and especially quantitative information from a specific small and non-planar region like a grain boundary, as TEM is essentially a projection-based technique. Besides, analytical TEM methods usually suffer from poor detection sensitivity and low accuracy for chemical quantification. The typical EDS has a detection limit in the range of 1 wt. % [77], which is not enough to characterize the impurities which are usually < 1 wt. % in any material. Therefore, a combination of TEM methods (structural information) in conjunction with APT (chemical information) enables access to critical information on the local microstructure as well as the elemental composition of thermally grown oxides.

2.9.2 Atom Probe Tomography (APT)

Investigations of the thermally grown oxide scales and the metal oxide interfaces were performed by APT in the present study. This section contains an introduction and basic principles of this technique.

A Historical perspective

The development of atom probe began in 1935 by Müller [78], who devised the field electron emission microscope. After 20 years, with the invention of field ion microscope (FIM), atomic scale resolution was achieved. Afterwards, chemical identification of the field-evaporated

atoms of a material was made possible with the help of a coupled time-of-flight mass spectrometer. Obtaining real 3D space compositional data was made possible with the development of the position sensitive atom probe in the year 1988 by Cerezo *et al.*[79]. Later, the introduction of local electrode atom probe (LEAP) has offered considerably increased data collection rates, making it feasible to examine much greater volumes of the given material [80].

B Fundamentals

APT operates on the fundamental principles of field evaporation. When a sharp-tipped specimen is exposed to very high electric fields, the apex of the tip undergoes field evaporation, resulting in ripping off of the surface atoms, as shown in Figure 2.10. Under high electric field, these freed ions are accelerated towards a position sensitive detector (PSD) recording the (X, Y) hit position of atoms which are later back-projected to the specimen surface to retrieve the original ion location in the material. This field evaporation process is followed shortly after the field ionization event, which is stimulated by a combination of the standing voltage with either a voltage or a laser pulse [81]. When the electric field is adequate enough, the atom is dragged away from its location on the surface before one of its electrons is consumed (by the surface). Thus, freshly produced ion is accelerated towards the PSD with the help of the electric field. The electric field magnitude (F) is proportional to the applied voltage (V) and the specimen apex radius (R) as shown in Equation (2.10).

$$F = \frac{V}{kR} \tag{2.10}$$

where k is a field factor (constant), which accounts for the reduced electric field due to the specimen shape and the electrostatic environment [82].

The chemical identity of field-evaporated atoms is determined based on the mass-to-charge state ratios of ions using time-of-flight mass spectrometry.

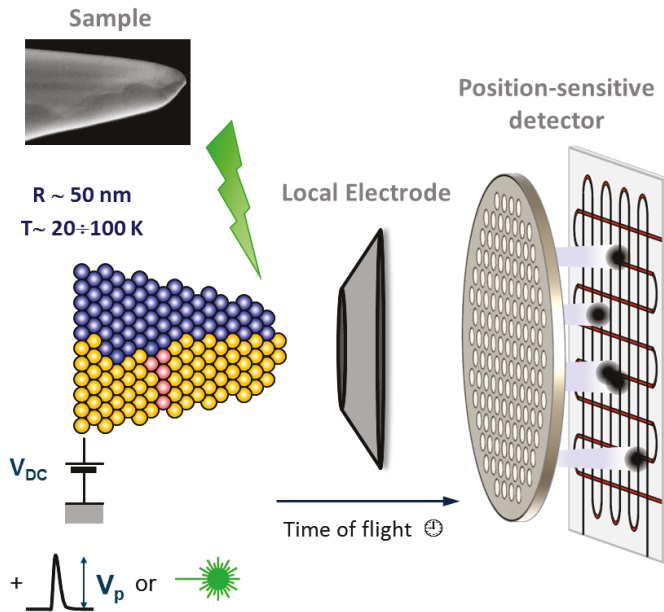


Figure 2.10: Schematics of specimen, local electrode and position sensitive detector in the analysis chamber of an APT instrument.

C Sample preparation

The APT measurement requires a sharp needle-like specimen to allow field evaporation of the surface atoms under high applied voltages. Suitable radius and shank angle of the specimen are the key requirements. A relatively smaller apex radius of the specimen could result in a lower starting voltage, which will affect the field of view. On the other hand, a larger apex radius would require higher starting voltages. Ideally, the apex radius of a specimen should be in the range of 50–100 nm [83] and the cross-section should be cylindrical. In order to avoid the possibility of premature fracture, the specimen surface should be free of protrusions and cracks [84]. To ensure that the region of interest is included within the obtained dataset, it should be located < 100 nm from the apex [85].

The developments in the FIB based lift-out technique enable the micro-fabrication of specimens from a wide range of materials [86]. Recently, the FIB based lift-out methods have been extensively applied to even electrically insulating materials [87]. The different steps involved in APT specimen preparation are shown in the Figure 2.11. More elaborate details of the sample preparation are available in the standard textbooks on APT [81, 88].

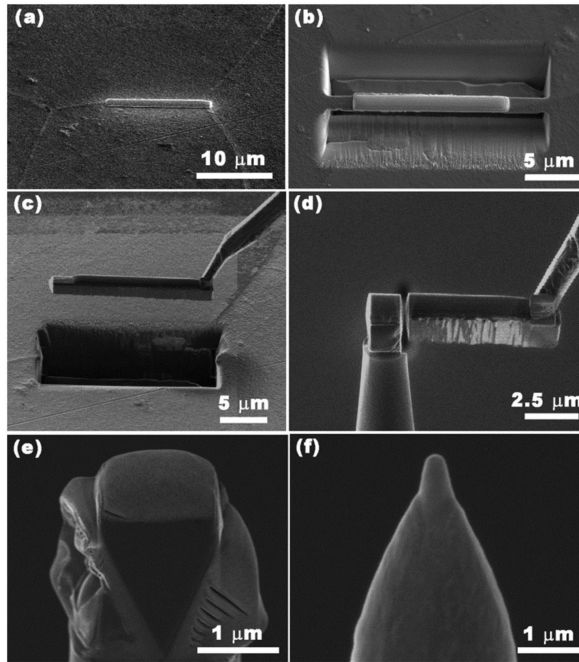


Figure 2.11: Site specific sample preparation for APT measurement using FIB [89].

D Application of APT to thermally grown oxide scales

APT is the only method that can routinely analyze and localize individual atoms in a material with nearly atomic resolution and with an equal sensitivity for all the elements. Back in time, atom probe technique had limited applications, only to conductive materials. With the advancement in the laser development, a pulsed-laser made possible to characterize non-conducting materials such as oxides. It has been extensively used for bulk oxides [90–92] and thermally grown oxide scales formed on alloy surfaces [93–96]. The elemental distributions derived from APT, especially at grain boundaries and interfaces, enabled to uncover the diffusion pathways and identify the role of minor alloying elements in the oxidation process.

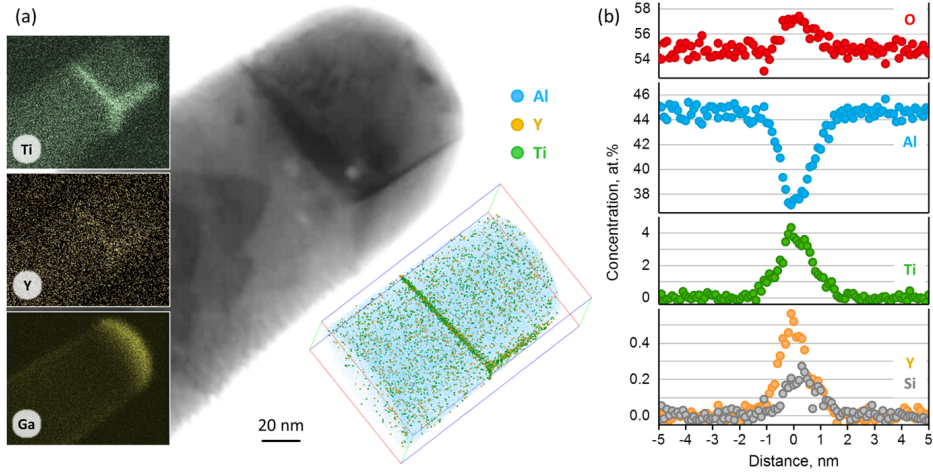


Figure 2.12: Correlative APT-TEM approach for a thermally grown alumina scale (a) bright-field STEM image of an APT specimen and corresponding EDS mapping for Ti, Y and Ga including APT atom maps and (b) elemental concentration profiles from the grain boundary [94].

A simple yet powerful example of APT characterization on thermally grown Al_2O_3 is shown in Figure 2.12 with clear segregation of minor solutes like Ti, Y, Si and O. Due to its superior benefits over other techniques, in the present work, APT was extensively employed to understand the segregation of alloy impurities and link it to oxide growth mechanism.

2.10 Motivation

As stated earlier, the intermittent nature of renewable energy generation by wind and solar limits its widespread adoption by virtue of lack of energy storage infrastructure. The introduction of SOCs has the opportunity of bridging the gap between electricity generation from intermittent renewable energy sources and its utilization with only minor adaptations in the way the energy is used today. This technological solution is ultimately a material challenge, as the design and optimization is targeted towards long-lasting, cost-effective and more efficient SOCs and hence, the components of SOCs need to be thoroughly researched and evaluated. In particular, research on interconnect materials is very important due to the various stringent requirements placed on it, especially those arising from the high temperature oxidation.

Metallic interconnect materials, mainly high-Cr ferritic steels, at high temperatures tend to oxidize quite rapidly, resulting in deterioration of electrical and mechanical properties. This

work is motivated by the fact that the present understanding of the oxidation behavior of these ferritic steels under actual operating conditions of SOCs remains insufficient. Therefore, such an investigation is very essential for efficient composition tailoring for further improvement of the steel properties, particularly its high temperature oxidation resistance, with a special focus on

- (i) the role of different SOC-relevant atmospheres and
- (ii) the effect of alloy composition including the minor constituents.

As these steels are exposed to air and fuel on either side, study of the oxidation behavior in such a wide range of corrosive environments is of significant importance. The model gas compositions: Ar – O₂ characterizing atmosphere on the air side and Ar – H₂ – H₂O, Ar – CO – CO₂ representing typical atmospheres on the fuel side of SOC devices were chosen for this work. In order to investigate the effect of alloying elements, a commercially available Crofer 22 H with variations in Nb, Ti and Si content and in total four steel varieties are produced. Oxidation tests are conducted at 800 °C, as the SOCs show the best efficiency at this temperature.

A key aspect in elucidating the oxidation mechanisms is to characterize thermally grown oxide scales down to near-atomic scale, which requires high resolution methods such as TEM and APT. Such investigation would lay the foundation for quantitative and qualitative interpretation of mass transport and diffusion pathways, in particular, to identify the oxide growth mechanisms that limit performance of SOC interconnects, and would aid in better design of interconnect materials for high temperature performance.

3 Experimental Methods

This chapter focuses on the type of materials and methods used for performing oxidation studies in different gas compositions pertinent to fuel cell operating conditions. A detailed methodology of the oxidation testing and characterization approaches is discussed.

3.1 Alloys investigated

A commercial steel Crofer 22 H was selected as the base alloy, and its modifications were produced by varying the concentrations of Nb, Ti and Si to study the effect of these elements. The steels were manufactured by VDM Metals by vacuum melting. An ingot of approximately 10 kg was cast and subsequently hot rolled down to sheets of 2 mm thickness.

Table 3.1: Chemical composition of the investigated alloys as determined by ICP-OES (in at. %).[†]
Alloys designations contain N for Niobium, T for Titanium and S for Silicon additions.

	Fe	Cr	Mn	Al	Si	Nb	Ti	La	W	C	N
Alloy-NTS (Crofer 22 H)	73.31	24.64	0.44	0.04	0.42	0.31	0.08	0.03	0.3	0.03	0.06
Alloy-NT (KCL)	74.8	23.58	0.52	0.02	0.04	0.66	0.17	0.06	–	0.05	0.07
Alloy-T (Crofer 22 APU)	75.36	24	0.41	0.03	0.02	–	0.06	0.04	–	< 0.01	0.01
Alloy-N (KCD)	74.48	24.22	0.47	0.02	0.04	0.63	–	–	–	0.02	0.08

[†]Alloys additionally contain B and C in concentrations < 50 atomic ppm.

The actual chemical compositions of the steels were analyzed by inductively coupled plasma optical emission spectroscopy (ICP–OES) and are given in Table 3.1. For convenience in reading, the alloys were designated following their minor elements content, where N, T and S stand for additions of niobium, titanium and silicon, respectively. The alloy names given in the parentheses refer to their designations in commercial/lab use.

3.2 Oxidation Testing

Samples of dimensions 20 x 10 x 2 mm for oxidation testing were machined from the hot rolled sheet by laser cutting. All machined samples were ground down to a 1200 grit surface finish with SiC abrasive papers. Prior to high temperature exposure, the specimens were ultrasonically cleaned with ethanol.

The high temperature oxidation experiments were performed at 800 °C (the typical operating temperature of SOCs) on all studied alloys in three different gas compositions i.e. Ar – 20 %O₂, Ar – 4 %H₂ – 4 %H₂O and Ar – 1 %CO – 1 %CO₂, which are model gases for SOEC/SOFC devices. Weight gain was monitored using a Setaram TG 92 microbalance. Specimens were heated to the test temperature at a rate of 90 K/min in the test gas, kept at 800 °C for 72 h, and subsequently furnace cooled at approximately 10 K/min.

3.3 Materials Characterization

Materials characterization is a key step to understand the materials' behavior under different oxidizing conditions. Basic information about phase composition by XRD and Raman spectroscopy, elemental depth profiling using GD–OES, oxide microstructure from SEM/TEM and quantitative elemental composition at nanoscale by APT are discussed in this section.

3.3.1 Phase Analysis

A X-ray Diffraction (XRD)

In order to identify the phases formed during high temperature oxidation (in different gas compositions and on various alloys), XRD technique was used. Phase analysis was done in two different modes; (i) parafocusing Bragg–Brentano geometry for the entire oxide scale using the following parameters: time per step of 1 sec, step size 0.026, divergence 0.4° and Cu tube operating 40 kV/40 mA (K_{α} radiation) and (ii) grazing incidence–XRD (GI–XRD) for surface oxide layers was performed using the parameters: time per step 2 sec, step size 0.025 and Cu tube of 40 kV/40 mA.

B Raman Spectroscopy

Laser Raman Spectroscopy by Dilor HR 800 equipped with a HeNe laser with the wavelength of 632.8 nm was used for surface phase analysis on all the samples exposed under different conditions.

3.3.2 Compositional Depth Profiling

There are different techniques available to get the compositional depth profile information, some of which are glow discharge optical emission spectroscopy (GD-OES), secondary ion mass spectrometer (SIMS) and X-ray photo-electron spectroscopy (XPS). Among these techniques, GD-OES is superior for the present work with its primary strengths being large analysis depth (tens of micrometers) and quantitative information on elemental concentrations. Therefore, GD-OES was selected to chemically characterize the oxide scales via depth profiling.

HORIBA Jobin-Yvon GD analyzer equipped with a 4 mm glow discharge source was used for this research work. The sputtering conditions (in Ar) were: pressure 700 Pa and power 30 W. In the GD-OES depth profiling, the sputter crater had a diameter of 3 mm and a procedure similar to that described in [97] was used for quantification.

3.3.3 Electron Microscopy

A Scanning Electron Microscopy (SEM)

The surface and cross-sectional microstructure of the oxidized samples were examined by SEM using a Zeiss Supra 50VP instrument. For cross-sectional SEM investigation, the specimens were mounted in an epoxy resin. Prior to mounting, the specimens were coated with an approximately 100 nm thick gold layer to create electrical conductive surface, and subsequently electroplated with nickel using NiSO₄ solution. The nickel layer mechanically supports the oxide scale during further metallographic preparation, and additionally improves the contrast between the oxide scale and the mounting material during optical and electron microscopy observations.

B Transmission Electron Microscopy (TEM)

Cross-sectional samples for TEM investigations were prepared using a Zeiss Auriga cross beam focused ion beam (FIB) with a Ga ion source using a lift-out method (Carl Zeiss Microscopy GmbH, Germany). TEM imaging was carried out in the scanning mode (STEM) using

a Zeiss Libra 200 transmission electron microscope (Carl Zeiss Microscopy GmbH, Germany) with accelerating voltage of 200 kV. The TEM images were acquired in a bright field, a dark field and a high angle annular dark field (HAADF) modes with the use of corresponding detectors. Elemental analysis of the oxide scale was performed by energy dispersive X-ray spectroscopy (EDS) using a X-Max 80 detector (Oxford Instruments, UK).

3.3.4 Atom Probe Tomography (APT)

For APT investigation of thermally grown oxide scales and metal–oxide interfaces, specimens were prepared from the cross-sectional SEM samples by a conventional lift-out method [84] similar to that shown in Figure 2.11 using a Thermo Fisher Scientific FEI Helios Nanolab 650i dual beam FIB. APT specimens from the chromia scale were prepared perpendicular to the growth direction (parallel to the oxide scale) to maximize the number of grain boundaries in APT datasets, since chromia grains usually appeared textured in the growth direction. APT specimens containing the metal–oxide interface were prepared perpendicular (to maximize the analyzed interface area) as well as parallel (to minimize the influence of local magnification effect at the interface) to the growth direction.

APT analysis was performed using a LEAP4000X HR instrument (Ametek Inc.) operating in laser mode with laser pulse frequencies of 200–250 kHz, laser pulse energies of 30–50 pJ and detection rate of 0.005 ions per pulse. The base specimen temperature was maintained at 50 K for all measurements. APT data reconstruction and analysis was carried out using the Integrated Visualization and Analysis Software (IVAS™) package 3.6.14 (Ametek Inc.).

APT reconstructions for chromia scale measurements were built based on the voltage-guided algorithm for radius evolution, while constant shank-angle algorithm was used for reconstruction of metal–oxide region measurements. For performing a correct reconstruction, i.e. matching the real specimen geometry, a set of reconstruction parameters must be determined and provided (initial specimen radius, specimen shank angle for shank-guided mode, image compression factor, atomic volumes and detection efficiency). The initial specimen radius for the start of the reconstruction is usually hard to measure due to irregular shape of the apex after FIB preparation. However, based on the assumption that the evaporation field during the measurement is constant, the field value can be derived from the final radius of a specimen determined in SEM after terminating the APT measurement based on the following equation,

$$F = \frac{V}{kR} \quad (3.1)$$

where F is the magnitude of electric field, V is the final applied voltage, R is the specimen radius and k is a field constant (assumed equal to 3.3 for the LEAP tool). The initial radius for the reconstruction can be later determined using the same equation, provided the starting voltage for the reconstruction is set.

The correct atomic volumes were determined based on the crystallographic data for the phases present in the APT datasets. The atomic volumes of metal species were set equal to $0.012 \text{ nm}^3/\text{at}$ matching the average atomic volume of the iron-based BCC alloy. The atomic volume of oxygen was set to $0.008 \text{ nm}^3/\text{at}$ to ensure the correct average atomic volume in the chromia phase. This oxygen volume also provides a quite correct average ionic volume for other detected oxide phases, e.g. spinel, ensuring the spatially correct reconstruction.

The detection efficiency was slightly reduced to 0.32 as compared to nominal 0.36 for the LEAP 4000X HR tool after analyzing the spectrum background to account for the volumes of out-of-pulse evaporated ions (a more detailed explanation can be found elsewhere [94]). The image compression factor was finally adjusted to obtain the reconstruction length matching the true length of the evaporated volume, as assessed by comparing the pre- and post-analysis SEM images of the specimen. This approach enables building a spatially correct reconstruction of the specimen, which is critical for quantification of GB segregation [94].

4

Effect of gas composition on high temperature oxidation

4.1 Introduction

This chapter deals with the oxidation behavior of a Crofer ferritic steel exposed to different gas compositions. In real SOFC operating conditions, the cathode side of the interconnect is exposed to air and the anode side is exposed to fuel. To model the conditions of SOFC operation, the oxidation experiments were performed in Ar – 20 %O₂ atmosphere representing the air side and Ar – 4 %H₂ – 4 %H₂O, Ar – 1 %CO – 1 %CO₂ atmospheres representing the fuel side. The oxygen partial pressures of these gases were determined from FACTSAGE software and the values are shown in the Table 4.1. Based on the oxygen partial pressures, they are broadly divided into two types: high p_{O_2} and low p_{O_2} gases. Commercially available steel, Crofer 22 H with modified chemical composition was used to study the oxidation behaviour in these gas compositions.

Table 4.1: The partial pressures of oxygen calculated using FACTSAGE for different gas compositions used in the current research work.

Gas Composition	p_{O_2} (atm)
Ar – 20 %O ₂ (high p_{O_2})	0.2
Ar – 4 %H ₂ – 4 %H ₂ O (low p_{O_2})	4.3×10^{-19}
Ar – 1 %CO – 1 %CO ₂ (low p_{O_2})	3.6×10^{-19}

4.2 Thermogravimetric analysis

One of the common methods to study a high temperature oxidation process is by monitoring the weight change before and after the oxidation experiments. Figure 4.1 shows the thermogravimetric (TG) data acquired during isothermal oxidation representing the continuous weight gain process as a function of exposure time in three different gas compositions at 800 °C for 72 hours of exposure.

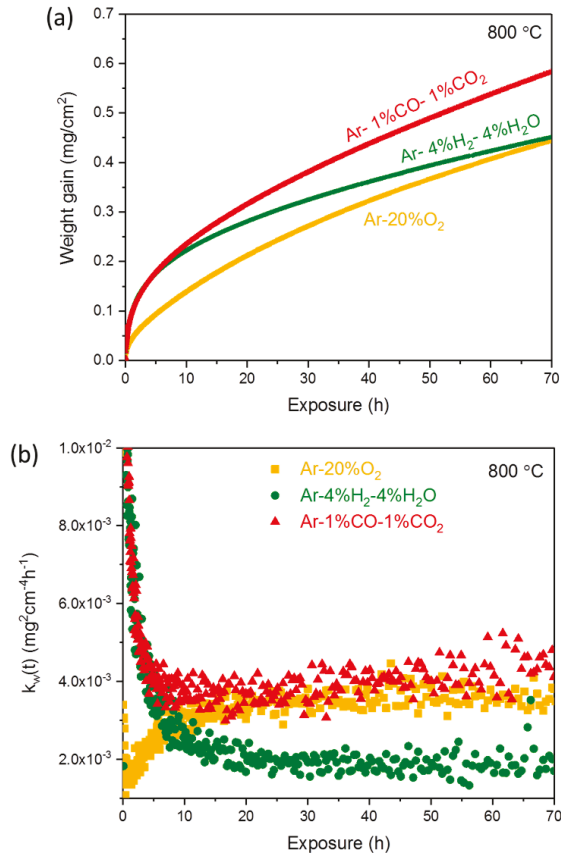


Figure 4.1: Thermogravimetric test results acquired during isothermal oxidation of Alloy-NT at 800 °C in different gas compositions for 72 hours of exposure: (a) mass change as a function of the exposure time and (b) instantaneous *apparent* parabolic rate constant (k_p) as a function of the exposure time.

Too short exposure experiments give information about the transient oxidation, commonly called as early stage of oxidation, which depends not only on the chemistry of gases or alloy but also on the sample preparation procedure leading to varied surface roughness. On the other hand, too long exposure experiments may lead to spallation due to accumulation of growth stresses. Therefore, an optimum exposure time is needed to grow the oxide scale which fully covers the alloy surface. From several iterations based on the earlier studies similar to this type of steel, it was found that 72 hours of exposure gives the required degree and uniformity of coverage of the oxide on the alloy surface.

It can be seen from [Figure 4.1a](#) that the weight gain for Ar – 20 %O₂ sample (high p_{O_2} gas) is much lower compared to Ar – 4 %H₂ – 4 %H₂O (low p_{O_2} dry gas) and Ar – 1 %CO – 1 %CO₂ gases (low p_{O_2} dry gas). However, after 72 hours, the weight gain for Ar – 20 %O₂ and Ar – 4 %H₂ – 4 %H₂O are almost equivalent, whereas the sample exposed to Ar – 1 %CO – 1 %CO₂ atmosphere shows significantly higher weight gain.

A plot of instantaneous *apparent* parabolic rate constant (k_w) as a function of exposure time is presented in [Figure 4.1b](#) and it displays lower rate constant value for the sample exposed in Ar – 20 %O₂ during the initial hours (< 10 hours) period. As the time proceeds, k_w increases for Ar – 20 %O₂ (high p_{O_2}) and decreases for the sample exposed in low p_{O_2} gases. After 72 hours, the overall rate constants for the samples exposed in Ar – 20 %O₂ and Ar – 1 %CO – 1 %CO₂ is approximately similar, which is higher compared to Ar – 4 %H₂ – 4 %H₂O. This clearly indicates that both Ar – O₂ (high p_{O_2}) and Ar – 1 %CO – 1 %CO₂ (low p_{O_2}) atmospheres exhibit faster oxidation rate, implying that the p_{O_2} itself is not a decisive factor here.

For all gas compositions, an approximate parabolic time dependence of the oxide thickness is observed, except for initial oxidation stages, whereas the rate constant remains stable over time. The classical oxidation theory indicates that the transport processes in the oxide scale are rate determining in the given case. Since the mass transport through an oxide scale is always strongly dependent on its microstructure, characterization of the microstructure can give a clue to understanding the oxidation mechanisms, in particular, the role of the atmosphere and its components.

4.3 Phase analysis

Earlier studies revealed the possibility of simultaneous presence of several oxide phases in the scale formed on Crofer alloys. For this reason, the phase compositions of the oxide scales

were characterized by XRD and Raman spectroscopy. Figure 4.2 shows the XRD patterns of the Alloy–NT exposed in the three different gas compositions. The predominant oxide phases observed during high temperature oxidation are MnCr_2O_4 spinel, Cr_2O_3 and a rutile–type $\text{Nb}_{0.94}\text{O}_2$. The substrate (alloy) peaks are also identified after 72 hours of exposure at 800 °C. There are no significant differences between the XRD patterns for the samples exposed in these gas compositions.

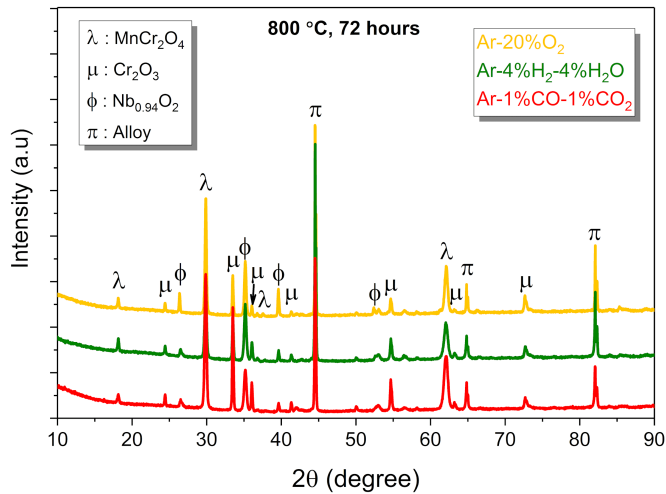


Figure 4.2: Room temperature XRD patterns acquired after isothermal oxidation of Alloy–NT exposed to different gas compositions at 800 °C for 72 hours.

Raman spectra for standard chromia, normal spinel and inverse spinel powder samples were obtained and then compared them with the spectra obtained from the thermally grown oxide scales formed on the surface of Alloy–NT in different gas compositions.

As Raman spectroscopy is a surface technique (the analysis depth is about 2 μm), information from the outermost layer shows higher intensity i.e., spinel formation on the surface is a direct observation from these results. It can be concluded from the Raman spectroscopy measurements (see Figure 4.3) that only normal spinel structure (λ) is present in low $p\text{O}_2$ gases (Ar– H_2 – H_2O and Ar– CO – CO_2) whereas a mixture of normal and inverse spinel structures (λ and η) are detected in high $p\text{O}_2$ (Ar– O_2) atmosphere.

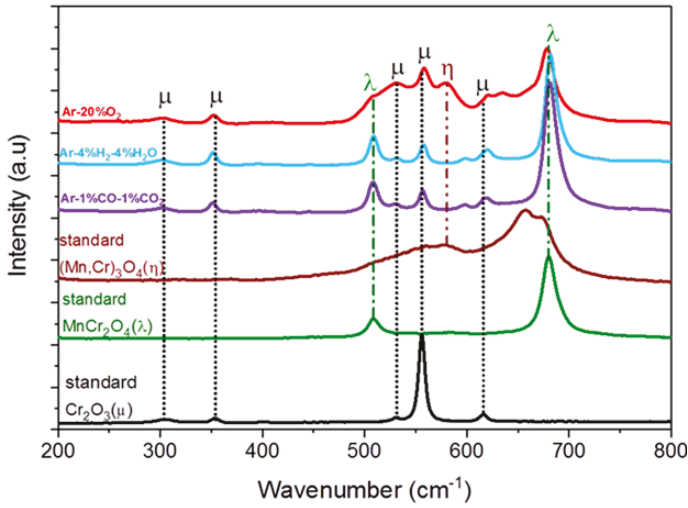


Figure 4.3: Raman spectra acquired after isothermal oxidation of Alloy-NT in different gas compositions at 800 °C for 72 hours.

4.4 Elemental Depth profiling

Different elements present in the alloy tend to oxidize at different oxygen partial pressures, which means multilayer oxide scale formation is usually possible for complex alloy systems. Therefore, depth profiling (concentration variation of an element from the surface to the bulk) of different species can reveal information on the formation of multilayered structure. Also from the previous results, the relative position of a particular phase in the entire oxide scale is not completely understood. To address this, the glow discharge-optical emission spectroscopy (GD-OES) was used. Figure 4.4 shows the GD-OES depth profiling for various elements present in the alloy after isothermal oxidation at 800 °C for 72 hours in Ar-20%O₂.

These profiles clearly show that the surface oxide is rich in Mn and Cr, indicating that the outermost oxide layer is spinel followed by chromia. This is in good agreement with XRD (Figure 4.2) and Raman (Figure 4.3) results. Nb and Ti peaks are evident at the oxide-alloy interface, indicating a new oxide phase formation at the interface. This is evident from XRD (Figure 4.2) as rutile-type NbO₂ phase. However, GD-OES profile shows that the oxide represents rather (Nb,Ti)O₂ stoichiometry. It should be noted here that the Ti peak might also contribute to internal oxidation zone formed in the alloy at the vicinity of oxide-alloy interface as such zones have been observed earlier [30]. In addition to the oxide formed at oxide-alloy

interface (or metal–oxide interface), Mn segregation is evident at the chromia/(Nb, Ti)O₂ oxide interface. From the GD–OES results it can also be concluded that the elements such as Fe, La and Si don't play an active role in the oxide formation as they are severely depleted in the oxide scale compared to their bulk concentrations. However, Al slightly segregates either at the oxide–alloy interface or in the internal oxidation zone (IOZ).

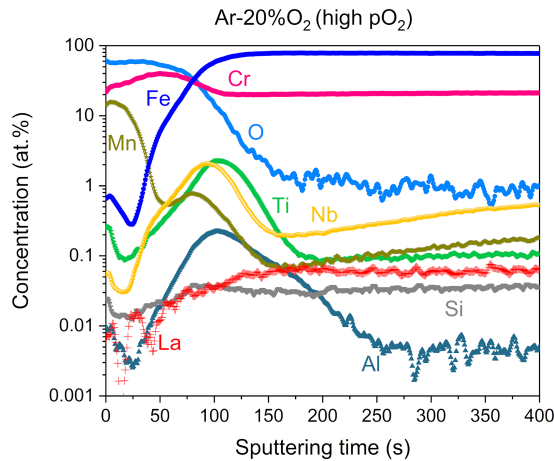


Figure 4.4: GD–OES depth profiling of various elements for the Alloy–NT exposed in Ar – 20 %O₂ at 800 °C for 72 hours of exposure.

Figure 4.5 shows the GD–OES depth profiling for various elements present in the same alloy (Alloy–NT) after isothermal oxidation at 800 °C for 72 hours of exposure in Ar – 4 %H₂ – 4 %H₂O. Almost similar depth profile was observed when compared to Ar – 20 %O₂ (Figure 4.4) except that the Nb/Ti ratio at oxide–alloy interface is significantly higher in the case of Ar – 4 %H₂ – 4 %H₂O. This is a clear indication that the amount of Nb, Ti–rich oxide is more in Ar – H₂ – H₂O.

Figure 4.6 shows the GD–OES depth profiling for various elements present in the Alloy–NT after isothermal oxidation at 800 °C for 72 hours of exposure in Ar – 1 %CO – 1 %CO₂. The elemental depth profiles for all elements in both the low p_{O_2} gases are almost identical. Mn concentration at the surface is relatively lower in the case of low p_{O_2} gases (Ar – 4 %H₂ – 4 %H₂O and Ar – 1 %CO – 1 %CO₂) compared to high p_{O_2} (Ar – 20 %O₂). This may be due to the higher solubility of Mn in the spinel formed in case of high p_{O_2} [98]. It was also found that in high– p_{O_2} atmosphere, Mn can replace a substantial amount of Cr in the Cr/Mn–outer spinel [99].

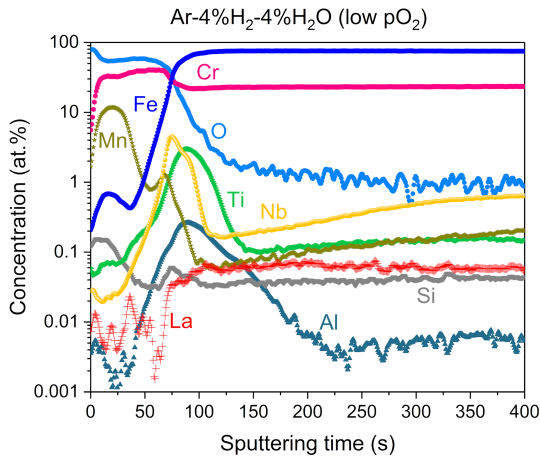


Figure 4.5: GD-OES depth profiling of various elements for the Alloy-NT exposed in Ar-4%H₂-4%H₂O at 800 °C for 72 hours.

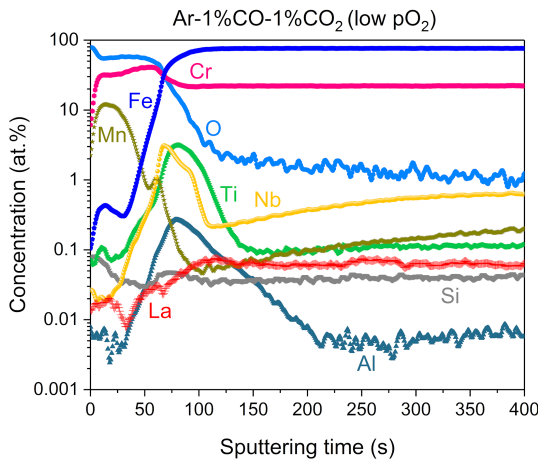


Figure 4.6: GD-OES depth profiling of various elements for the Alloy-NT exposed in Ar-1%CO-1%CO₂ at 800 °C for 72 hours.

Surprisingly, carbon is not evident either in the oxide scale or in the alloy. This indicates that there is no evidence of carburization during high temperature oxidation in Ar-CO-CO₂. Carbon penetration through the oxide scale is indeed a prominent phenomenon typically observed in carbon rich gases [54], but it was not observed in the present study.

However, the information from GD-OES profiles is not localized, both in terms of possible simultaneous sputtering of different layers in different regions of the sample surface and in terms of elemental distribution in the microstructure (in solid solution, at GBs or as minor inclusions of other phases besides spinel and chromia). This requires high resolution characterization methods, which are discussed in the following sections.

4.5 Electron microscopy

4.5.1 Scanning Electron Microscopy (SEM)

SEM was used to examine the surface morphology as well as cross-section of the oxide scale after oxidation in different gas compositions. Figure 4.7 shows the low magnification (a, b and c) and high magnification (d, e and f) SEM images of sample exposed to Ar-O₂ (a, d), Ar-H₂-H₂O (b, e) and Ar-CO-CO₂ (c, f).

Oxide scales fully cover the alloy surface in all the gas compositions. It can be seen that the sample exposed to Ar-O₂ shows globular oxide morphology whereas the samples exposed to low pO_2 gases show plate and whisker-like morphology, a typical morphology for this material in low pO_2 gases [54]. Therefore, the oxide formed in high pO_2 is relatively more denser than the oxides formed in low pO_2 gases.

The cross-sectional SEM images are shown in Figure 4.8. The cross-sectional micrographs for all the gas compositions show Laves phase in the base alloy microstructure. All the samples showed duplex oxide scales consisting of an outer spinel and an inner chromia. At high pO_2 , the spinel-chromia interface is quite compact and adherent whereas this interface in low pO_2 gases shows numerous pores (significantly in Ar-CO-CO₂) indicating that the adherence between the layers may be poor. Internal oxidation is observed in all the samples. Additionally, the internal oxide precipitates are more pronounced in the low pO_2 gases in contrast to the high pO_2 gas.

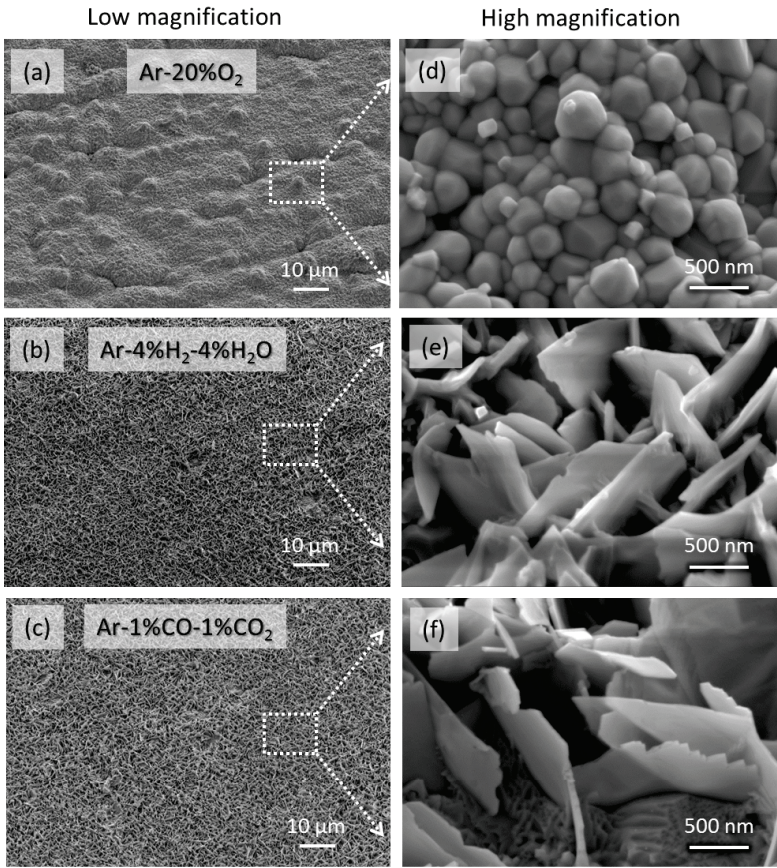


Figure 4.7: Surface morphologies of the Alloy-NT exposed at 800 °C for 72 hours in (a, d) Ar-20%O₂, (b, e) Ar-4%H₂-4%H₂O and (c, f) Ar-1%CO-1%CO₂. The figure also shows globular type oxide in case of Ar-20%O₂ (high p_{O_2}) and plate-like morphology in case of Ar-4%H₂-4%H₂O and Ar-1%CO-1%CO₂ (low p_{O_2} gases).

Earlier studies [100, 101] have shown that chromia formation takes place first, followed by Mn diffusion through chromia scale resulting in outer spinel (MnCr₂O₄) formation in the later stages of oxidation. Therefore, the elemental diffusion through chromia (including that of Mn outward diffusion) is the rate-controlling process for the overall kinetics. The methods presented above reveal the overall structure and composition of the oxide layer. However, their spatial resolution and/or chemical sensitivity are not sufficient to look into the microstructure at the level that enables to understand the diffusion processes through the oxide scale and

across the metal–oxide interfaces. High-resolution techniques need to be employed for that purpose.

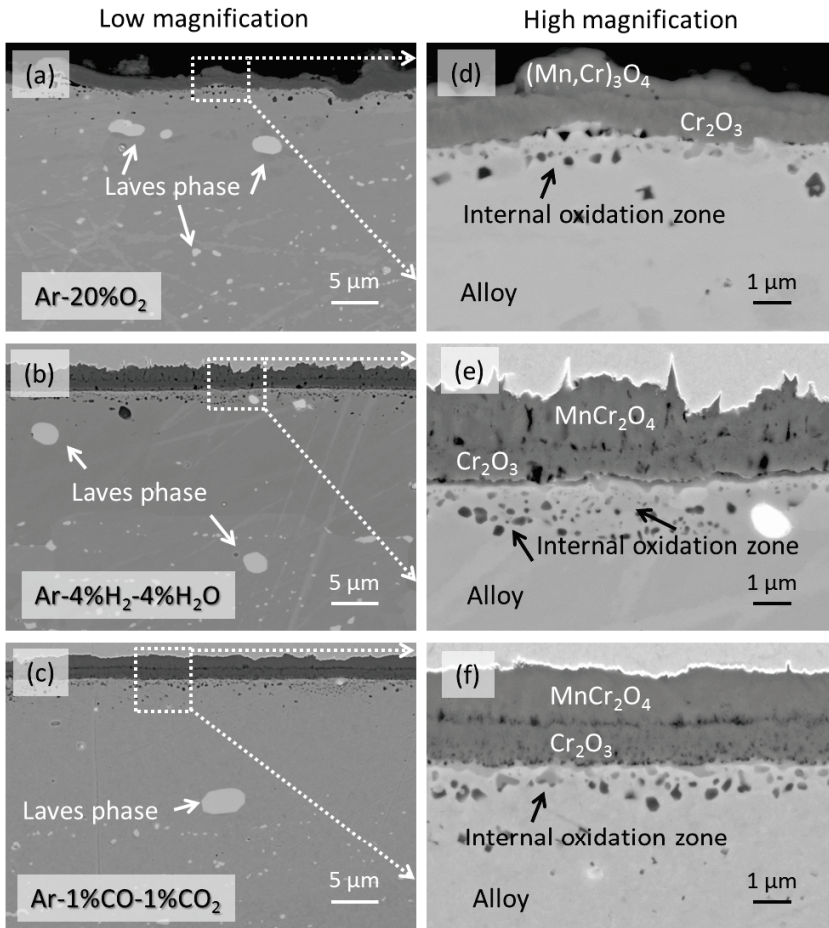


Figure 4.8: Cross sectional SEM images of the Alloy–NT exposed at 800 °C for 72 hours. (a, d) Ar–20%O₂, (b, e) Ar–4%H₂–4%H₂O and (c, f) Ar–1%CO–1%CO₂.

4.5.2 Transmission Electron Microscopy (TEM)

TEM analysis was performed in the scanning mode (STEM) to further investigate the oxide scales of the Alloy–NT with respect to the scale thickness, porosity and grain structure. [Figure 4.9](#) shows that the oxide layers formed in different gas compositions have different thicknesses of individual subscales.

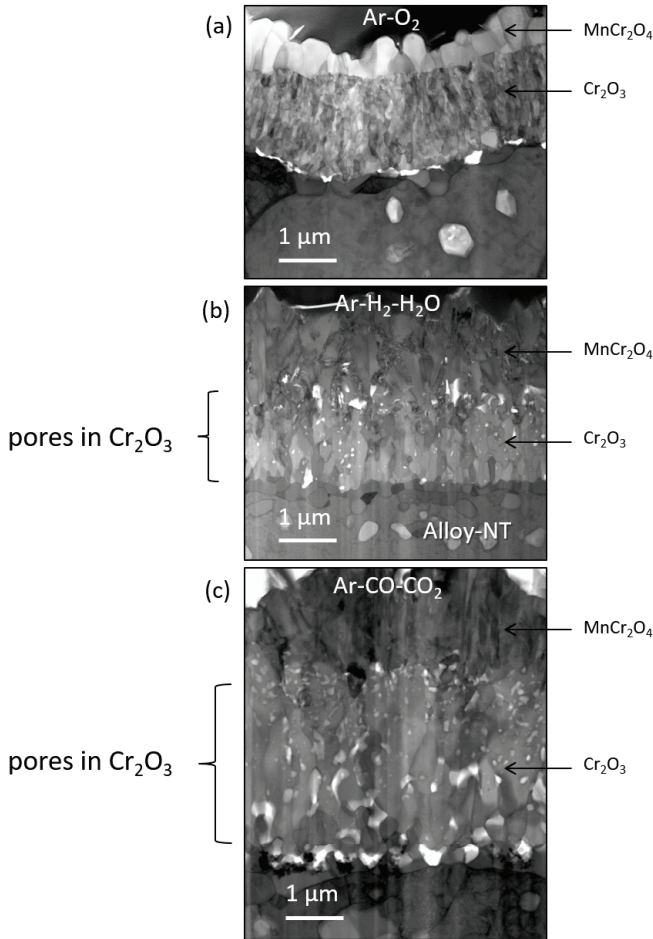


Figure 4.9: Bright-field STEM images of oxide layers formed on the surface of Alloy-NT at 800 °C after 72 hours of exposure in (a) Ar-20%O₂, (b) Ar-4%H₂-4%H₂O and (c) Ar-1%CO-1%CO₂.

In high pO_2 gas, the spinel is thinner compared to chromia, whereas in low pO_2 gases the reverse effect is observed. The thinner spinel layer in the high pO_2 gas appears probably due to slower Mn diffusion to the gas-scale interface (or to the surface of the oxide). On the other hand, chromia is thicker in Ar-CO-CO₂ compared to other gases [Figure 4.9](#). Interestingly, a continuous Nb(Ti,Cr)O₂ oxide layer of 0.35 μm thickness is observed at the metal-oxide interface in the low pO_2 gases and this layer is discontinuous at high pO_2 .

Table 4.2: Thickness (in μm) of different oxide scales formed after 72 hours of oxidation at $800\text{ }^\circ\text{C}$ in different gas compositions for the Alloy-NT.

Oxide scales	Ar-20%O ₂	Ar-4%H ₂ -4%H ₂ O	Ar-1%CO-1%CO ₂
Spinel (outer)	0.76	1.76	1.57
Chromia (inner)	1.33	0.97	1.7
Nb(Ti, Cr)O ₂	Discontinuous	0.35	0.35
Total	2.4	3.08	3.62

Table 4.2 displays the thicknesses of the oxide layers formed in different gas compositions. The overall thickness of the oxide scale changes in decreasing order as follows: Ar-CO-CO₂ > Ar-H₂-H₂O > Ar-O₂. This is in agreement with the weight gain plot from the thermogravimetric test results (Figure 4.1).

A major and important observable difference in the oxide scales formed in three gas compositions is their porosity. The pore density in the chromia scale and at the metal-oxide interface is quite high in Ar-CO-CO₂. Probably this is the reason for faster oxidation in this atmosphere as the diffusion through the scale can partially proceed at the walls of the pores, which must occur faster compared to solid-state diffusion solely. This process can be further exacerbated if the pores are partially interconnected, so that the residual diffusion path through the solid will be substantially shortened. However, this cannot be directly proved due to limitations of the used analytical techniques. As seen in Figure 4.9, the metal-oxide interfacial pores are significantly larger in Ar-CO-CO₂ and Ar-O₂ but these pores remain smaller in Ar-H₂-H₂O, indicating that there is no direct dependence on the $p\text{O}_2$ level. Spinel-chromia interfacial pores are quite pronounced in Ar-H₂-H₂O in contrast to the high $p\text{O}_2$ atmosphere. All these types of pores can make the entire oxide scale less dense and can cause it to spall off easier due to thermal stresses.

Although a similar duplex scale structure (chromia-spinel) is observed for all gas compositions, the scales exhibit large differences also with respect to the grain sizes of the chromia scale, as shown in the Figure 4.10. Besides, at high $p\text{O}_2$ the chromia grains are nearly equiaxed, whereas at low $p\text{O}_2$ they are more elongated (columnar) in the direction of oxide growth, indicating slightly textured growth. As mentioned above, GBs substantially contribute to the overall diffusion through the oxide. The total diffusion flux through GBs must be proportional

both to the GB ionic conductivity and to the GB density. It was found that the sample with the densest GB network (chromia in Ar–O₂ as shown in Figure 4.10) shows nevertheless the lowest weight gain (Figure 4.1). Therefore, it can be concluded that the ionic conductivity appears to be a limiting step for the oxide growth. However, TEM capabilities are restricted with respect to unveiling the accurate GB chemistry, which can substantially influence their ionic conductivity, so APT has been employed for further investigations.

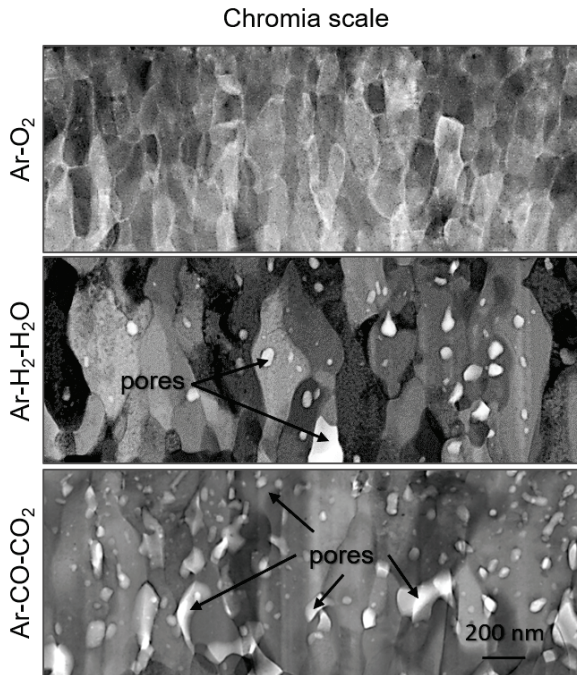


Figure 4.10: Bright-field STEM micrographs shown for chromia grain size comparison formed on Alloy-NT at 800 °C oxidized in three different gas compositions for 72 hours.

4.6 Atom probe tomography

To get insights into the chemistry of chromia scale including grains and grain boundaries as well as segregation of alloying elements at GBs, APT was employed.

4.6.1 Chromia scale in Ar–O₂

Figure 4.11 shows the results the APT analysis of chromia scale formed in Ar–O₂ after 72 hours at 800 °C.

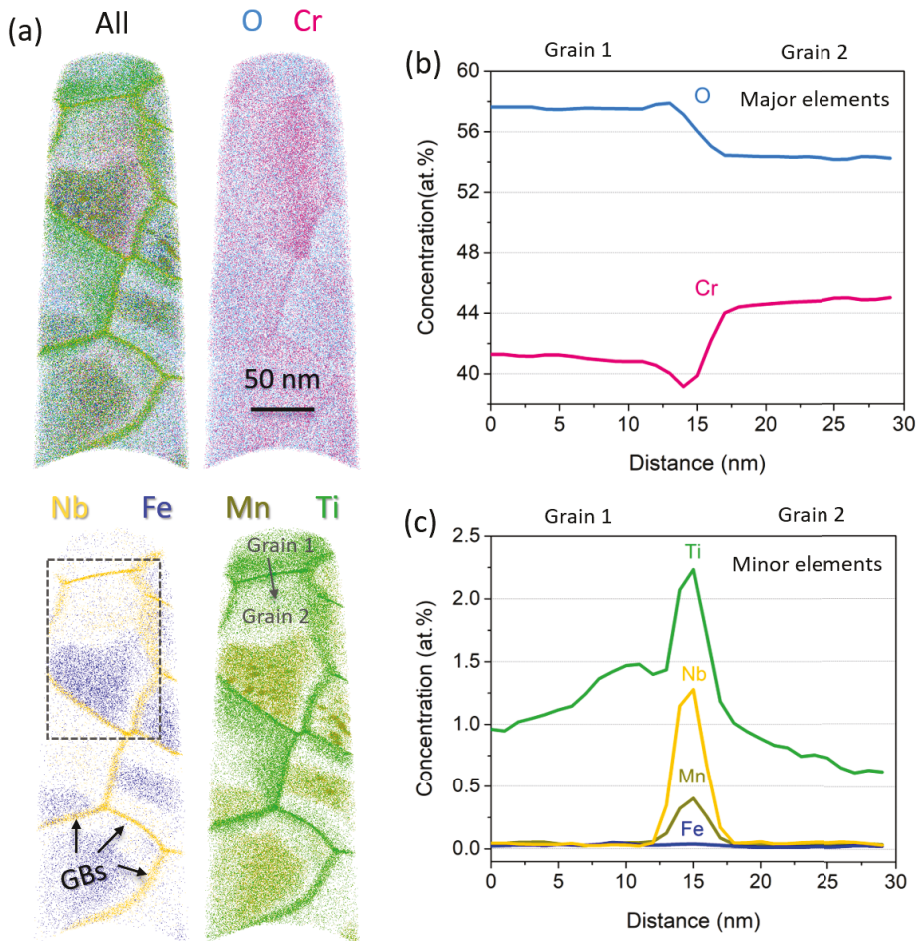


Figure 4.11: APT analysis of chromia scale formed on the Alloy-NT exposed to Ar – 20%O₂ at 800 °C for 72 hours. (a) Atom maps of chromia showing the elemental segregation to grain boundaries (Ti, Nb and Mn) and solubility in grains (Ti, Mn and Fe are not uniformly distributed), (b) and (c) are the elemental concentration profiles for major and minor elements, respectively, across a random grain boundary marked with an arrow in (a).

Atom maps (Figure 4.11a) clearly show the polycrystalline chromia with multiple grains and grain boundaries, which are distinguished by the segregation of alloying elements such as Ti, Nb, Al and Mn. Additionally, inhomogeneous distribution of Ti, Mn and Fe is also evident within the grains. It is interesting to observe the segregation patterns of Mn and Fe which share the same regions inside the chromia grains.

Table 4.3 shows the bulk composition of chromia scale formed in Ar–O₂. The amount of oxygen is slightly underestimated compared to its stoichiometric level (60 at. % O). However, the underestimation of oxygen concentration in oxide materials is an usual artifact in the APT measurement [102–104] due to dissociation of complex metal–oxygen ions under high electric field resulting in formation of undetectable oxygen neutrals, so the observed non-stoichiometry should be disregarded. The impurities present in chromia scale are Ti and Mn with concentrations of 0.66 at. % and 0.36 at. %, respectively, as well as Nb and Fe with 0.13 at. % each. The concentrations of bulk impurities are quite low, rendering their detection and particularly the elemental distribution by analytical TEM nearly impossible.

Table 4.3: APT bulk composition of chromia scales formed in different gas atmospheres relevant to SOFC/SOEC.

Gas composition	O	Cr	Mn	Si	Al	Ti	Nb	Fe
Ar–O ₂	56.43	42.24	0.36	0	0.03	0.66	0.13	0.13
Ar–H ₂ –H ₂ O	56.16	41.9	0.057	0.087	0.096	0.82	0.1	0
Ar–CO–CO ₂	56.12	43.13	0.031	0.049	0.011	0.54	0.054	0

Concentration profile across a random grain boundary (marked with an arrow in Figure 4.11a) is presented in the Figure 4.11b (for major elements) and Figure 4.11c (for minor elements). It shows the complex and perhaps non-stoichiometric nature of Cr₂O₃, where the chromium-to-oxygen ratio varies from one grain to another (unlike the absolute O concentration in oxides, the relative variations can be established by APT reliably). The minor alloy impurities such as Ti, Nb and Mn segregate to chromia GBs with peak concentration of 2.2 at. %, 1.2 at. %, < 0.5 at. % respectively. Interestingly, Nb showed almost no solubility in the chromia lattice (bulk) whereas Ti shows a substantial lattice solubility.

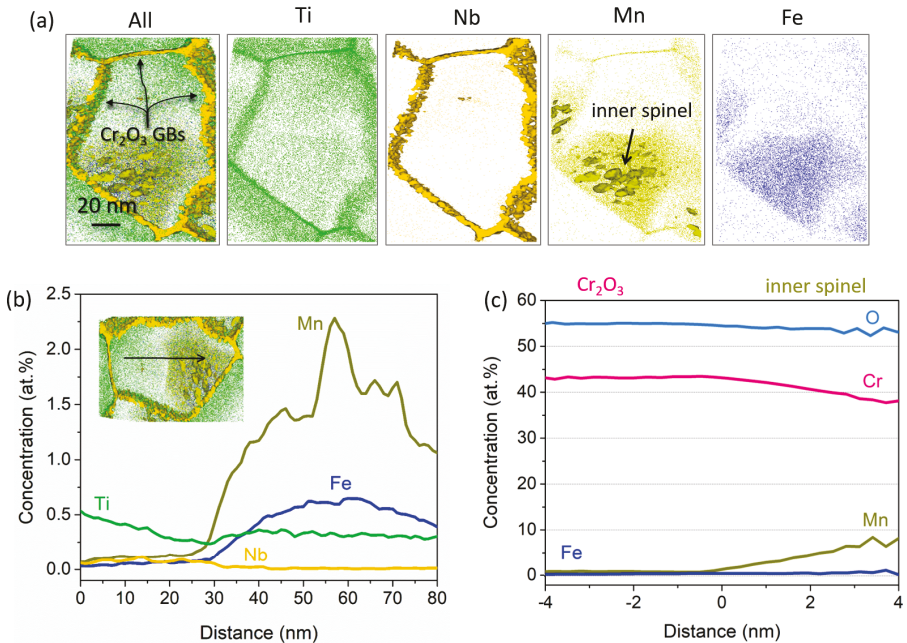


Figure 4.12: (a) Atom maps from APT for a grain interior decorated with Nb and Mn iso-surfaces. (b) Typical concentration profiles across a grain interior. (c) Proxigrams for the Mn-rich nano precipitates showing the substoichiometry of the inner spinel nuclei.

Earlier study showed that increase in pO_2 results in increased solubility of Mn in the chromia grains [99]. However, at nanoscale it is not homogeneous, as can be seen from Figure 4.12b. The Mn content in the chromia grain interior varies from 0 to 2.3 at. %. However, the proximogram shown in Figure 4.12c, showed Mn content in the local in-grain microvolumes reaching at least 7–8 at. %. Taking into account that about 14–15 at. % of Mn is required for MnCr_2O_4 to be formed, this clearly indicates that the Mn-rich tiny regions can be interpreted as possible inner spinel nuclei (based on their composition). The Mn content in these regions may increase with exposure time and would lead to complete stoichiometric spinel formation inside the chromia grains. To prove that these microvolumes are indeed the nuclei of another phase in chromia, structure-sensitive methods such as HR-TEM are needed.

4.6.2 Chromia scale in Ar–4% H_2 –4% H_2O

Figure 4.13 shows the APT analysis of chromia scale formed in Ar– H_2 – H_2O after 72 hours at 800 °C. Atom maps also show the fine-grained nature of chromia scale which is distin-

guished by the segregation of alloying elements such as Ti, Nb, Mn and Al at GBs. Si appears as an island-like segregation pattern randomly formed inside the chromia grains, at grain boundaries and triple junctions. Unlike the sample oxidized in the high pO_2 gas, Ti is the only element which shows notable solubility (approximately 0.5 at. %) in the chromia grains (Ti doped Cr_2O_3 lattice). However, the overall bulk composition for the chromia scale shows 0.8 at. % of Ti (see Table 4.3), which is due to substantially higher Ti concentration at GBs.

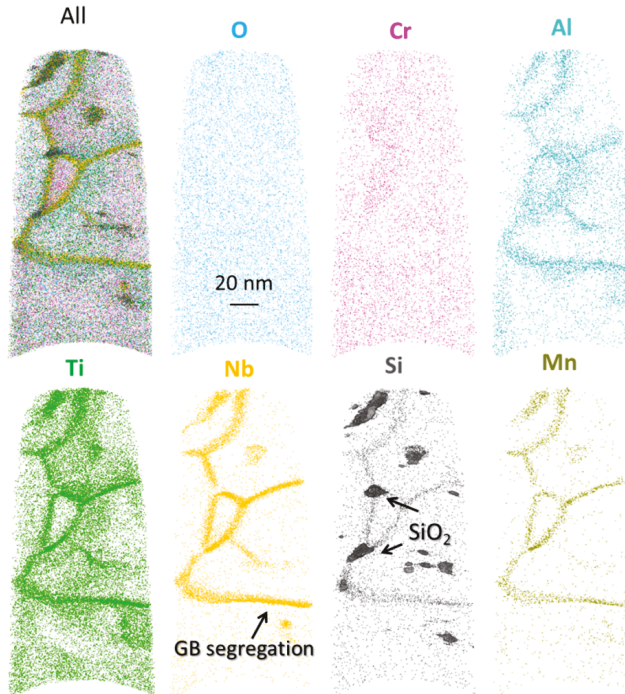


Figure 4.13: Atom maps from APT for the chromia formed on Alloy-NT after isothermal oxidation at 800 °C in Ar-H₂-H₂O for 72 h.

GB segregation was quantitatively analyzed by plotting the concentration profile across a random GB in the chromia (see Figure 4.14a). The elements which segregate at GBs don't show any notable solubility in the grains, except for Ti. The peak concentration at chromia GBs reach about 2.5 at. % for Ti, about 1.2 at. % for Nb and 0.25 at. % for Mn, which is similar to the values observed in high pO_2 atmosphere. Al segregation is slightly displaced from the GB plane, which might occur due to either cooling the sample to room temperature or by space charge distribution at GB plane by heavier cations like Nb, Ti and Mn. Figure 4.14b

shows the proximity histogram across the isosurface encompassing the Si-rich regions in the chromia scale. The Si-to-O ratio within these regions indicates stoichiometry close to SiO_2 , i.e. formation of silica particles. Interestingly, these silica particles were not observed in high $p\text{O}_2$ atmosphere (Figure 4.11 & Figure 4.12). This indicates that Si has relatively higher tendency to form SiO_2 at low $p\text{O}_2$ values.

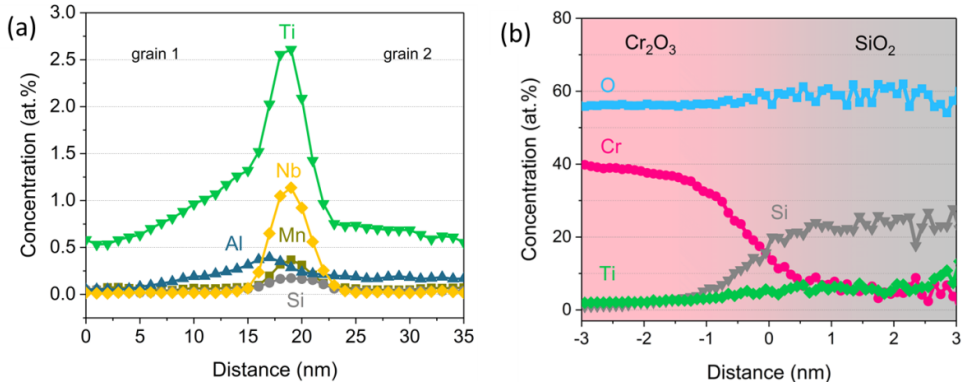


Figure 4.14: (a) Concentration profiles across a random grain boundary from Figure 4.13, and (b) Proxigrams across the interfaces encompassing Si-rich regions in the chromia scale.

4.6.3 Chromia scale in Ar – 1%CO – 1%CO₂

Figure 4.15 shows the results of the APT analysis of chromia scale formed in Ar – CO – CO₂ after 72 hours of exposure at 800 °C. The APT dataset shown below contains 3 grains and GBs including a triple junction (three GBs meeting at a line). Elements such as Ti, Nb, Mn and Al segregate at chromia GBs, whereas Si shows island-like segregation pattern, very similar to that in chromia scale formed in Ar – H₂ – H₂O.

Also, the segregation activities of impurities are quantitatively nearly identical to those in Ar – H₂ – H₂O, i.e. there is not much difference in nanoscale chemistry of the chromia scales formed in Ar – H₂ – H₂O and Ar – CO – CO₂. It is worth mentioning that carbon from the gas atmosphere has not been detected in any parts of the chromia by APT, so it does not directly influence the chromia scale formation. This is probably due to low carbon activity ($a_C = 0.01$ calculated from FACTSAGE) in the gas composition. In spite of the low Si concentration in the investigated steel (Alloy-NT), it was found in the chromia scale with an average concentration of approximately 0.04 at. % in Ar – CO – CO₂.

The key observation from APT with respect to different atmospheres is that the chemistry of chromia grain boundaries is nearly identical for all gas compositions, indicating a similar influence on the GB diffusion properties.

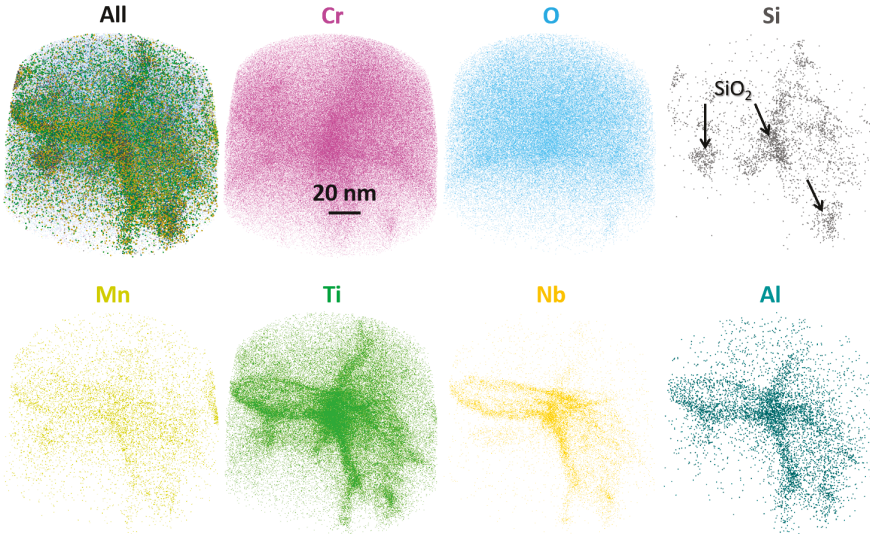


Figure 4.15: Atom maps from APT of chromia scale formed on Alloy-NT after isothermal oxidation at 800 °C in Ar-CO-CO₂ for 72 hours.

4.7 Oxidation Mechanisms

4.7.1 Nanoscale considerations for the oxide scale growth

It is known that for Cr₂O₃ at 800 °C, the cationic (outward) diffusion via GBs is much faster than the lattice/bulk diffusion [24]. Therefore, chromia GBs play a very important role in oxidation process. Segregation of elements such as Mn, Nb, and Ti to chromia grain boundaries alters its defect structure. From the theory of Wagner-Hauffe doping, it is known that doping of chromia with Mn²⁺ (this is inferred from the surface spinel stoichiometry, MnCr₂O₄) results in increased concentration of oxygen vacancies, whereas Nb⁴⁺/Nb⁵⁺/Ti⁴⁺ additions to chromia can result in increased concentrations of chromium vacancies, as shown in the following equations.





The above equations (Equation (4.1)–(4.4)) indicate that oxygen vacancies are generated in case of Mn addition, which are responsible for inward chromia growth mechanism, and chromium vacancies are generated in case of Nb and Ti addition, which are responsible for outward chromia growth mechanism. The schematic representation of mass transport via chromia grain boundaries is shown in Figure 4.16. Additionally, grain interior doping by Mn and Fe in high $p\text{O}_2$ should increase the oxygen vacancies in the oxide scale and thereby should make the oxidation process faster. However, the reverse effect was observed (high $p\text{O}_2$ sample showed lower weight gain from TG results). Inner spinel formation in high $p\text{O}_2$ contributes only partially to the weight gain. Kinetic trapping of Mn (in chromia grain interiors) may be indeed responsible for thinner spinel (less Mn reaches the surface), but it does not explain the overall weight gain. In case of Mn unavailability, Cr would just oxidize exclusively and form more chromia.

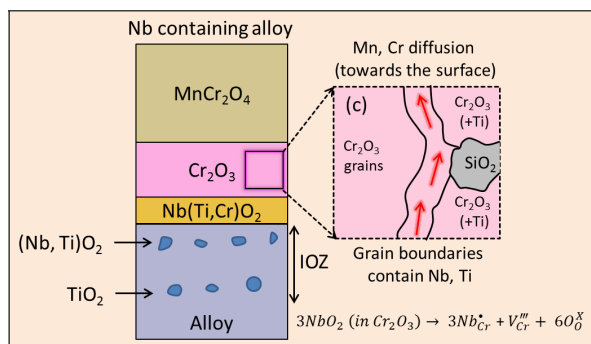


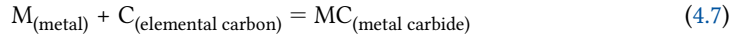
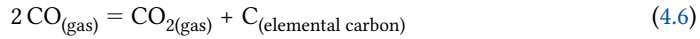
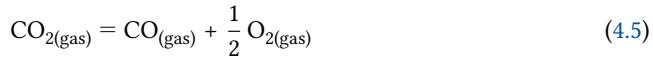
Figure 4.16: Schematic illustrating that the oxide scale composition and microstructure of Alloy–NT. Nb^{4+} segregation to the chromia scale GBs increases local concentration of Cr vacancies ($\text{V}_{\text{Cr}}^{\prime\prime\prime}$) leading to enhanced transport of Cr and Mn, and consequently higher weight gain in low $p\text{O}_2$ gases.

As shown in the previous section, APT revealed similar segregation activities for impurity elements in all gases implying that the vacancy concentrations and the associated increase in GB ionic conductivity must also be very similar in both low- and high- $p\text{O}_2$ gases. The other factor i.e. higher GB network density must have resulted in higher weight gain in Ar– O_2 , but the TG curves show the opposite behavior, rendering those factors as not decisive as well. On the contrary, the difference in porosity correlates well with the oxidation rate, so it (and

associated in-pore diffusion, either at walls for metal cations or direct for gases) appears to be the decisive factor.

4.7.2 Carbon transport through Cr_2O_3

The elemental carbon from carbon-rich gases diffuses rapidly into the base alloy through protective chromia (in case of chromia formers) and forms carbide precipitates in the alloy matrix at the vicinity of metal-oxide interface, according to the following equations [105]:



This is an indication that activity of carbon at metal-oxide interfaces is reasonably higher and results in carbide formation. The process of carbide formation in the alloy or at the metal-oxide interface during oxidation is known as carburization.

Nevertheless, no carbides were observed in the metal matrix, where the carbon amount in the Ar-CO-CO₂ is relatively low. Moreover, carbon-sensitive analytical techniques such as GD-OES and APT did not detect any carbon in the oxide scale or beneath it. This implies that carbon itself does not play any important role in the oxidation process under low $p\text{O}_2$ conditions. At the same time, the presence of carbon-containing gases entails high porosity of the chromia scale, but the responsible mechanisms remain unclear even with the use of nanoscale analysis methods in the current study.

Interestingly, in Ar-CO-CO₂, the entire chromia scale (from spinel-chromia interface to chromia-niobia interface) possesses pores which vary in size. The pores in chromia at the proximity of spinel-chromia interface are very fine whereas the pores at the chromia-niobia are coarser. This may occur due to the partial pressure gradient which exists across the oxide scale. The spinel-chromia interface being at slightly higher partial pressure gives rise to finer pores as compared to chromia-niobia interface which has coarser pores due to the comparatively lower oxygen partial pressure.

4.7.3 Chromia plate/whisker formation

Earlier studies showed that the presence of water (H_2O) in the exposed atmosphere led to accelerated oxidation during high temperature applications. The H_2O molecules act as more nucleating sites for oxidation to occur and result in very fine oxide structure. Presence of H_2O (in gaseous form) in the exposure gas can notably affect the oxidation behavior of Cr_2O_3 -forming materials when compared with that in air or in dry oxygen-based gases. Michalik et al. [106], have found that the oxidation rate of pure chromium in $\text{Ar}-\text{H}_2-\text{H}_2\text{O}$ is faster than in air-like gases ($\text{Ar}-\text{O}_2$). The oxide scale exhibited less tendency to buckle and more tendency to form whiskers at the surface of the scale compared to $\text{Ar}-\text{O}_2$.

The interesting observation on the oxide surface morphology in the present work is that the alloy exposed to high $p\text{O}_2$ shows globular type morphology, whereas the alloy exposed to low $p\text{O}_2$ shows plate-like morphology. Earlier studies report that H_2O is the key ingredient for the formation of plate or whisker type morphology. When Nguyen et al [107] studied $\text{Fe}-20\% \text{Cr}$ alloy in $\text{Ar}-20\% \text{CO}_2$ and $\text{Ar}-20\% \text{CO}_2-20\% \text{H}_2\text{O}$, the latter gas composition showed pronounced plate morphology. The gas $\text{Ar}-\text{CO}_2(+\text{H}_2\text{O})$ induced formation of fine Cr_2O_3 grains and the extent of Cr_2O_3 plate formation was increased as compared to $\text{Ar}-\text{CO}_2$. The Cr_2O_3 plates were found to be bi-crystals containing an internal interface (perpendicular to the alloy surface) which acts as fast diffusion pathway for Cr and/or Mn. Cross-sectional analysis showed that different plates grew by the competition between the thickening and lengthening (maintained by vapor phase deposition). Based on this observation, it was concluded that H_2O accelerated plate formation [107]. Contrary to this, in the present research, similar plate morphology was observed in both low $p\text{O}_2$ gases ($\text{H}_2-\text{H}_2\text{O}$ and $\text{CO}-\text{CO}_2$ containing), which means partial pressure of oxygen may be more influential in the plate-like morphology formation rather than H_2O itself.

4.8 Summary

The oxidation behaviour of the Alloy-NT was studied at 800°C in three model atmospheres relevant to the SOFC/SOEC operating conditions, namely $\text{Ar}-20\% \text{O}_2$, $\text{Ar}-4\% \text{H}_2-4\% \text{H}_2\text{O}$ and $\text{Ar}-1\% \text{CO}-1\% \text{CO}_2$. These atmospheres can be classified into high $p\text{O}_2$ ($\text{Ar}-20\% \text{O}_2$) and low $p\text{O}_2$ ($\text{Ar}-4\% \text{H}_2-4\% \text{H}_2\text{O}$, $\text{Ar}-1\% \text{CO}-1\% \text{CO}_2$) ones. The key findings of the present investigation can be summarized as follows:

1. The overall weight gain of the samples exposed in low pO_2 gases is significantly higher compared to high pO_2 gas, indicating faster oxidation. The mass transport through the forming oxide, as a limiting step, controls the oxidation process.
2. The oxide scale formed in these gas compositions showed a duplex structure consisting of outer spinel ($MnCr_2O_4$) and inner Cr_2O_3 . Besides, an additional thin $Nb(Cr, Ti)O_2$ rich rutile-type oxide layer forms at the metal/oxide scale interface.
3. TEM investigations of the chromia subscale, which acts as the key barrier separating the metal and the atmosphere, revealed formation of dense chromia with fine grain structure in high pO_2 atmosphere. On the contrary, low pO_2 atmosphere results in formation of the coarser grained and porous chromia layer.
4. APT revealed segregation of Mn, Ti and Nb at chromia grain boundaries for all atmospheres in approximately similar amounts. A high pO_2 level (Ar– O_2 atmosphere) additionally results in substantial accumulation of Mn and Fe impurities inside chromia grains, which was not observed in low pO_2 gases.
5. Comparison of various factors, potentially affecting the oxidation kinetics, revealed that the difference in porosity of the chromia layer appears to be responsible for the difference in oxidation rates, presumably by providing rapid diffusion paths at the pore walls or directly through pores. Other factors such as bulk diffusion, grain boundary ionic conductivity or the density of the GB network cannot explain the difference in oxidation rates.
6. Carbon from the Ar–CO– CO_2 atmosphere was found not to enter the oxide scale under low pO_2 conditions and therefore not directly influencing the oxidation process, unlike its reported behavior in high pO_2 carbon-containing atmospheres.

5

Role of minor alloying elements on high temperature oxidation

This chapter focuses on the investigation of oxidation behavior of Fe–22Cr–0.5Mn based ferritic steels with different additions of minor alloying constituents. Four steel samples, including the commercial steel Crofer 22 H, were oxidized using TG at 800 °C in a model Ar–4%H₂–4%H₂O atmosphere simulating the fuel side of the cell. APT was extensively used for obtaining atomic-scale insight into the segregation processes in the forming oxide scale. An additional focus was put on the metal–oxide interface, which is critical for the oxide scale adherence as well as the electrical conductivity of an interconnect. The oxidation mechanisms are discussed.

5.1 Oxidation Kinetics

Figure 5.1 shows the thermogravimetric data obtained during isothermal oxidation of the alloys at 800 °C in Ar–4%H₂–4%H₂O. All the studied alloys exhibited weight gain from the very beginning (transient oxidation stage). The base Alloy–NTS showed a maximal specific weight gain approximately equal to 0.18 mg cm⁻². When Alloy–T (i.e. Nb and Si were removed from the base alloy) was exposed, the maximum weight gain reduced to 0.13 mg cm⁻². However, for both Alloy–N and Alloy–NT (note excess Nb content compared to Alloy–NTS) the weight gain increased significantly.

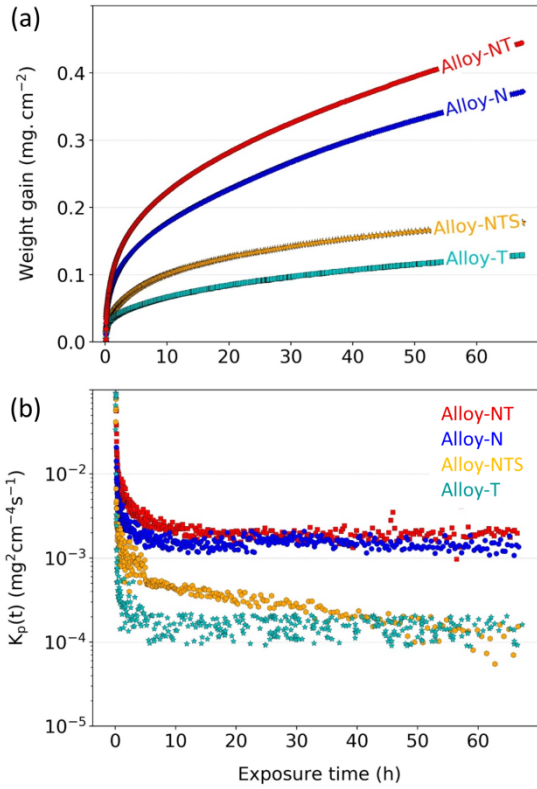


Figure 5.1: Thermogravimetric test results acquired during isothermal oxidation of four different alloys at 800 °C in Ar–4% H_2 –4% H_2O : (a) mass change as a function of the exposure time and (b) instantaneous *apparent* parabolic rate constant $k_p(t)$ as a function of the exposure time.

Figure 5.1b shows the instantaneous *apparent* parabolic rate constants $k_p(t)$ calculated from the mass change data plotted in Figure 5.1a. After an initial transient period of about 10 hours, the rate constants become virtually time independent, indicating approximate parabolic time dependence of the oxide scale thickness. This would be expected from the classical oxidation theory, if transport processes through the oxide are rate determining.

$$(\Delta m)^2 = k_p \cdot t \tag{5.1}$$

where Δm is the area specific weight gain (mg cm⁻²) and t is the exposure time (h).

5.2 Glow discharge optical emission spectroscopy

Figure 5.2 shows the GD–OES elemental depth profiles of various minor alloying elements in all the investigated alloys. All depth profiles showed Mn enrichment at the surface, suggesting spinel formation. Though the Mn content in these alloys is in the range 0.4–0.5 at. %, its concentration on the surface is quite low in case of Alloy–T. Interestingly, titanium peaks are observed in all Ti–containing alloys (except Alloy–N in Figure 5.2d). Particularly, the Ti peak concentration for Alloy–NT at the metal–oxide interface is relatively higher compared to Ti concentration peaks for Alloy–NTS and Alloy–T. The base alloy (Alloy–NTS) showed enrichment of several minor alloying elements such as Nb, W, Si and Ti, most likely at the metal–oxide interface. To retrieve more detailed information on the scale microstructure, the cross sectional analysis of oxidized samples by SEM and TEM was performed.

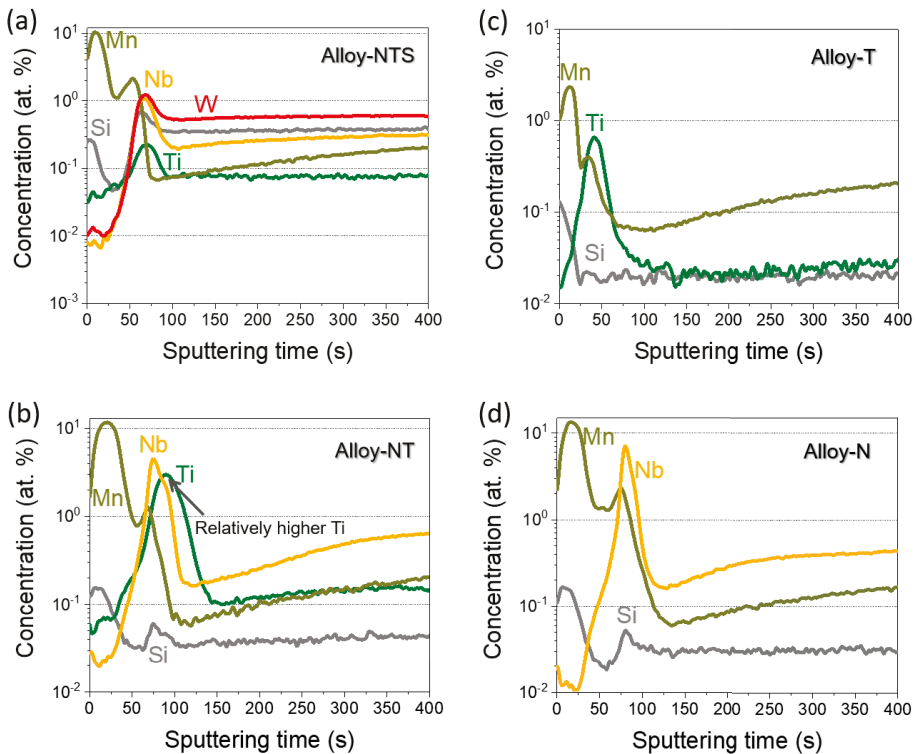


Figure 5.2: Glow Discharge–Optical Emission Spectroscopy (GD–OES) depth profiling of different alloys oxidized at 800 °C for 72 hours in Ar–4% H_2 –4% H_2O . (a) Alloy–NTS (Crofer 22 H), (b) Alloy–NT (KCL), (c) Alloy–T (Crofer 22 APU) and (d) Alloy–N (KCD).

5.3 Electron Microscopy analysis

5.3.1 Scanning electron microscopy (SEM)

SEM was used to examine the surface morphology as well as cross-section after oxidation in different gas compositions. Figure 5.3 depicts the surface morphologies and cross sections of the studied alloys as imaged by SEM. The oxides show a plate-like morphology with well-developed plates for Alloy-NT (Figure 5.3b) and Alloy-N (Figure 5.3d), whereas this morphology just started to develop on the surface of Alloy-T (Figure 5.3c). The cross-sectional SEM images show an oxide scale consisting of the outermost MnCr_2O_4 spinel and the inner chromia layers. Two Nb-containing alloys (Alloy-N and Alloy-NT) exhibit formation of an additional layer of 100–200 nm thickness between the chromia and the metal matrix. All Ti-containing alloys exhibit an internal precipitation zone underneath the oxide scale. In addition to the oxide phases, bright regions in Alloy-NTS and Alloy-NT indicate the presence of a Laves phase of the Fe_2Nb -base stoichiometry.

The average thicknesses of the different oxide subscales derived from SEM image analysis are presented in Table 5.1. It can be concluded that the overall oxide thickness increases after Nb addition to the alloy, correlating with the observations from the thermogravimetric data and indicating decrease in oxidation resistance. Comparison of Alloy-N and Alloy-NT reveals a qualitatively similar effect of Ti. Si addition to the alloy greatly mitigates the detrimental Nb influence and eliminates the formation of the additional inner layer between Cr_2O_3 and the alloy matrix.

Table 5.1: Thickness (in μm) of the various subscales in the surface oxide formed on the studied alloys.

	Full Scale	Spinel (outer)	Chromia	Nb-rich (inner) oxide
Alloy-NTS	1.1	0.3	0.7	–
Alloy-NT	3.1	1.8	1	0.35
Alloy-T	1	0.6	0.3	–
Alloy-N	2.1	0.9	1	0.25

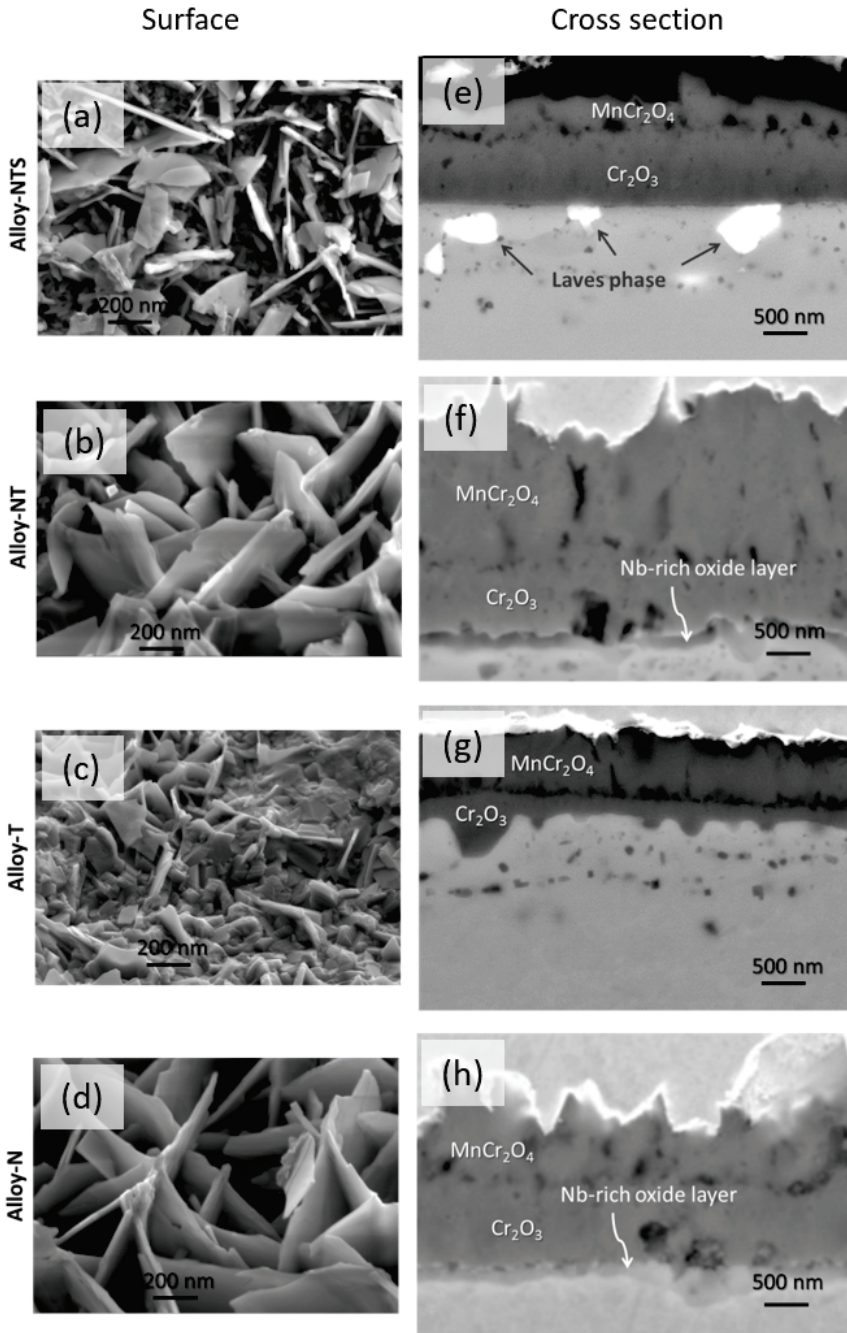


Figure 5.3: Surface morphologies (left column) and cross sectional (right column) SEM micrographs of the alloys exposed for 72 h at 800 °C in Ar-4%H₂-4%H₂O: (a) and (e) Alloy-NTS, (b) and (f) Alloy-NT, (c) and (g) Alloy-T, (d) and (h) Alloy-N.

5.3.2 Scanning transmission electron microscopy (STEM)

More detailed information on the oxide structure formed in the Ar–H₂–H₂O atmosphere was retrieved by STEM analysis. The results for Alloy–NTS and Alloy–N, which contain all minor additives, were obtained in bright field imaging mode in conjunction with EDS mapping and presented in Figure 5.4c.

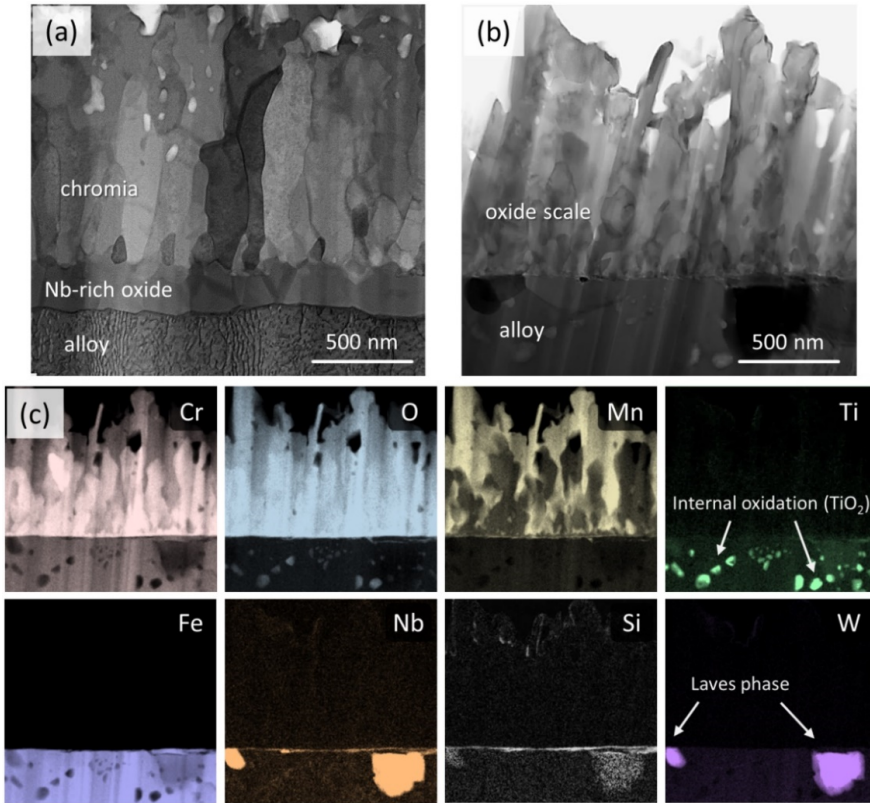


Figure 5.4: Bright-field TEM images of (a) Alloy–N and (b) base Alloy–NTS oxidized for 72 h at 800 °C in Ar–4%H₂–4%H₂O and (c) corresponding EDS elemental maps for Alloy–NTS.

Although a duplex spinel/chromia surface scale with fine-grained structure can be distinguished, EDS maps also reveal the presence of spinel grains deeply penetrating into the Cr₂O₃ layer. Additionally, a thin Si-rich layer was found by EDS at the alloy–oxide interface, which was not recognizable in SEM due to either its lower resolution or a small step formed on the

polished SEM cross-sectional sample around the metal–oxide interface. The region beneath the oxide scale contains numerous TiO_2 precipitates (internal oxidation zone) and a few Laves phase inclusions rich in Nb, Si and W.

Unfortunately, TEM was not able to provide reliable information about the chemistry at the grain boundaries and phase interfaces, especially when it comes to quantification of segregating species. These microstructural defects serve as fast diffusion paths and may be crucial for mass transport through the oxide scale and consequently, for understanding the oxidation mechanisms. To address these issues, atom probe investigations were performed.

5.4 Atom probe tomography (APT)

Though the external oxide consists of duplex microstructure containing outermost (at gas–scale interface) spinel and inner chromia (at spinel–alloy interface), the oxide growth is governed by ionic transport through chromia as it forms first during oxidation in the present situation. Therefore, in APT investigations emphasis has been put on the elemental distribution in chromia, especially on grain boundary segregation, as well as at the metal–oxide interface, which is important for the oxide scale adhesion and electrical properties of the oxidized alloy.

5.4.1 Alloy–NTS

A Chromia scale

Figure 5.5a shows APT elemental maps of key impurities detected in the Cr_2O_3 scale formed on the Alloy–NTS (base alloy). Mn shows a clear tendency to segregate at chromia GBs and is also present in local Mn–rich regions with compositions matching MnCr_2O_4 spinel, i.e. it forms inner spinel inclusions in chromia. Figure 5.5b and Figure 5.5c show averaged elemental concentration profiles across chromia GBs and proximity histograms [94] across chromia/spinel interfaces, respectively. Ti and especially Nb segregate to grain boundaries at substantially lower levels compared to Mn. Si exhibits a weak tendency to GB segregation and additionally enters, in marginal amounts, into the inner spinel precipitates. Al appears as a solute element in the chromia grains without any tendency to segregate at the GBs.

Table 5.2: APT bulk composition of chromia scales formed in different gas atmospheres relevant to SOFC/SOEC.

	O	Cr	Mn	Si	Ti	Nb	Al
Alloys – NTS (base)	57.8	42	0.07	0.02	0.09	0.004	0.004
Alloys – NT	56.2	41.9	0.06	0.09	0.8	0.1	0.06
Alloys – T	56.3	42.7	0.1	0.01	0.7	–	0.04
Alloys – N	58.7	41.0	0.06	–	–	0.1	0.001

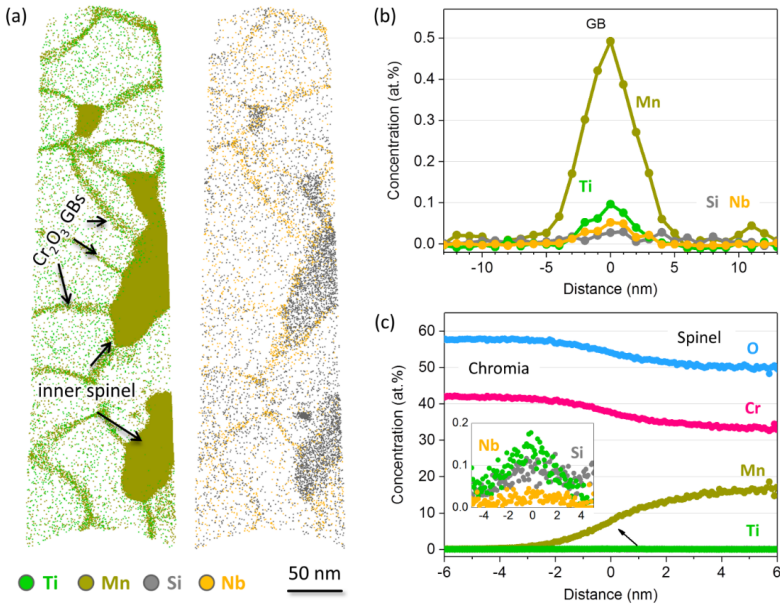


Figure 5.5: APT analysis of the Cr₂O₃ scale thermally grown on Alloy–NTS (base alloy) during oxidation at 800 °C in Ar–4%H₂–4%H₂O: (a) atom maps of Ti, Mn, Si and Nb; (b) elemental concentration profiles across GBs in the chromia scale; (c) proximity histograms across an interface between chromia and inner spinel grains. The inset shows a magnified view at the same interface to highlight minor impurities.

Table 5.2 summarizes the bulk composition of the chromia phase in all studied alloys, including both grains and grain boundaries. All measurements show oxygen deficiency by 2–4 at. % as compared to the nominal Cr_2O_3 stoichiometry. Such a deficiency is often observed in APT analysis of many oxide materials [102, 103], as mentioned earlier, and can be explained by artifacts originating from the field evaporation process, i.e. not related to any true non-stoichiometry of the oxide phase. Despite pronounced GB segregation, the total amount of impurities in chromia is low for Alloy–NTS, not exceeding 0.1 at. % for each element. This may indicate sluggish bulk diffusion of metal cations through chromia (especially of Mn needed to form a spinel layer above Cr_2O_3) resulting in a relatively lower oxidation rate.

B Metal–oxide interface

Since the electron microscopy analysis revealed formation of additional layers at the metal–oxide interface of three of the four studied alloys, this region was selected for a further APT analysis. Figure 5.6 shows combined APT elemental maps for the chromia–alloy interface for the base Alloy–NTS. The chemical structure around the interface appears complex, with a substantial accumulation of Nb, Si and Mn (≥ 10 at. % local concentrations) detected in this region.

Elemental concentration profiles in Figure 5.6b demonstrate that concentration peaks of these elements are spatially displaced with respect to each other, evidencing formation of a multilayer nanostructure instead of a usual segregation pattern. A more detailed analysis reveals formation of a ragged island–like interfacial multilayer, especially for Mn and Si. The peak Mn concentration indicates possible formation of an interfacial thin MnCr_2O_4 spinel layer, in addition to inner spinel grains formed inside the chromia scale. Beneath the spinel–like layer, a few nm thick Si– and O–rich layers emerge with local Si concentrations up to 40 at. %, indicating formation of numerous SiO_2 phase regions. These SiO_2 regions do not form a continuous film separating the oxide scale from the alloy. Beneath the SiO_2 region an additional thin layer of an Nb–rich oxide can be distinguished, that contains also minor additions of W and Ti. Other alloying elements and impurities (Al, La, B and C) were not detected around the metal–oxide interface.

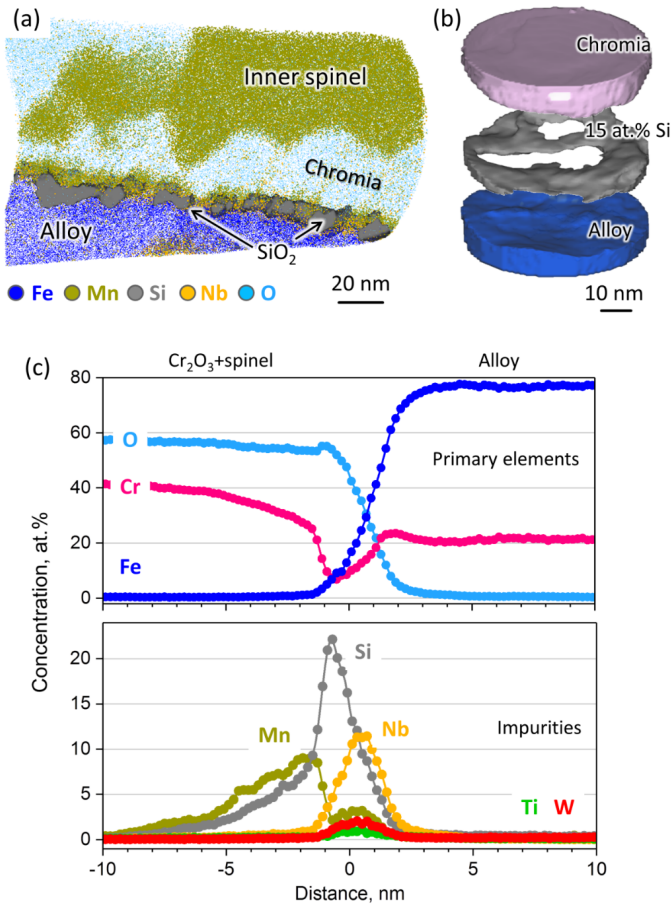


Figure 5.6: APT analysis of the oxide–alloy interface region in Alloy–NTS (base alloy) after oxidation at 800 °C in Ar–4% H_2 –4% H_2O : (a) combined atom maps for the chromia–alloy interfacial region; (b) 15 at. % Si iso–concentration surface delineating the net–like SiO_2 layer forming at the metal–oxide scale interface; (c) proximity histograms across the interface for major and minor alloying elements.

5.4.2 Alloy–NT

A Chromia scale

Figure 5.7 shows APT atom maps of the inner (chromia) scale. The bulk chromia composition presented in Table 5.2 shows that the main impurity in chromia is Ti, which amounts to 0.8

at. %. The Ti concentration in the grain interior was slightly lower (approximately 0.6 at. %) than at the GBs. Additionally, segregation of Nb and Mn were also detected.

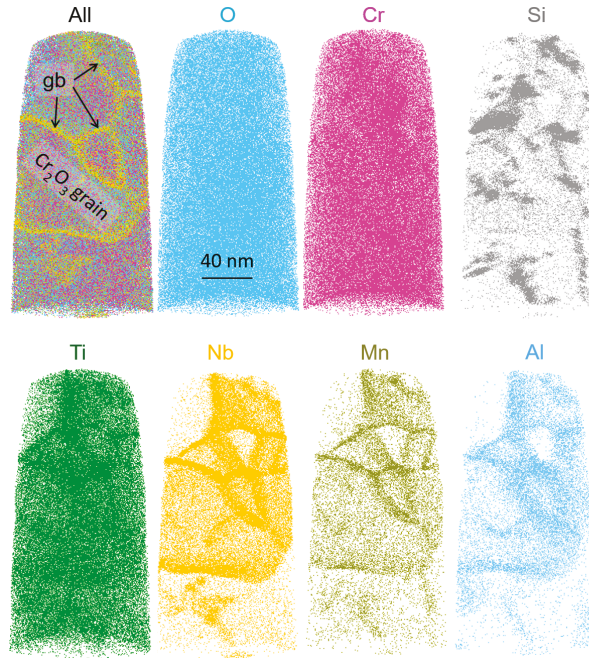


Figure 5.7: APT atom maps for the inner chromia scale formed on Alloy-NT after isothermal oxidation at 800 °C in Ar-4% H_2 -4% H_2O for 72 hours.

In spite of low Si concentration in the investigated alloy (Table 3.1), it was observed in the chromia scale with an average concentration of approximately 0.08 at. %. However, the segregation pattern is quite different compared to that of the other elements. Si does not appear on all GBs, but instead displays an *island-like* segregation pattern as shown in Figure 5.7. Detailed analysis of the APT data reveals that at least a fraction of Si-rich islands exhibit SiO_2 stoichiometry without any notable impurities.

A small sub-volume consisting of three adjacent chromia grains was extracted from the presented dataset and analyzed in detail for better insight into the segregation behavior. Figure 5.8a shows dissimilar GB segregation of Nb, Ti, Mn, Si and Al. The concentration of segregated elements at the different GBs as well as in the grains varies. Figure 5.8b depicts the concentration variation across these three GBs and grains. On average, 0.8 at. % and 2.6 at. % of Ti is present in chromia grains and GBs, respectively. Slight overestimation of Ti content in grains over its bulk concentration (Table 5.2) value ensues here due to the overlap of O_2^{++} and

TiO⁺⁺ peaks in the mass spectrum, which was not deconvoluted in the concentration profiles. Nevertheless, the overlap is relatively small and does not essentially affect the Ti quantification from APT data. Similarly, 0.1 at. % and 1.2 at. % of Nb are present in chromia grains and at GBs, respectively. Mn also exhibited qualitatively similar behavior, but its maximum concentration is only 0.4 at. %. In the case of Al, no similar segregation pattern was found, rather it is present in some chromia grains and absent in others. It is also clear that Si appears as GB segregating element and also as Si-rich oxide particle formed in the chromia scale.

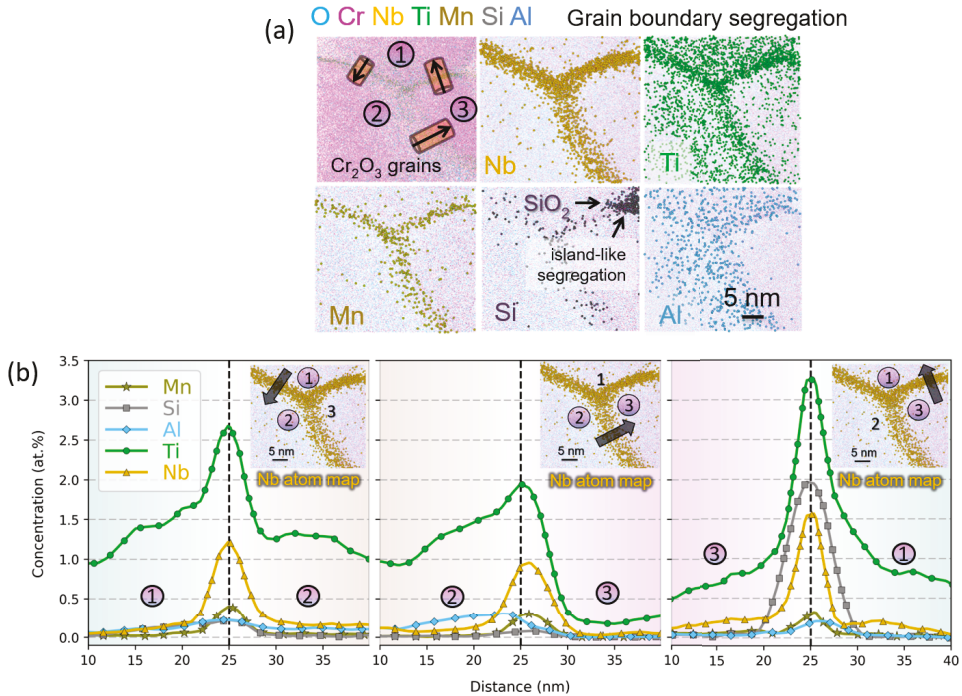


Figure 5.8: APT analysis of a GB region in chromia scale formed on Alloy-NT oxidized isothermally at 800 °C in Ar-4%H₂-4%H₂O for 72 h. (a) Atom maps of impurities present in the GB region showing dissimilar segregation behavior. (b) Elemental concentration profiles across the GBs..

B Metal-oxide interface

Figure 5.9 shows the results of APT analysis of the oxide-metal interfacial region. From the bulk compositional analysis (see Table 5.2), the stoichiometry of the Nb-rich oxide layer formed at the Cr₂O₃-alloy interface is Nb(Ti, Cr)O₂. In addition to the oxide-alloy interface, it also shows a GB in the oxide phase enriched with Mn (Figure 5.9a) with a peak concentration

of approximately 0.4 at. % (Figure 5.9c) and no other elements segregate here. At the oxide–alloy interface (Figure 5.9d), only Si segregation is observed with a peak concentration of approximately 1.5 at. % (Figure 5.9e). Nevertheless, no SiO₂ layer or inclusions were observed at the interface in this alloy, unlike the SiO₂–rich Alloy–NTS.

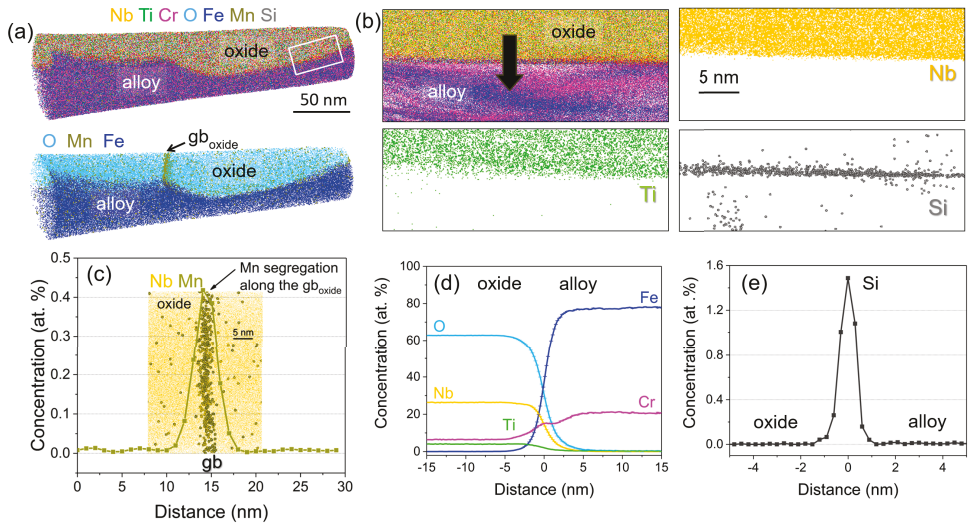


Figure 5.9: APT analysis of the oxide/alloy interface region in Alloy–NT after isothermal oxidation at 800 °C in Ar–4% H_2 –4% H_2O for 72 hours. (a) A combined atom map for major elements from the regions near the interface between oxide and alloy. (b) Magnified interfacial region from (a) with atom maps for Nb, Ti and Si. (c) Concentration profile of Mn across the GB in the oxide scale. (d), (e) Proximity histograms across the oxide/alloy interface for major alloying elements and Si, respectively.

5.4.3 Alloy–T

A Chromia scale

Figure 5.10 shows the results of the chromia scale formed in Alloy–T, and the individual atom maps show that both Ti and Mn segregate to chromia GBs. Moreover, Ti is also soluble in the chromia grains. The quantitative analysis determines the concentration of these impurities. Figure 5.10b shows that about 1.4 and 0.6 at. % of Ti and Mn respectively, are present as GB segregants. Approximately 1 at. % of Ti is dissolved in the chromia scale in the given alloy, whereas Mn showed almost no solubility.

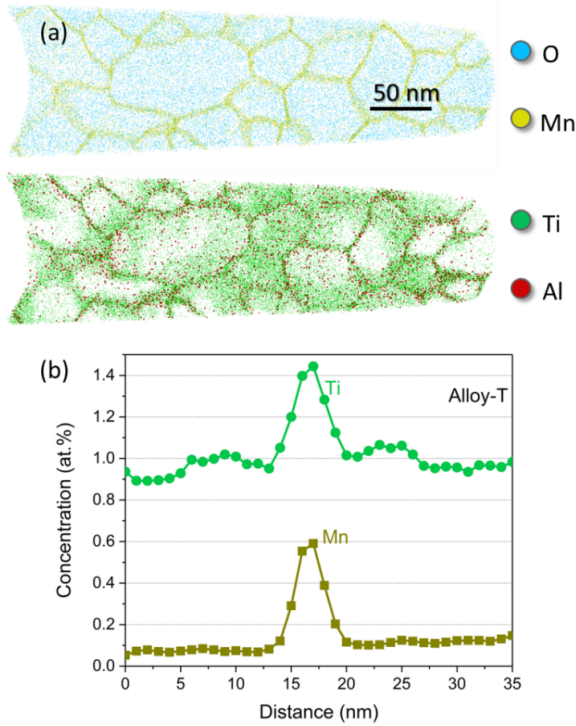


Figure 5.10: APT analysis of the chromia scale on Alloy-T (without Nb and Si) oxidized isothermally at 800 °C in Ar-4% H_2 -4% H_2O for 72 hours. (a) Atom maps of alloying elements present in Cr_2O_3 and (b) concentration profiles across a grain boundary for primary segregants (Ti and Mn).

B Metal-oxide interface

Compared to other alloys, Alloy-T (without Nb and Si) showed a direct junction of the chromia scale and alloy matrix, as can be seen from Figure 5.11. Continuous Ti segregation with a peak concentration of 2.5 at. % was detected at the interface. Neither segregation of other elements nor precipitation of other phases was found at the interface or in its vicinity. Intermittent Mn-rich regions were observed in the chromia scale close to the interface, indicating possible presence of inner spinel precipitates.

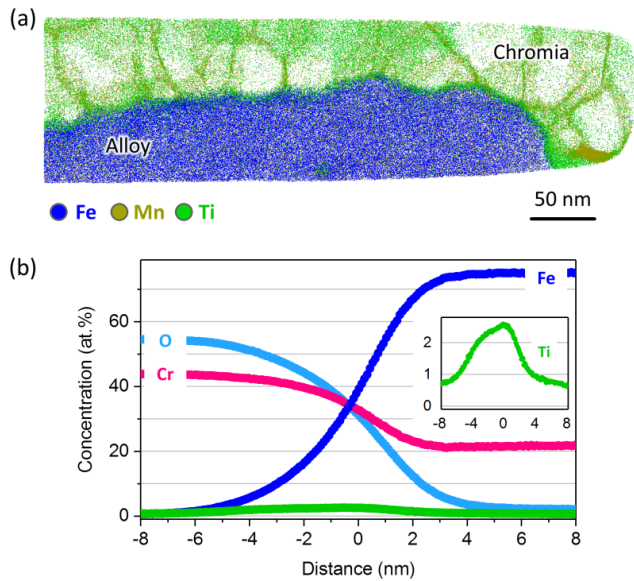


Figure 5.11: APT analysis of the chromia–alloy interface region in Alloy–T (without Nb and Si) after 72 h oxidation at 800 °C in Ar–4% H_2 –4% H_2O : (a) a combined atom map and (b) proximity histograms across the chromia–alloy interface. A magnified inset highlights Ti segregation at the interface.

5.4.4 Alloy–N

A Chromia scale

The chromia scale was analyzed using APT and the results are shown in Figure 5.12. The atom maps (Figure 5.12a) show GB segregation of Nb and Mn in the chromia phase. Elemental concentration profiles built across chromia GBs (Figure 5.12b) show substantial GB enrichments for Nb and Mn of 0.8 and 0.3 at. %, respectively.

Aluminum was detected predominantly as a non-homogeneous solute in grain interiors, exhibiting no tendency to GB segregation. La, B and C were not found in the chromia either as solute impurities or at grain boundaries.

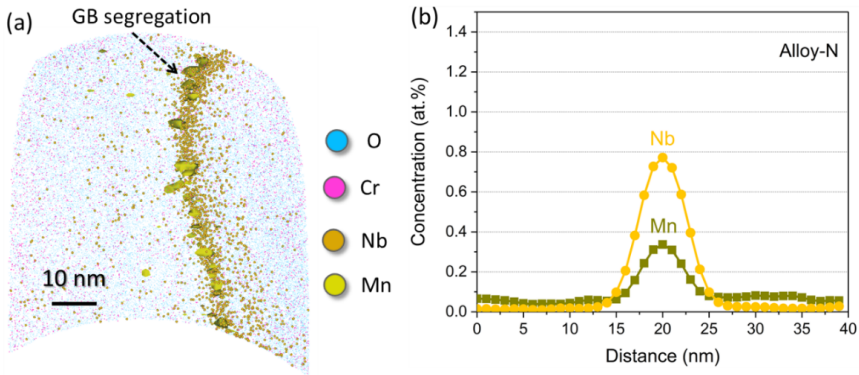


Figure 5.12: APT analysis of chromia scale on Alloy-N (without Ti and Si) oxidized isothermally at 800 °C in Ar-4% H_2 -4% H_2O for 72 h. (a) Atom maps of alloying elements present in Cr_2O_3 (Nb and Mn) and (b) concentration profile of grain boundary segregants (Nb and Mn) for the Cr_2O_3 phase.

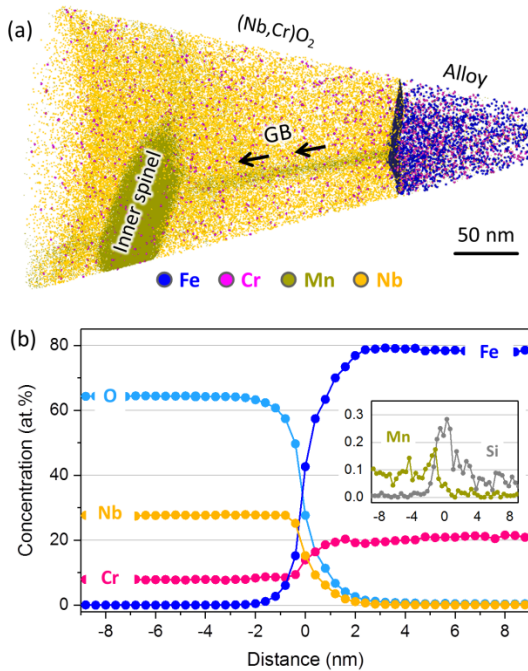


Figure 5.13: APT analysis of the oxide-alloy interfacial region in Alloy-N (without Ti and Si) after 72 h oxidation at 800 °C in Ar-4% H_2 -4% H_2O : (a) atom maps demonstrating formation of a $(Nb,Cr)O_2$ layer next to the alloy; (b) proximity histograms across the metal-oxide interface showing weak Si segregation.

B Metal–oxide interface

Unlike the base alloy (Alloy–NTS), the two other Nb–containing alloys (Alloy–NT and Alloy–N) form a thick continuous Nb–rich oxide between chromia and alloy. Figure 5.13 presents an elemental map for the interfacial region and corresponding concentration profiles across the oxide–alloy interface for Alloy–N. APT reveals this oxide layer stoichiometry being close to NbO₂ rutile phase with partial substitution of Nb with Cr. Si was found at the interface as weak homogeneous segregation, i.e. no interfacial SiO₂ layer forms in these Si–lean alloys.

Other minor alloying elements (Al and La) were not detected in (Nb, Cr)O₂ oxide or at the metal–oxide interface. An additional noticeable feature in the NbO₂–base layer is the presence of Mn enrichment at grain boundaries, with occasional appearance of inner spinel precipitates.

5.5 Discussion

5.5.1 General considerations of GB influence on the oxidation behavior

As mentioned above, earlier studies of the oxidation behavior of high–Cr ferritic steels concluded that chromia is the first oxide scale forming on the alloy surface under high–temperature oxidation [108]. This determines the key role of chromia GBs for further oxide scale growth and the formation of the spinel layer. In particular, both inward diffusion of oxygen and outward diffusion of metal species can be strongly influenced by creating defects in the host lattice [20]. Substitution of the host ions (Cr³⁺) at GBs with segregating ions of different charge states either promotes the formation of vacancies due to the necessity to maintain charge neutrality or alters the space–charge distribution [109, 110] and can eventually accelerate the mass transport. To understand the mechanism of the segregation effect, not only the types but also the amounts of segregating species need to be analyzed.

Beside the elemental segregation, the density of the grain boundary network also directly affects the mass transport, since it determines the amount of fast diffusion paths. A denser GB network provides higher total diffusion flux and must entail faster oxidation rate in the present case of the diffusion–controlled oxidation process. Comparison of chromia grain sizes for the alloys reveals however the opposite (see TEM in Figure 5.4b): the Alloy–NTS sample with smaller chromia grains (denser GB network) shows essentially slower oxidation in comparison to the larger–grained sample of the Alloy–NT. It should be also mentioned that chromia formed in Ar–4%H₂–4%H₂O atmosphere shows quite low porosity for all alloys,

rendering this factor irrelevant to the observed dependency of the oxidation rate on the alloys composition. On the other hand, GB segregation behavior in chromia varies substantially with the composition, thus indicating the dominating role of the GB ionic conductivity, which is discussed below.

Table 5.3: Gibbsian interfacial excess values G_i for grain boundary segregation in the chromia scale.

Interfacial excess at/nm ²	Mn	Ti	Nb	Summary (Mn+Ti+Nb)
Alloy-NTS	2.4	0.6	0.4	3.4
Alloy-NT	1.2	11	6	18.2
Alloy-T	1.6	5	–	6.6
Alloy-N	1.0	–	6	7

5.5.2 Quantification of GB segregation from APT data

Calculation of the Gibbsian interfacial excess G_i , i.e. the number of segregating atoms of the element i per GB unit area, represents a convenient and physically explicit way for quantifying and comparing GB segregation [111]. Interfacial excess values can be easily derived from APT data [112, 113] and, apart from that, are less affected by the data analysis artifacts as compared to other usual metrics, e.g. peak elemental concentrations at GB.

Table 5.3 summarizes the Gibbsian interfacial excess values G_i for the key elements segregating at chromia scale GBs. At least three grain boundaries were used to calculate G_i for each element in each alloy, and the average value was taken. G_i values reveal substantial variations in segregation activity of the same element, with the most significant difference observed for Ti and Nb between Alloy-NTS and the other alloys.

Comparing the summary interfacial excess values with the densest cationic planes in the corundum type Cr_2O_3 phase (≈ 10 at/nm² at the (110) plane) and considering that a random GB generally has a lower cationic density, it can be concluded that the summary interfacial excess approaches or even exceeds (at least for Alloy-NT) a monolayer GB coverage, which must essentially alter the microstructure and properties of the GBs.

5.5.3 Elemental diffusion through the chromia scale

As discussed above, Nb in the chromia scale must appear as aliovalent Nb^{4+} or Nb^{5+} ions under the given oxidation conditions. Replacement of Cr^{3+} with aliovalent Nb ions was assumed to engender formation of GB cation vacancies in order to maintain charge balance, which accelerates the outward diffusion fluxes of metallic ions, especially of Mn needed to form the top spinel layer. This mechanism can explain the high oxidation rate of Nb-containing alloys: Alloy-N and Alloy-NT indeed demonstrate high G_{Nb} values, i.e. high segregation activity of Nb. The slowly oxidizing base Alloy-NTS shows the extremely low G_{Nb} at chromia GBs, probably due to the intensive Nb consumption for Laves phase formation in presence of Si [27] (visible in TEM in Figure 5.4b). The lowest oxidation rate of the Nb-free, Alloy-T also aligns with the proposed mechanism.

A similar influence on the vacancy formation in chromia and eventually on the oxidation rate could be expected from titanium, once Ti ions also possess charge state of at least 4+ in the entire oxide scale (TEM-EDX shows formation of TiO_2 precipitates underneath the metal-oxide interface). Moreover, Ti was also found within chromia grains with concentrations up to 0.8 at. %, which must generate bulk vacancies via the Wagner-Hauffe doping [20] and thereby additionally contribute to the ionic mass transport through the chromia scale. Nevertheless, Alloy-N exhibits much faster oxidation than Alloy-T despite the very close G_{Mn} and G_{Ti} values, see Table 5.3. This observation indicates that the GB doping with aliovalent ions does not fully explain at least the effect of Nb.

Since GB coverage with segregating Nb and Ti reaches or even exceeds a monolayer thickness, as discussed above, one can assume formation of a thin GB layer with a local atomic environment corresponding to another phase rather than Cr_2O_3 . Earlier studies discovered the existence of the rutile-type CrNbO_4 phase with a wide cationic concentration range [114]. Involvement of a substantial amount of Cr for the phase formation must expand its volume to two or more atomic layers, rendering alteration of the local atomic environment at GBs more likely. The inner NbO_2 -base rutile layer detected in Alloy-N and Alloy-NT shows a relatively high-Cr concentration (up to 10 at. %), which aligns with the wide range of Cr solubility in the rutile phase. Besides, the alloys forming this additional oxide layer demonstrate high oxidation rate, indicating high permeability of the rutile phase for metallic cations. If an off-stoichiometric rutile-type local environment forms at the chromia GBs, this may accelerate GB diffusion more aggressively than the Wagner-Hauffe doping. To prove the viability of this mechanism, an accurate high-resolution TEM analysis of the GB regions could be helpful in the future.

Mn forms aliovalent ions of 2+ charge state in the chromia layer, since this charge state is characteristic for the topmost MnCr_2O_4 spinel with the highest $p\text{O}_2$ level, i.e. with the highest possible charge state in the oxide scale. In terms of GB vacancy formation, this should counterweigh the effect of Nb and Ti. Most notable here is the base Alloy–NTS, where Mn segregation at GBs exceeds that of Ti and Nb together ($G_{Mn} > G_{Ti} + G_{Nb}$), which should reverse the charge balance at GBs towards positive charge deficiency. This can be mitigated by partial removal of negative charge, i.e. by creation of oxygen vacancies, promoting inward oxygen transport instead of outward cation diffusion. This mechanism may explain the small thickness of the outer spinel layer in Alloy–NTS (due to slow outward Mn diffusion) as well as appearance of small chromia grains in the vicinity of the metal–oxide interface (fast O^{2-} diffusion promotes inner nucleation of Cr_2O_3), which are distinguishable in TEM and even in APT by the GB segregation pattern (see Figure 5.11a). Slow Mn diffusion is also possibly responsible for the extensive formation of the inner spinel grains in Alloy–NTS due to accumulation of Mn at grain boundaries (the highest G_{Mn} value among all alloys) with further nucleation and growth of the MnCr_2O_4 phase in the inner region of the chromia.

5.5.4 Intermittent oxide phases between chromia and alloy

The Nb–containing alloys (Alloy–NT and Alloy–N) were found to form substantially thicker oxide scales compared to the Alloy–NTS and Alloy–T. The effect is partly related to the formation of an additional Nb–rich oxide at chromia–alloy interface. For unit metal activities, the oxides in equilibrium with Nb and Cr are NbO and Cr_2O_3 , respectively. The dissociation oxygen partial pressures ($p\text{O}_2$) of these oxides at 800 °C equal to 10^{-31} atm and 10^{-27} atm, respectively [47]. Since the metal activities in the alloy are generally less than unity, these values appear underestimated. Additionally, under the given Nb activity, NbO_2 will become thermodynamically more stable than NbO [47]. Assuming in the first approximation that the metal activities are close to their mole fractions in the alloy matrix, the activities for Cr and Nb would be 0.2 and 0.001, respectively. Besides, the $p\text{O}_2$ for the equilibrium NbO/ NbO_2 at 800 °C equals to 10^{-27} atm, being quite close to the dissociation pressure of chromia for unit metal activity. This explains why an NbO_2 rather than an NbO type oxide is formed at the scale/alloy interface in Alloy–NT and Alloy–N. An earlier study also showed that Nb oxidizes beneath the chromia scale in high–Cr ferritic steels [48]. The stoichiometry and structure of the Nb–rich oxide layer indicates the 4+ oxidation state of Nb in the inner oxide scale regions. In the outer part of the oxide scale, Nb can also exist as 5+ ions as the dissociation oxygen partial pressure of Nb_2O_5 to NbO_2 at 800 °C is 10^{-22} atm, which is lower than the equilibrium oxygen partial pressure of the test gas ($\text{Ar} - 4\% \text{H}_2 - 4\% \text{H}_2\text{O}$, 10^{-19} atm).

After the formation of the Nb-rich oxide layer, the further growth of chromia and Mn-Cr spinel (MnCr_2O_4) in the outer part of the scale requires diffusion of Mn and Cr through this underlying oxide. Mn can efficiently diffuse through the chromia layer via its GBs, as directly demonstrated by APT in Alloy-NT (Figure 5.9a) and in Alloy-N (Figure 5.13a). Cr can diffuse through GBs as well as through the bulk of the Nb-rich oxide, as indicated by a relatively high-Cr concentration in this layer: 6 at. % in Alloy-NT and 9 at. % in Alloy-N. Alloy-NTS also forms a thin Nb-rich oxide layer, as indicated by the Nb concentration peak at the metal-oxide interface (see Figure 5.9d), but high Nb consumption by the Laves phase limits its thickness to only a few nm.

Analysis of the interfacial region in Alloy-NTS reveals also the formation of an additional Si-rich oxide layer. A continuous SiO_2 layer at the metal-oxide interface is considered being strongly detrimental for the interconnect performance in an SOFC/SOEC due to its high electrical resistivity. TEM-EDS analysis indeed shows an apparently continuous Si-rich oxide at the interface (Figure 5.4c). APT analysis confirms the SiO_2 stoichiometry of these Si-rich regions but reveals its net-like morphology with only partial interface coverage (see Figure 5.6b). Open windows in the SiO_2 layer should provide the necessary electrical conductivity after oxidation, thus not restricting an interconnect plate made of this alloy to function as a current collector in fuel/electrolysis cell devices. Nevertheless, the interfacial coverage with SiO_2 turned out to be quite high, indicating the Si concentration of 0.42 at. % in Alloy-NTS (commercial Crofer 22 H) as potentially being close to the maximum acceptable level.

5.5.5 Reactive element effect

An additional comment should be made on the role of La as a reactive element. As mentioned earlier, previous studies concluded that it has a positive influence on the oxide scale adherence on many high-Cr steels [29]. The assumed explanations for the La effect were (1) its segregation at the metal-oxide interface and thereby direct alteration of the adhesion properties and (2) binding detrimental impurities, first of all sulfur, inside the cast alloy. La was added to three of the studied alloys in order to directly check the former assumption by APT. Peaks of La or LaO_x ions in the APT mass spectra must reside not overlapping with other ions, so La detection was expected to be easy. Nevertheless, no La was found in any part of the oxide scale, at the metal-oxide interface or in the alloy directly beneath the interface. This observation rules out the first mechanism of direct interfacial segregation for La.

5.6 Summary

A detailed APT analysis of four high-Cr ferritic steels of the regions influencing the diffusion through the oxide scale (chromia and metal-oxide interface) revealed the determining role of GB segregation in the oxidation processes, and established relationships between the composition, the microstructure and oxidation behavior. The main conclusions can be formulated as follows:

1. Mn, Ti and Nb actively segregate at chromia GBs. Gibbsian interfacial excess G_i values indicate a monolayer or higher GB coverage with Nb+Ti in alloys with low Si amount. Substitution of the host Cr^{3+} ions with higher-charged $\text{Nb}^{4+}/\text{Nb}^{5+}$ and Ti^{4+} ions (Wagner-Hauffe doping) can promote formation of cationic vacancies, thereby accelerating outward cation diffusion along GBs and eventually increasing the oxidation rate. Nevertheless, the vacancy formation mechanism cannot solely explain the much stronger effect of Nb compared to that of Ti, indicating possible alteration of GB structure in presence of Nb with further changes in their diffusion properties.
2. Addition of Si promotes Laves phase formation, which actively binds Nb and prevents it from entering oxide phase (into both lattice and GBs), thereby providing a low oxidation rate for Alloy-NTS. However, Si amount of about 0.4 at. % in the alloy causes formation of a net-like SiO_2 layer at the metal-oxide interface, which may become continuous at higher Si levels and therefore critical for the electrical properties of the interconnects.
3. GB segregation of lower charged Mn^{2+} ions mitigates the effect of Nb and Ti ions. A relatively high Gibbs interfacial excess of Mn (G_{Mn}) in comparison to $G_{\text{Nb}} + G_{\text{Ti}}$ (Alloy-NTS) exhibit slow oxidation, which may be explained by lower concentration of cation vacancies and even the counter-formation of oxygen vacancies promoting inward O diffusion. This results in slow growth of the outermost spinel layer and formation of inner spinel grains (due to slow outward Mn diffusion) in Alloy-NTS.
4. Nb-containing alloys with low Si content exhibit an additional rutile-type $\text{Nb}(\text{Cr}, \text{Ti})\text{O}_2$ layer between chromia and metal matrix. This layer does not inhibit outward diffusion of Mn (proceeding through GBs) and Cr (proceeding through GB and bulk) necessary to form the main chromia/spinel scales. Higher Si addition binds Nb and makes this layer disappear.

5. La (reactive element) was not detected in the oxide scale as well as around the metal-oxide interface for all La-containing alloys, ruling out mechanism of direct interfacial segregation for La.

6 Internal oxidation

This chapter is focused on the internal oxidation zone (IOZ) formation in various Crofer family steels, particularly on the chemistry of internal oxide particles and their interface with the metal matrix. Also the role of partial pressure of oxygen on the internal oxidation was considered. Particular focus was put on the role of alloy grain boundaries, oxide particle chemistry and the subsurface strengthening mechanisms are discussed.

6.1 Scanning electron Microscopy (SEM)

Figure 6.1 shows the cross-sectional scanning electron microscopy images performed on all four alloys investigated in this research. These alloys show the duplex nature of an external oxide, containing outermost spinel and inner chromia scale. Additionally, internal oxidation zone (IOZ) consists of oxide particles (dark spots) are observed in various sizes and shapes, except for Alloy-N, as it is the only alloy which is free of Ti. Therefore, it can be concluded that Ti is the key element involved in the formation of internal oxide particles. Alloy-NT possesses the highest concentration of Ti (about 0.17 at. %) compared to other alloys. It is interesting to note that the Alloy-NT showed pronounced internal oxidation, since the density of the internal oxide particles is higher compared to other alloys. Therefore, emphasis has been put on characterizing the internal oxide particles present in the Alloy-NT using TEM and APT.

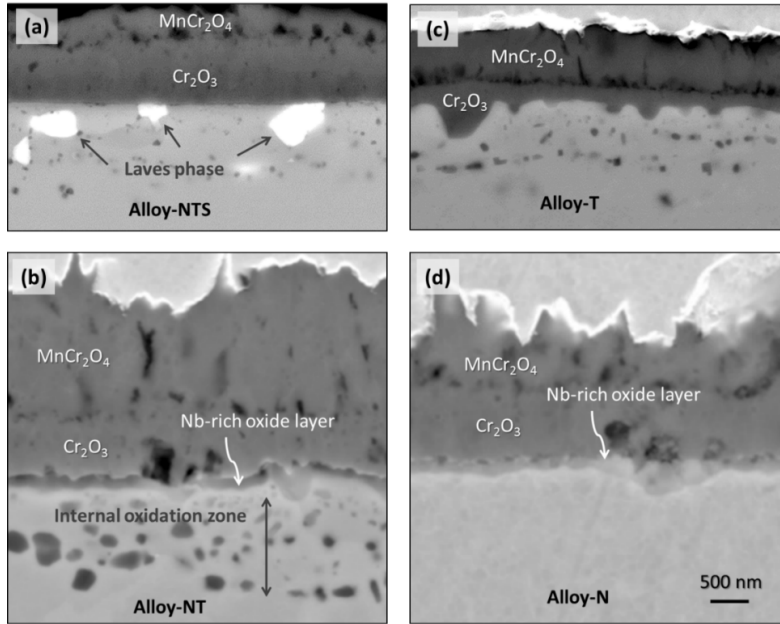


Figure 6.1: SEM micrographs of the cross sectional samples from different alloys oxidized at 800 °C for 72 hours in Ar-4% H_2 -4% H_2O . (a) Alloy-NTS (Crofer 22 H), (b) Alloy-NT (KCL), (c) Alloy-T (Crofer 22 APU) and (d) Alloy-N (KCD). All images are shown at same magnification. The alloys' names given in the parenthesis refer to their designations in commercial use or in the lab as well as in our earlier publications.

6.2 Transmission electron Microscopy (TEM)

Figure 6.2 shows TEM characterization of Alloy-NT with high magnification view of internal oxidation zone (IOZ) in Figure 6.2b. Based on the EDS analysis of the IOZ, it can be concluded that the presence of both Ti and Nb results in fine internal oxide particles of $(Nb, Ti)O_2$ stoichiometry which are non-spherical at the vicinity of metal oxide interface. As the depth increases, Nb content in these particles decreases, and solely round TiO_2 are observed. This is due to the fact that partial oxygen pressure required for Nb to form oxides is relatively higher (can be inferred from Ellingham diagram in Chapter 2) compared to Ti to form TiO_2 .

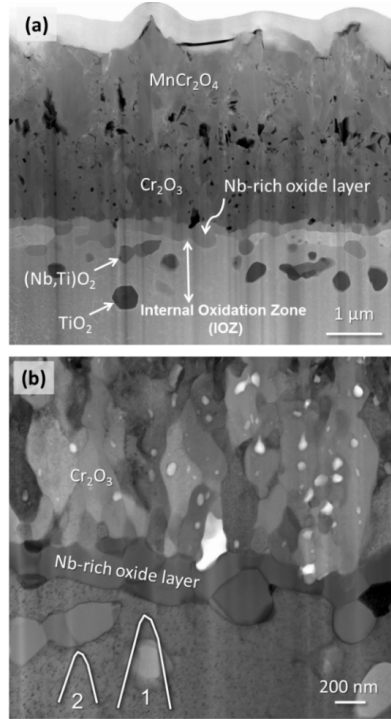


Figure 6.2: Bright-field TEM images of Alloy-NT oxidized at 800 °C for 72 hours in Ar-4% H_2 -4% H_2O . (a) Low magnification and (b) corresponding high magnification image showing metal-oxide interface and the internal oxidation zone.

Moreover, high magnification TEM image in Figure 6.2b showed two different sized precipitates, which are marked as regions 1 & 2. Region 1 shows coarse oxide particles, whereas region 2 shows fine oxide precipitates (dark spots), both embedded in the metal matrix. As the metal matrix (lattice) and the matrix-oxide particle interface acts as pathway for the ingress of oxygen, these local regions must be analyzed, and APT was used for this purpose.

6.3 Atom probe tomography (APT)

Figure 6.3a shows the results of APT analysis of internal oxide particle formed at the alloy grain boundary (region 1 in Figure 6.2). The oxide particles consist mainly of Ti, Nb and O of $Ti_xNb_yO_z$ stoichiometry where $x > y$. The metal-oxide particle interface showed the presence of about 1 at. % of Si, 0.5 at. % of B and < 0.2 at. % of C. The presence of nonmetallic

alloy impurities such as B and C are clearly evident from the APT mass spectrum at mass-to-charge ratios 11 and 12 (main isotopes) respectively as shown in [Figure 6.3b](#).

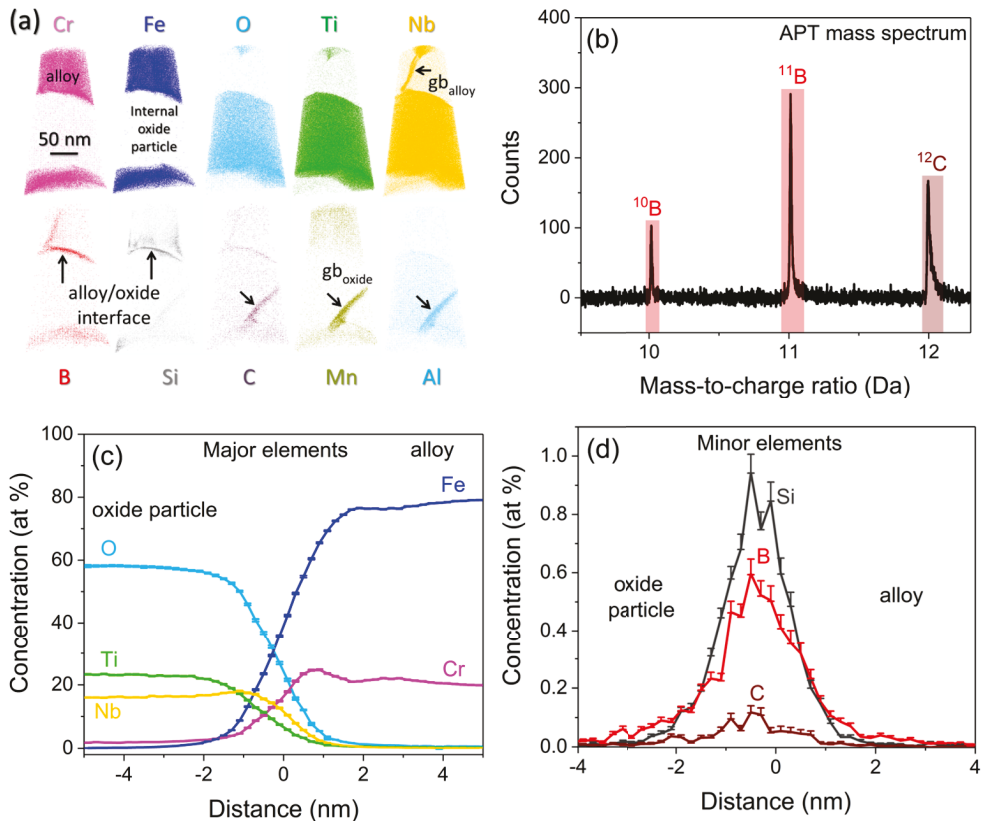


Figure 6.3: APT analysis of an inner Ti-rich oxide particle (Region 1 in [Figure 6.2b](#)) in Alloy-NT after isothermal oxidation at 800 °C in Ar–4% H_2 –4% H_2O for 72 hours. (a) Alloy/oxide particle interface with atom maps of major (Fe, Cr, Nb, Ti) and minor (Si, Mn, Al, B and C) alloying elements. (b) Mass spectrum showing the presence of impurities, such as B and C at the alloy/oxide particle interface. (c) Proximity histogram built across the alloy/oxide particle interface for major alloying elements and (d) for minor alloying elements.

The chemical segregation at grain boundaries in the alloy (in [Figure 6.4a](#)) as well as in the oxide particle ([Figure 6.4b](#)) were analyzed. The alloy GB enriched with Cr, Nb and Ti (in marginal amount) indicates the active diffusion of oxide forming elements through the alloy GB towards the oxide scale. Solubility of titanium in the alloy is slightly higher compared to Nb whereas the segregation of Nb at alloy GB is three times higher than Ti, indicating that Nb

diffusion is more intensive. This correlates with the formation of a continuous Nb-rich oxide layer rutile-type Nb(Ti, Cr)O₂ was observed just above the alloy (at chromia-alloy interface).

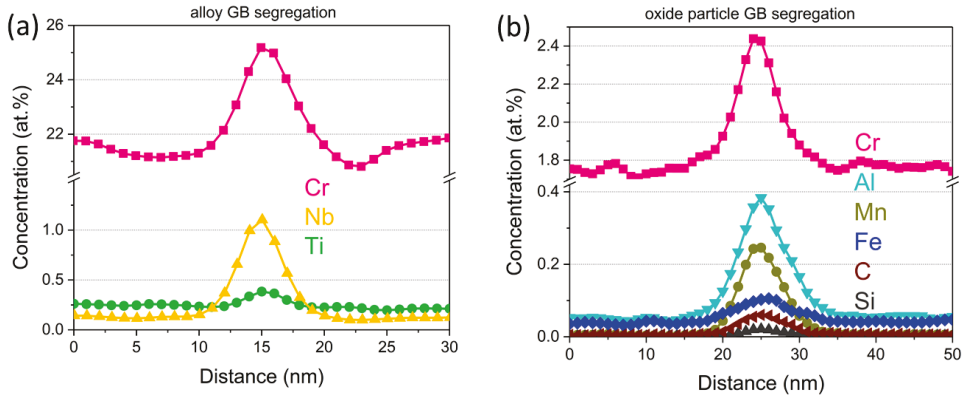


Figure 6.4: Concentration profiles from APT measurement for (a) alloy grain boundary and (b) oxide particle grain boundary.

The oxide particle containing GB appears to have a complex structure as it showed segregation of several minor alloying elements and impurities (Cr, Al, Mn, Fe, C and Si) [Figure 6.4b](#).

Surprisingly, C segregation appears both at the metal matrix–oxide particle interface and oxide particle GB. Quantitatively, the amount of C segregation at metal matrix–oxide particle interface ([Figure 6.3d](#)) and oxide particle GB ([Figure 6.4b](#)) is similar (both < 0.1 at. %).

In addition to internal oxide particles (Region 1 in [Figure 6.2b](#)), smaller oxide precipitates (Region 2 in [Figure 6.2b](#)) in the metal matrix were also characterized using APT (they were not identified by other methods on these materials due to their very small size). [Figure 6.5a](#) shows the atom maps containing internal oxide precipitates which are formed during high temperature oxidation in Ar – 4%H₂ – 4%H₂O at 800 °C for 72 hours of exposure. Two phases are observed in the presented dataset; i) internal oxide precipitates consisting mainly of O, Ti and Nb and ii) the metal matrix (Fe–Cr base alloy). The composition analyzed by building a proxigram (proximity histograms shown in [Figure 6.4b–c](#)) across the oxide precipitates–metal matrix interface, shows that their chemical composition is nearly identical to big internal oxide particles, Ti_xNb_yO_z (where $x > y$).

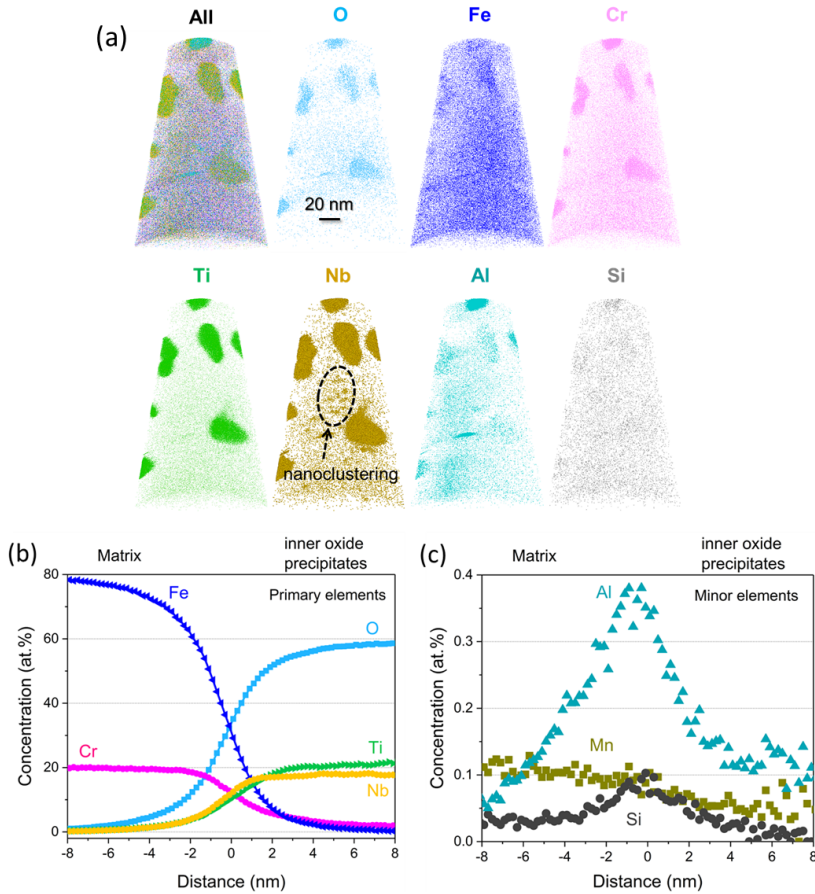


Figure 6.5: APT atom maps of subsurface layer containing small oxide precipitates (Region 2 in Figure 6.2b). Proxigram for the matrix and inner oxide precipitates interface for (a) primary elements and (b) minor elements.

Figure 6.5b shows a proximity histogram across the metal matrix–oxide particles interface for primary elements like Fe, Cr, O, Ti and Nb, whereas Figure 6.5c shows that for minor elements like Al, Mn and Si. The existence of these internal precipitates at the subsurface can efficiently strengthen the region by precipitation–strengthening mechanism (bigger and scattered oxide particles are not efficient for this).

Interestingly, in addition to these oxide precipitates, Nb–rich oxide clusters were observed in the matrix as shown in Figure 6.6. Unfortunately, it cannot be concluded whether these

nanoclusters really exist at high temperatures or they are formed during cooling the sample to room temperature.

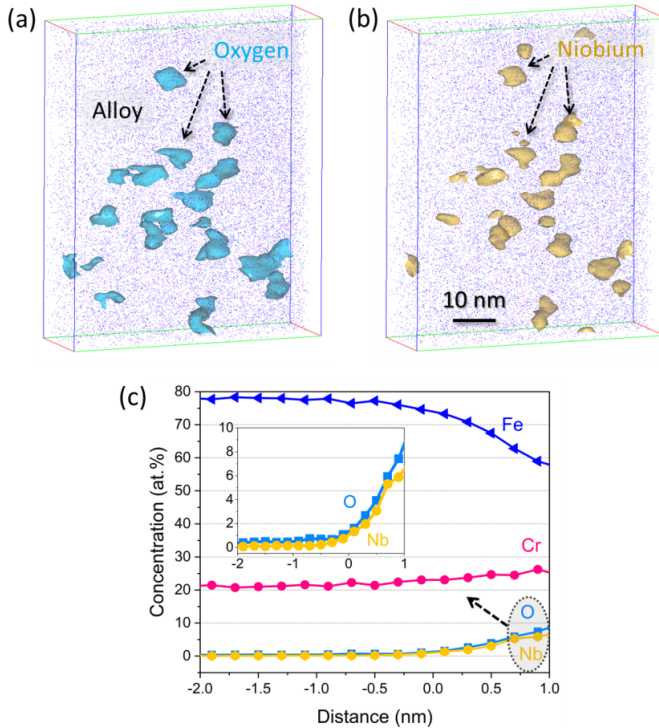


Figure 6.6: A small sub-volume of the Nb-rich nanoclusters as shown in Figure 6.5(a) and (b) Atom maps of oxygen and niobium respectively and (c) proximity histogram profiles for Fe, Cr, Nb and O. The inset figure highlights the Nb-rich oxide most likely of NbO₂ stoichiometry (as oxygen deficiency is an inherent artifact of APT).

6.4 Thermodynamic considerations

The precipitates in the internal oxidation zone mainly contain niobium and/or titanium oxide. While close to the metal-oxide interface the precipitates are rich in niobium, with increasing depth the titanium concentration increases until eventually the precipitates contain solely TiO₂. This depth dependence can qualitatively be explained by the relative differences in thermodynamic stability of the various oxides. Using the software package Thermocalc, in combination with the database TCFE8, the activities of Cr, Nb and Ti at 800 °C in the prevailing alloy are found to be 4.88×10^{-1} , 2.51×10^{-3} and 6.42×10^{-5} respectively. Using the

database FACT in FACTSAGE reveals that for these metal activities the dissociation pressures of chromium oxide, niobium oxide and titanium oxide are 8.2×10^{-28} , 5.5×10^{-27} and 4×10^{-35} bar respectively, suggesting that Ti can be oxidized at a depth where niobium oxide is no longer thermodynamically stable.

Titanium in the alloy is oxidized predominantly internally due to its low activity on the alloy surface in the experimental conditions and higher negative free energy than Cr_2O_3 or SiO_2 (ΔG_{TiO_2} ($-750.4 \text{ kJ mol}^{-1}$) $<$ ΔG_{SiO_2} ($-717.5 \text{ kJ mol}^{-1}$) $<$ $\Delta G_{\text{Cr}_2\text{O}_3}$ ($-568.3 \text{ kJ mol}^{-1}$)) [24].

6.5 Influence of gas composition

The extent of internal oxidation is less pronounced in Ar–20% O_2 than in Ar–4%H₂–4%H₂O (Figure 4.8). This could be explained by a mechanism proposed earlier [115] in similar gas compositions that the hydrogen taken up by the alloy during the exposure in low p_{O_2} gas modifies internal oxidation e.g. by affecting oxygen solubility and/or diffusivity or transport processes at interfaces between internal oxide and the alloy. An alternative explanation would relate to the growth rate of the external scale. If, at least during a certain time, the growth rate of the external scale formed in Ar–20% O_2 is slower than that in Ar–4%H₂–4%H₂O (Figure 5.1), subscale chromium depletion would be higher and thus the chromium interface concentration will be lower in the latter gas. Correspondingly, the oxygen activity at the metal–oxide interface will be lower in case of Ar–H₂–H₂O than in Ar– O_2 . This would qualitatively explain the observed differences in the extent of internal oxidation. However, further studies will be needed to determine if one of these mentioned mechanisms is responsible for the experimental findings.

6.6 Summary

Internal oxidation zones of one of the Crofer based steels (Alloy–NT) were successfully analyzed, and the results are summarized as follows:

1. Presence of Ti in all the studied alloys causes formation of TiO_2 –base particles in internal oxidation zone (IOZ).
2. Nb addition to Ti-containing steels results in its partial internal oxidation, as Nb and Ti together form $(\text{Nb}, \text{Ti})\text{O}_2$ type oxide particles of two size classes (big particles $>$ 100 nm

and small precipitates < 20 nm). These small oxide precipitates can provide additional subsurface strengthening for the base alloy.

3. Non-metallic alloy impurities such as boron and carbon preferentially segregate at alloy GBs and oxide particle GBs, respectively, in addition to their segregation at alloy-oxide particle interface.

7

Conclusion

A detailed investigation of the thermally grown oxide scales formed on four high-Cr ferritic steels, including commercial Crofer 22 H in three model atmospheres relevant to the SOCs operating conditions, namely high pO_2 (Ar–20% O_2) and low pO_2 (Ar–4%H₂–4%H₂O, Ar–1%CO–1%CO₂) atmospheres at 800 °C was performed. The microscopic regions responsible for the mass transport through the oxide scale (chromia and metal–oxide interface) were studied using atom probe tomography in conjunction with other methods. The relationships between the composition, microstructure and the oxidation behavior were established based on the determining role of GB in the oxidation processes. The main findings of the present investigation can be summarized as follows:

i) Gas composition

The total weight gain of the steel samples subjected to low pO_2 gases is significantly higher compared to high pO_2 gas, indicating lesser oxidation resistance. Oxidation rate in all the gas compositions obeys parabolic kinetics, i.e. mass transport through the oxide scale controls the oxidation process. Phase analysis reveals the duplex oxide structure consisting of outer spinel (MnCr₂O₄) and inner Cr₂O₃. The subsurface Cr₂O₃ layer, which acts as the main barrier disconnecting the metal from the atmosphere, shows fine, equiaxed grain structure in high pO_2 atmosphere. On the contrary, formation of coarse, elongated grains of porous chromia layer in low pO_2 atmospheres is evident. Additionally, a thin Nb(Cr, Ti)O₂ rich rutile-type layer forms at the metal–oxide interface in Nb-containing alloys. APT revealed segregation of Mn, Ti and Nb at chromia grain boundaries for all atmospheres in approximately similar amounts. Moreover, exposure in Ar–O₂ results in substantial accumulation of Mn and Fe impurities in chromia grain interiors, which was not observed in low pO_2 gases. Analysis of various factors, that are potentially responsible for the oxidation resistance in different gas compositions, revealed that the porosity difference in the chromia scale can be a decisive factor,

probably by providing rapid diffusion paths at the pore walls or directly through pores. Other factors such as bulk diffusion, grain boundary ionic conductivity or the GB network density cannot explain the observed difference in oxidation rates. The reason for different porosity in different gases cannot unfortunately be established with the characterization approaches used in the present work. It is important to note that the carbon from low pO_2 Ar–CO–CO₂ atmosphere does not enter the oxide scale and therefore carbon is not directly influencing the oxidation process.

ii) Alloy composition

The minor alloy constituents of all the investigated steels such as Mn, Ti and Nb actively segregate at chromia GBs during oxidation. In the alloy with low Si content (Alloy–NT), the Gibbsian interfacial excess G_i values indicate a monolayer or even higher GB coverage with Nb+Ti. Substitution of the host Cr³⁺ ions with aliovalent ions of higher-charged Nb⁴⁺/Nb⁵⁺ and Ti⁴⁺ ions (Wagner–Hauffe doping) can enhance cationic vacancies formation, resulting in accelerated outward diffusion of cations along GBs and eventually decreasing the oxidation resistance. However, the vacancy formation mechanism cannot solely explain the much stronger effect of Nb compared to that of Ti, suggesting possible modifications of GB structure in the presence of Nb which further changes the diffusion properties. The GB segregation of lower charged Mn²⁺ ions alleviates the negative effect of Nb⁴⁺/Nb⁵⁺ and Ti⁴⁺ ions. A relatively high Gibbs interfacial excess of Mn (G_{Mn}) in comparison to $G_{Nb} + G_{Ti}$ in Alloy–NTS (exhibiting slower oxidation) can suppress formation of cation vacancies and cause counter-formation of oxygen vacancies favoring inward diffusion of O²⁻ ions. This results in slow growth of the outermost spinel layer (thinner spinel) and nucleation of inner spinel grains in Alloy–NTS due to sluggish outward diffusion of Mn. Nb-containing alloys with marginal Si concentration (Alloy–NT and Alloy–N) exhibit an additional rutile-type oxide layer (Nb(Cr, Ti)O₂ and Nb(Cr)O₂) between chromia and metal matrix. This layer does not impede outward Mn diffusion (via GBs) and Cr (via GBs as well as lattice), which is essential to form the main chromia/spinel scales. Addition of Si to the alloy aids in Laves phase formation, which actively binds Nb and prevents it from entering oxide phase (both lattice and GBs), thus providing good oxidation resistance for Alloy–NTS. However, Si amounts of 0.4 at. % in the base Alloy–NTS leads to a net-like SiO₂ layer formation at the metal–oxide interface, which can become continuous at higher Si concentrations or during long term oxidation and therefore critical for the electrical properties of the interconnects. Lastly, La (reactive element) was not found either in the oxide scale or around the metal–oxide interface for all La-containing alloys (Alloy–NT and Alloy–N), ruling out the suggested direct mechanism for RE effect.

iii) Internal oxidation

Presence of Ti in all the studied alloys causes formation of TiO_2 -base particles in the internal oxidation zone (IOZ). Nb addition to the steels results in its partial internal oxidation, as Nb and Ti together form $(\text{Nb}, \text{Ti})\text{O}_2$ type oxide particles of two size classes (big particles > 100 nm and small precipitates < 20 nm). The oxide particles show $\text{Nb}_x\text{Ti}_y\text{O}_z$ stoichiometry, where $x > y$, at the vicinity of metal-oxide interface. The composition of the oxide particles gradually changes to $x < y$ with the depth and finally becomes TiO_2 . It was suggested that small oxide precipitates can substantially provide additional subsurface strengthening for the base alloy. Non-metallic alloy impurities such as boron and carbon preferentially segregate at alloy GBs and oxide particle GBs, respectively, in addition to their segregation at alloy-oxide particle interface.

7.1 Possible pathways for further steel development

Based on the results obtained and the understanding gained from this research work, strategies for further steel development are proposed.

1. Ti addition must be tolerated despite its direct influence on the oxidation due to its positive effect for subsurface alloy strengthening (in IOZ). However, adjustment of Ti amount might decrease its effect on oxidation without significantly modifying the IOZ, being thereby beneficial for high temperature oxidation resistance of these steels.
2. Nb is strongly deleterious for the oxidation resistance and should be, in principle, avoided (such as in the industrial Crofer 22 APU steel). However, an addition of controlled amount of Si together with Nb can result in their mutual binding in the strengthening Laves phase (positive effect) and concurrently eliminate their negative impact on the oxidation resistance.
3. La, one of the most expensive elements in the steel, does not show a direct influence on the oxidation (probably only binds other deleterious impurities such as sulfur), so it can be potentially replaced with a cheaper alternative for that purpose.

Bibliography

- [1] P. D. Lund et al. [Review of energy system flexibility measures to enable high levels of variable renewable electricity](#). In: *Renewable and Sustainable Energy Reviews* 45 (2015), 785–807.
- [2] A. Schavan. [Germany’s Energy Research Plan](#). In: *Science* 330.6002 (2010), 295–295.
- [3] A. Woyte, R. Belmans, and J. Nijs. [Fluctuations in instantaneous clearness index: Analysis and statistics](#). In: *Solar Energy* 81.2 (2007), 195–206.
- [4] P. Milan, M. Wächter, and J. Peinke. [Turbulent Character of Wind Energy](#). In: *Physical Review Letters* 110.13 (2013), 138701.
- [5] BMWi. [Innovations for the Energy Transition](#). In: *7th Energy Research Programme of the Federal Government* (2018).
- [6] S. C. Singhal and K. Kendall. [High Temperature and Solid Oxide Fuel Cells](#). Elsevier, 2003, 406.
- [7] K. Kendall and M. Kendall. [High-Temperature Solid Oxide Fuel Cells for the 21st Century](#). Elsevier, 2016.
- [8] V. Shemet et al. [Metallic Materials in Solid Oxide Fuel Cells](#). In: *Fuel Cell Technologies: State and Perspectives*. Vol. 7. 1. Berlin/Heidelberg: Springer-Verlag, 2006, 97–106.
- [9] R. Gorte and J. Vohs. [Nanostructured anodes for solid oxide fuel cells](#). In: *Current Opinion in Colloid & Interface Science* 14.4 (2009), 236–244.
- [10] W. Zhu and S. Deevi. [A review on the status of anode materials for solid oxide fuel cells](#). In: *Materials Science and Engineering: A* 362.1-2 (2003), 228–239.
- [11] N. H. Menzler et al. [Materials and manufacturing technologies for solid oxide fuel cells](#). In: *Journal of Materials Science* 45.12 (2010), 3109–3135.
- [12] N. Q. Minh. [Ceramic Fuel Cells](#). In: *Journal of the American Ceramic Society* 76.3 (1993), 563–588.
- [13] L. Antoni. [Materials for Solid Oxide Fuel Cells: the Challenge of their Stability](#). In: *Materials Science Forum* 461-464 (2004), 1073–1090.

-
- [14] S. C. Singhal. [Science and Technology of Solid-Oxide Fuel Cells](#). In: *MRS Bulletin* 25.03 (2000), 16–21.
- [15] L. Singheiser et al. [High Temperature Corrosion Issues for Metallic Materials in Solid Oxide Fuel Cells](#). In: *Shreir's Corrosion*. Elsevier, 2010, 482–517.
- [16] B. Kuhn et al. [Development of high chromium ferritic steels strengthened by inter-metallic phases](#). In: *Materials Science and Engineering A* 594 (2014), 372–380.
- [17] J. H. Froitzheim. “SOFC development of ferritic steels for SOFC interconnectors and interactions with Ni based anodes”. PhD thesis. RWTH Aachen University, 2008.
- [18] URL: https://www.vdm-metals.com/fileadmin/user_upload/Downloads/Data_Sheets/Data_Sheet_VDM_Crofer_22_H.pdf.
- [19] P. Huczowski. [Effect of geometry and composition of Cr steels on oxide scale properties relevant for interconnector applications in Solid Oxide Fuel Cells \(SOFCs\)](#). PhD Thesis, RWTH Aachen University, 2007, 159.
- [20] P. Kofstad. [High Temperature Corrosion](#). Elsevier, 1988.
- [21] N. Birks, G. H. Meier, and F. S. Pettit. [Introduction to the High-Temperature Oxidation of Metals](#). Cambridge: Cambridge University Press, 2006.
- [22] C. Wagner. [The theory of the warm-up process](#). In: *Zeitschrift für Physikalische Chemie* 21 (1933), 25–41.
- [23] C. Wagner. [Equations for transport in solid oxides and sulfides of transition metals](#). In: *Progress in Solid State Chemistry* 10 (1975), 3–16.
- [24] D. J. Young. [High Temperature Oxidation and Corrosion of Metals](#). Vol. 1. 2015, 576. arXiv: arXiv:1011.1669v3.
- [25] D. Naumenko, L. Singheiser, and W. Quadackers. “Oxidation Limited Life of FeCrAl Based Alloys During Thermal Cycling”. In: *EFC monograph number 27, Cyclic Oxidation of high Temperature Materials*, eds. M. Schütze, W.J. Quadackers, Institute of Materials. 1999, 288–306.
- [26] C. Gindorf, L. Singheiser, and K. Hilpert. [Chromium vaporisation from Fe, Cr base alloys used as interconnect in fuel cells](#). In: *Steel Research* 72.11-12 (2001), 528–533.
- [27] J. Froitzheim et al. [Development of high strength ferritic steel for interconnect application in SOFCs](#). In: *Journal of Power Sources* 178.1 (2008), 163–173.
- [28] B. Kuhn et al. [Effect of Laves phase strengthening on the mechanical properties of high Cr ferritic steels for solid oxide fuel cell interconnect application](#). In: *Materials Science and Engineering: A* 528.18 (2011), 5888–5899.
-

- [29] J. Quadakkers and L. Singheiser. [Practical Aspects of the Reactive Element Effect](#). In: *Materials Science Forum* 369-372 (2001), 77–92.
- [30] J. Froitzheim. [Ferritic steel interconnectors and their interactions with Ni base anodes in solid oxide fuel cells \(SOFC\)](#). 2008.
- [31] L. Niewolak et al. [Sigma-phase formation in high chromium ferritic steels at 650 °C](#). In: *Journal of Alloys and Compounds* 638 (2015), 405–418.
- [32] C. R. Helms and B. E. Deal, eds. [The Physics and Chemistry of SiO₂ and the Si–SiO₂ Interface](#). Boston, MA: Springer US, 1988.
- [33] J Piron-Abelian et al. “Long term oxidation behaviour and compatibility with contact materials of newly developed ferritic interconnector steel”. In: *European Solid Oxide Fuel Cell Forum*, 5. 2002, 248–256.
- [34] D. Naumenko, B. A. Pint, and W. J. Quadakkers. [Current Thoughts on Reactive Element Effects in Alumina-Forming Systems: In Memory of John Stringer](#). In: *Oxidation of Metals* 86.1-2 (2016), 1–43.
- [35] B. M. Ovsyannikov, V. N. Surovova, A. G. Ivanov, A. V. Salautin, and B. M. Ovsyannikov. In: 9 (1982), 35–37.
- [36] H. C. H. Carpenter. [The Influence of Phosphorus and Sulphur on the Mechanical Properties of Steel](#). In: *Nature* 98.2465 (1917), 410–411.
- [37] C. L. Briant. [The Effects of Sulfur and Phosphorus on the Intergranular Corrosion of 304 Stainless Steel](#). In: *CORROSION* 36.9 (1980), 497–509.
- [38] D. G. Lees. [On the reasons for the effects of dispersions of stable oxides and additions of reactive elements on the adhesion and growth-mechanisms of chromia and alumina scales-the sulfur effect](#). In: *Oxidation of Metals* 27.1-2 (1987), 75–81.
- [39] S. Chevalier et al. [Effects of chromia coatings on the high-temperature behavior of Fe₁₇Ti stainless steel in air. Effect of rare-earth-element oxides](#). In: *Oxidation of Metals* 47.1-2 (1997), 53–67.
- [40] S Chevalier et al. [The combined effect of refractory coatings containing reactive elements on high temperature oxidation behavior of chromia-forming alloys](#). In: *Corrosion Science* 45.8 (2003), 1661–1673.
- [41] S. Chevalier and J. Larpin. [Influence of reactive element oxide coatings on the high temperature cyclic oxidation of chromia-forming steels](#). In: *Materials Science and Engineering: A* 363.1-2 (2003), 116–125.

-
- [42] S. Chevalier et al. Influence of the mode of introduction of a reactive element on the high temperature oxidation behavior of an alumina-forming alloy. Part II: Cyclic oxidation tests. In: *Materials and Corrosion* 55.8 (2004), 610–616.
- [43] T. Richardson. *Shreir's Corrosion*. Elsevier Science, 2009, 4000.
- [44] H. Beske et al. SIMS investigations on the growth mechanisms of protective chromia and alumina surface scales. In: *Mikrochimica Acta* 101.1-6 (1990), 109–119.
- [45] P. Papaicovou et al. The effect of CeO₂ coatings on the oxidation behaviour of Fe – 20 Cr alloys in O₂ at 1173 K. In: *Corrosion Science* 30.4-5 (1990), 451–460.
- [46] R. J. Hussey and M. J. Graham. The influence of reactive-element coatings on the high-temperature oxidation of pure-Cr and high-Cr-content alloys. In: *Oxidation of Metals* 45.3-4 (1996), 349–374.
- [47] J. Klöwer and J.-G. Li. Effects of yttrium on the oxidation behaviour of Iron-Chromium-Aluminium Alloys. In: *Materials and Corrosion/Werkstoffe und Korrosion* 47.10 (1996), 545–551.
- [48] J. Klöwer. Factors affecting the oxidation behaviour of thin Fe-Cr-Al foils. Part II: The effect of alloying elements: Overdoping. In: *Materials and Corrosion* 51.5 (2000), 373–385.
- [49] B. A. Pint. Experimental observations in support of the dynamic-segregation theory to explain the reactive-element effect. In: *Oxidation of Metals* 45.1-2 (1996), 1–37.
- [50] G. J. Yurek. Segregation of Y to Grain Boundaries in Cr₂O₃ and NiO Scales Formed on an ODS Alloy. In: *Journal of The Electrochemical Society* 134.10 (1987), 2643.
- [51] K. Przybylski. The influence of implanted yttrium on the oxidation properties of a Co-25Cr-1Al alloy. In: *Materials Science and Engineering: A* 120-121 (1989), 509–517.
- [52] B. A. Pint. Grain Boundary Segregation of Cation Dopants in α -Al₂O₃ Scales. In: *Journal of The Electrochemical Society* 145.6 (1998), 1819.
- [53] T. Horita et al. Evaluation of Laves-phase forming Fe–Cr alloy for SOFC interconnects in reducing atmosphere. In: *Journal of Power Sources* 176.1 (2008), 54–61.
- [54] W. Quadackers and J. Žurek. Oxidation in Steam and Steam/Hydrogen Environments. In: *Shreir's Corrosion*. Elsevier, 2010, 407–456.
- [55] M Michalik et al. “Effect of water vapour on growth and adherence of chromia scales formed on Cr in high and low”. PhD thesis. Forschungszentrum Jülich GmbH, 1913, 213–221.
-

- [56] W Quadakkers et al. Compatibility of perovskite contact layers between cathode and metallic interconnector plates of SOFCs. In: *Solid State Ionics* 91.1-2 (1996), 55–67.
- [57] S. Linderoth et al. Investigations of metallic alloys for use as interconnects in solid oxide fuel cell stacks. In: *Journal of Materials Science* 31.19 (1996), 5077–5082.
- [58] M. Ueda and H. Taimatsu. Thermal Expansivity and High-Temperature Oxidation Resistance of Fe–Cr–W. In: *Materials Transactions, JIM* 40.12 (1999), 1390–1395.
- [59] M. Ueda, M. Kadowaki, and H. Taimatsu. Effect of La and Ce on the Reactivity of Fe – 18 mass%Cr – 7 mass%W Alloy with $\text{La}_{0.85}\text{Sr}_{0.15}\text{MnO}_3$. In: *Materials Transactions, JIM* 41.2 (2000), 317–322.
- [60] K Huang. Characterization of iron-based alloy interconnects for reduced temperature solid oxide fuel cells. In: *Solid State Ionics* 129.1-4 (2000), 237–250.
- [61] T. Brylewski. Application of Fe–16Cr ferritic alloy to interconnector for a solid oxide fuel cell. In: *Solid State Ionics* 143.2 (2001), 131–150.
- [62] T. Horita et al. Evaluation of Fe–Cr Alloys as Interconnects for Reduced Operation Temperature SOFCs. In: *Journal of The Electrochemical Society* 150.3 (2003), A243.
- [63] T. Horita et al. Stability of Fe–Cr alloy interconnects under $\text{CH}_4\text{–H}_2\text{O}$ atmosphere for SOFCs. In: *Journal of Power Sources* 118.1-2 (2003), 35–43.
- [64] C. Asensio-Jimenez. Effect of Composition, Microstructure and Component Thickness on the Oxidation Behaviour of Laves Phase Strengthened Interconnect Steel for Solid Oxide Fuel Cells (SOFC). In: *RWTH Aachen, PhD Thesis* (2014).
- [65] C. Wagner. Theoretical Analysis of the Diffusion Processes Determining the Oxidation Rate of Alloys. In: *Journal of The Electrochemical Society* 99.10 (1952), 369.
- [66] S. Guruswamy et al. Internal oxidation of Ag-In alloys: Stress relief and the influence of imposed strain. In: *Oxidation of Metals* 26.1-2 (1986), 77–100.
- [67] C. Wagner. Reaktionstypen bei der Oxydation von Legierungen. In: *Zeitschrift fuer Elektrochemie* 63.7 (1959), 772–782.
- [68] D. L. Douglass. A critique of internal oxidation in alloys during the post-wagner era. In: *Oxidation of Metals* 44.1-2 (1995), 81–111.
- [69] G Böhm and M Kahlweit. Über die innere Oxydation von Metallegierungen. In: *Acta Metallurgica* 12.5 (1964), 641–648.
- [70] J. Groza. Heat-resistant dispersion-strengthened copper alloys. In: *Journal of Materials Engineering and Performance* 1.1 (1992), 113–121.

-
- [71] D. G. R. William D. Callister Jr. *Callister's Materials Science and Engineering, 10th Edition, Global Edition*. 2019, 944.
- [72] Y. Mishin et al. *Grain boundary diffusion: fundamentals to recent developments*. In: *International Materials Reviews* 42.4 (1997), 155–178.
- [73] V. I. Dybkov. *Reaction diffusion and solid state chemical kinetics : Handbook*. Zurich : Trans Tech Publ., 2010. - 330 p., 2010.
- [74] J. Ayache et al. *Sample Preparation Handbook for Transmission Electron Microscopy*. New York: Springer New York, 2010.
- [75] J. Yang et al. *Electron microscopy studies of NiAl/ γ -Al₂O₃ interfaces*. In: *Scripta Metallurgica et Materialia* 33.7 (1995), 1043–1048.
- [76] K. Unocic et al. *Effect of environment on the scale formed on oxide dispersion strengthened FeCrAl at 1050 °C and 1100 °C*. In: *Materials at High Temperatures* 29.3 (2012), 171–180.
- [77] P. Schlossmacher et al. *Nanoscale Chemical Compositional Analysis with an Innovative S/TEM-EDX System*. In: *Microscopy and Analysis Nanotechnology Supplement 24* (2010), S5–S8.
- [78] Muller, E. W., *Zhurnal Tekhnicheskoi Fiziki* 1936, 17, 412. In: ().
- [79] A. Cerezo, T. J. Godfrey, and G. D. W. Smith. *Application of a position-sensitive detector to atom probe microanalysis*. In: *Review of Scientific Instruments* 59.6 (1988), 862–866.
- [80] T. F. Kelly et al. *On the many advantages of local-electrode atom probes*. In: *Ultramicroscopy* 62.1-2 (1996), 29–42.
- [81] B. Gault et al. *Atom Probe Microscopy*. Vol. 160. Springer Series in Materials Science. New York, NY: Springer New York, 2012.
- [82] D. J. Larson et al. *Local Electrode Atom Probe Tomography*. New York, NY: Springer New York, 2013.
- [83] M. K. Miller. *Atom Probe Tomography*. Boston, MA: Springer US, 2000.
- [84] K. Thompson et al. *In situ site-specific specimen preparation for atom probe tomography*. In: *Ultramicroscopy* 107.2-3 (2007), 131–139.
- [85] T. Kelly et al. *Local Electrode Atom Probe Tomography - A User's Guide*. February. 2006.
- [86] T. F. Kelly and D. J. Larson. *Local Electrode Atom Probes*. In: *Materials Characterization* 44.1-2 (2000), 59–85.

- [87] D. Larson et al. [Field-ion specimen preparation using focused ion-beam milling](#). In: *Ultramicroscopy* 79.1-4 (1999), 287–293.
- [88] M. K. Miller and R. G. Forbes. [Atom-Probe Tomography](#). Boston: Springer US, 2014.
- [89] A. Devaraj et al. [Three-dimensional nanoscale characterisation of materials by atom probe tomography](#). In: *International Materials Reviews* 63.2 (2018), 68–101.
- [90] D. R. Diercks et al. [Three-dimensional quantification of composition and electrostatic potential at individual grain boundaries in doped ceria](#). In: *Journal of Materials Chemistry A* 4.14 (2016), 5167–5175.
- [91] Y. M. Chen et al. [Laser-assisted atom probe analysis of zirconia/spinel nanocomposite ceramics](#). In: *Scripta Materialia* 61.7 (2009), 693–696.
- [92] E. A. Marquis et al. [Probing the improbable: Imaging C atoms in alumina](#). In: *Materials Today* 13.10 (2010), 34–36.
- [93] J.-H. Kim et al. [The role of grain boundaries in the initial oxidation behavior of austenitic stainless steel containing alloyed Cu at 700 °C for advanced thermal power plant applications](#). In: *Corrosion Science* 96 (2015), 52–66.
- [94] I. Povstugar et al. [Correlative Atom Probe Tomography and Transmission Electron Microscopy Analysis of Grain Boundaries in Thermally Grown Alumina Scale](#). In: *Microscopy and Microanalysis* 25.1 (2019), 11–20.
- [95] P. Kontis et al. [The effect of boron on oxide scale formation in a new polycrystalline superalloy](#). In: *Scripta Materialia* 127 (2017), 156–159.
- [96] K. Stiller et al. [Atom probe tomography of interfaces in ceramic films and oxide scales](#). In: *MRS Bulletin* 41.1 (2016), 35–39.
- [97] J. P. Pfeifer et al. [Quantitative analysis of oxide films on ODS-alloys using MCs⁺-SIMS and e-beam SNMS](#). In: *Fresenius' Journal of Analytical Chemistry* 346.1-3 (1993), 186–191.
- [98] [Chapter 9 AB2X4 structure](#). In: *Developments in Geochemistry*. Ed. by S. Mitra. Vol. 9. C. 2004, 673–709.
- [99] A. Naoumidis et al. [Phase studies in the chromium-manganese-titanium oxide system at different oxygen partial pressures](#). In: *Journal of the European Ceramic Society* 7.1 (1991), 55–63.
- [100] P. Huczowski et al. “Growth rates and electrical conductivity of oxide scales on ferritic steels proposed as interconnect materials for SOFCs”. In: *6th European Solid Oxide Fuel Cell Forum, Proceedings, Vol. 3, Jun 28-Jul 2, 2004*, 1594–1601.

-
- [101] H. Nabelek et al. Reducing Degradation Effects in SOFC Stacks Manufactured at Forschungszentrum Julich - Approaches and Results. In: *Advances in Solid Oxide Fuel Cells III*. Hoboken, NJ, USA: John Wiley & Sons, Inc., 2009, 65–77.
- [102] A. Devaraj et al. Role of Photoexcitation and Field Ionization in the Measurement of Accurate Oxide Stoichiometry by Laser-Assisted Atom Probe Tomography. In: *The Journal of Physical Chemistry Letters* 4.6 (2013), 993–998.
- [103] M. Karahka, Y. Xia, and H. J. Kreuzer. The mystery of missing species in atom probe tomography of composite materials. In: *Applied Physics Letters* 107.6 (2015), 062105.
- [104] D. Zanuttini et al. Simulation of field-induced molecular dissociation in atom-probe tomography: Identification of a neutral emission channel. In: *Physical Review A* 95.6 (2017), 061401.
- [105] D. J. Young. *High Temperature Oxidation and Corrosion of Metals*. Elsevier, 2016, 758.
- [106] M. Michalik et al. Effect of water vapour on growth and adherence of chromia scales formed on Cr in high and low p_{O_2} -environments at 1000 and 1050°C. In: *Materials at High Temperatures* 22.3-4 (2005), 213–221.
- [107] T. D. Nguyen, J. Zhang, and D. J. Young. Growth of Cr_2O_3 blades during alloy scaling in wet CO_2 gas. In: *Corrosion Science* 133 (2018), 432–442.
- [108] W. Quadackers et al. Metallic interconnectors for solid oxide fuel cells – a review. In: *Materials at High Temperatures* 20.2 (2003), 115–127.
- [109] X. Guo and Y. Ding. Grain Boundary Space Charge Effect in Zirconia. In: *Journal of The Electrochemical Society* 151.1 (2004), J1.
- [110] K. L. Kliewer and J. S. Koehler. Space Charge in Ionic Crystals. I. General Approach with Application to NaCl. In: *Physical Review* 140.4A (1965), A1226–A1240.
- [111] B. W. Krakauer and D. N. Seidman. Absolute atomic-scale measurements of the Gibbsian interfacial excess of solute at internal interfaces. In: *Physical Review B* 48.9 (1993), 6724–6727.
- [112] P. Maugis and K. Hoummada. A methodology for the measurement of the interfacial excess of solute at a grain boundary. In: *Scripta Materialia* 120 (2016), 90–93.
- [113] O. C. Hellman and D. N. Seidman. Measurement of the Gibbsian interfacial excess of solute at an interface of arbitrary geometry using three-dimensional atom probe microscopy. In: *Materials Science and Engineering: A* 327.1 (2002), 24–28.
- [114] C. Chen et al. Rutile phases in the $CrNbO_4VO_2MoO_2$ system: Preparation and properties. In: *Journal of Solid State Chemistry* 64.1 (1986), 81–89.
-

- [115] E. Essuman et al. Enhanced internal oxidation as trigger for breakaway oxidation of Fe–Cr alloys in gases containing water vapor. In: *Scripta Materialia* 57.9 (2007), 845–848.

Acknowledgements

This dissertation would not have been conceivable without the support and encouragement of a large number of people. I would like to take this opportunity to express my deep gratitude. I am grateful to Prof. Joachim Mayer as my thesis supervisor, for sharing his knowledge and my biggest thanks to Prof. Lorenz Singheiser, who kindly agreed to review my thesis.

I would like to express my sincere acknowledgment to Dr. Ivan Povstugar, my scientific advisor, who from his broad knowledge and experience on APT, has always provided valuable inputs by constructively questioning every result and offering plenty of time for discussions. I am very thankful for his enthusiastic supervision and guidance throughout my PhD and for teaching me APT very patiently.

I would like to thank my collaborators Prof. Willem J. Quadackers and Dr. Dmitry Naumenko from Microstructure and Properties of Materials (IEK-2), Forschungszentrum Jülich GmbH for their enthusiastic co-supervision and fruitful guidance throughout my PhD on high temperature oxidation. Other colleagues from this institute are also sincerely acknowledged; Mr. Timur Galiullin (PhD student) for GD-OES, Dr. Egbert Wessel for TEM, Dr. Daniel Grüner for SEM, Mr. Mirko Ziegner for XRD, Mr. Volker Gutzeit for metallography and Heiko Cosler for TG measurements.

I would also like to thank Dr. Elmar Neumann of HNF who was quite helpful in allowing me to use FIB till late evenings as well as on weekends.

Prof. Dr. Stephan Küppers of Central Institute for Engineering, Electronics and Analytics (ZEA-3) and HiTEC Graduate School of Forschungszentrum Jülich are acknowledged for providing me with the opportunity to carry out my doctoral research at ZEA-3 in Forschungszentrum Jülich.

I thank all my colleagues at the Forschungszentrum Jülich for all the stimulating discussions and the precious moments we shared during and outside of work. Thanks to my friends here in Jülich, with whom I have spent the memorable three years of my life. I deeply acknowledge my office mates Akbar, Liming, Younas, Serkan for the discussions related to or unrelated to work and for keeping me motivated.

Lastly, I would like to thank my parents and my brother for their support and encouragement.

Curriculum Vitae

Sep 2016 – Mar 2020	Joint PhD at RWTH Aachen University (FB-5) and Forschungszentrum Juelich (ZEA-3), Germany Nanoscale investigation of high temperature oxidation mechanisms of high-Cr ferritic steels
Aug 2013 – Jul 2016	Master of Science in the Department of Metallurgical and Materials Engineering, Indian Institute of Technology Madras (IIT-M), India. High temperature oxidation and hot corrosion behaviour of directionally solidified Ni-base superalloys
Aug 2012 – May 2013	Graduate Trainee at International Advanced Research Center for Powder Metallurgy and New Materials (ARCI), Hyderabad, India. Detonation spray gun (D-Gun) coatings to improve the corrosion and wear resistance of engineering components
Sep 2008 – May 2012	Bachelor of Technology at Jawaharlal Nehru Technological University (JNTU), Hyderabad, India. High temperature corrosion of Ti-base alloys for gas turbine applications

PUBLICATIONS

1. A. Vayyala, I. Povstugar, T. Galiullin, D. Naumenko, W. J. Quadackers, H. Hattendorf, and J. Mayer. Effect of Nb addition on oxidation mechanisms of high-Cr ferritic steel in Ar-H₂-H₂O. *Oxidation of Metals*, 92(5):471–491, 2019. <https://doi.org/10.1007/s11085-019-09933-x>
2. A. Vayyala, I. Povstugar, D. Naumenko, W. J. Quadackers, H. Hattendorf and J. Mayer. A Nanoscale Study of Thermally Grown Chromia on High-Cr Ferritic Steels and Associated Oxidation Mechanisms. *Journal of Electrochemical Society*, 167(6), 2020.

CONFERENCES

2019	<u>Ashok Vayyala</u> , Ivan Povstugar, Dmitry Naumenko, Willem J. Quadackers and Joachim Mayer; Effect of nanoscale chemistry on oxidation behaviour of thermally grown Cr ₂ O ₃ former ferritic steels, <i>CORCON (Corrosion Conference)</i> , Chennai, India. (talk)
2018	<u>Ashok Vayyala</u> , Ivan Povstugar, Dmitry Naumenko, Willem J. Quadackers and Joachim Mayer; Insights into the chemistry of high temperature oxide scales, grain boundaries and interfaces, <i>CORSYM (Corrosion Symposium)</i> , Chennai, India. (award for best presentation)
2018	Ivan Povstugar, <u>Ashok Vayyala</u> ; Quantitative analysis of grain boundary segregation in oxides: the influence of APT reconstruction accuracy, <i>10th European Atom Probe Workshop</i> , 7-9 th November 2018, Düsseldorf, Germany.
2017	<u>Ashok Vayyala</u> , Ivan Povstugar, Dmitry Naumenko, Willem J. Quadackers and Joachim Mayer; Effect of gas composition on high temperature oxidation of ferritic steel in SOEC relevant environments, <i>Gordon Research Conference (GRC) on High Temperature Corrosion</i> , NH, USA. (award for best poster)
2017	Ivan Povstugar, Juliane Weber, Egbert Wessel, <u>Ashok Vayyala</u> , Dmitry Naumenko, Willem J. Quadackers; Correlative TEM and APT analysis of high-temperature oxidation behavior of high-Cr ferritic steels, <i>7th European Atom Probe Workshop</i> , 2-5 th October 2017, Gullmarsstrand, Sweden.

SUMMER SCHOOL

2016 1st Summer school on Atom Probe Tomography, Friedrich-Alexander-Universität (FAU) Erlangen-Nürnberg, Germany

INVITED TALKS

2020 *Nanoscale investigation of thermally grown oxides*, Institute of Nanotechnology, Karlsruhe Institute of Technology, Germany.

2019 *Nanoscale characterization of thermally grown oxides on high temperature materials*, Department of Metallurgical Engineering and Materials Science, Indian Institute of Technology Bombay (IIT-B), India.

Band / Volume 477

Massentransportphänomene in Schichtsystemen eines Elektrolyseurs

U. Panchenko (2019), 107 pp

ISBN: 978-3-95806-433-1

Band / Volume 478

Mechanische Eigenschaften von Polymer-Elektrolyt-Membran-Brennstoffzellen

P. Imscher (2019), vii, 177 pp

ISBN: 978-3-95806-435-5

Band / Volume 479

Morphology and Degradation of High Temperature Polymer Electrolyte Fuel Cell Electrodes

S. Liu (2019), III, 162 pp

ISBN: 978-3-95806-436-2

Band / Volume 480

Structural uptake and retention of safety relevant radionuclides by cementitious materials

S. Lange (2019), 133 pp

ISBN: 978-3-95806-437-9

Band / Volume 481

Quantifying the Impact of Inhomogeneity, Transport and Recombination in Emerging Thin-Film Solar Cells

P. Kaienburg (2019), vii, 258 pp

ISBN: 978-3-95806-440-9

Band / Volume 482

Studies of oxidation resistant tungsten alloys at temperatures of 1100K to 1475K

F. Klein (2019), 158 pp

ISBN: 978-3-95806-444-7

Band / Volume 483

Impact Assessment of Land-Use Change and Agricultural Treatments on Greenhouse Gas Emissions from Wetlands of Uganda and Tanzania

K. X. X. Wagner (2019), 144 pp

ISBN: 978-3-95806-447-8

Band / Volume 484

IEK-3 Report 2019

Tailor-Made Energy Conversion for Sustainable Fuels

D. Stolten, B. Emonts (Eds.) (2020), 162 pp

ISBN: 978-3-95806-451-5

Band / Volume 485

Multiskalare Modellierung integrierter Energie- und Elektrizitätssysteme

T. C. Pesch (2019), XXV, 384 pp

ISBN: 978-3-95806-452-2

Band / Volume 486

**Quantitative Untersuchung des Laserablationsprozesses mittels
Kombination von optischer Spektroskopie und Massenspektrometrie**

J. Oelmann (2020), vii, 141 pp

ISBN: 978-3-95806-453-9

Band / Volume 487

**Leistungssteigerung metallgestützter Festelektrolyt-Brennstoffzellen
(MSCs) durch gezielte Optimierungen des Anoden/Elektrolytverbunds**

C. Bischof (2020), X, 176 pp

ISBN: 978-3-95806-455-3

Band / Volume 488

**Aluminiumoxiddispersionsverstärkte Haftvermittlermaterialien in
Wärmedämmschichtsystemen**

C. Vorkötter (2020), VIII, 99, XXXIII pp

ISBN: 978-3-95806-457-7

Band / Volume 489

**The Balmer lines emission of fast hydrogen atoms at the plasma-solid
interface in a low density plasma: challenges and applications**

S. O. Dickheuer (2020), 117 pp

ISBN: 978-3-95806-458-4

Band / Volume 490

**Micromechanical Characterization of Ceramic Solid
Electrolytes for Electrochemical Storage Devices**

J. F. Nonemacher (2020), xv, 131 pp

ISBN: 978-3-95806-461-4

Band / Volume 491

**Nanoscale investigation of high temperature oxidation mechanisms
of high-Cr ferritic steels**

A. Vayyala (2020), xix, 105 pp

ISBN: 978-3-95806-467-6

Energie & Umwelt / Energy & Environment
Band / Volume 491
ISBN 978-3-95806-467-6

Mitglied der Helmholtz-Gemeinschaft

